Development of High Performance Organic-Inorganic Halide Perovskite Optoelectronic Devices via Morphological and Interfacial Manipulation

Ting Zhao

A dissertation

submitted in partial fulfillment of the

requirements for the degree of

Doctor of Philosophy

University of Washington

2019

Reading Committee:

Alex K.-Y. Jen, Chair

Xiaodong Xu

Lucien N. Brush

Program Authorized to Offer Degree:

Materials Science and Engineering

University of Washington

Abstract

Development of High Performance Organic-Inorganic Halide Perovskite Optoelectronic Devices via Morphological and Interfacial Manipulation

Ting Zhao

Chair of the Supervisory Committee:
Professor Alex K.-Y. Jen
Materials Science and Engineering

Organic-inorganic halide perovskites (OIHPs) have emerged as excellent solution processable semiconductors for a new generation of potentially printable and efficient optoelectronic devices in recent years, including photodetection, energy harvesting, and light-emitting devices. The rise to prominence for this class of materials is fueled by their superior properties, such as tunable bandgap, high carrier mobility, outstanding optoelectronic merits, and low-cost solution processability. Given all exciting properties, solution-processed perovskite thin film also shows very challenging characteristics including difficult morphology control and substantial defects at film surface and grain boundaries (GBs). In this dissertation, integrated morphological and interfacial approaches have been utilized to overcome the above-mentioned challenges and further enhance performance of OIHP optoelectronic devices. Chapter 1 briefly overviews basics of perovskite material, current status of various perovskite optoelectronic devices, and remaining challenges for obtaining high quality solution processed perovskite thin film. Chapter 2 introduces common experimental details involved in this work including material preparation, material property characterization, device fabrication and performance test. Chapter 3 demonstrates a fast (<1s) and simple post deposition chemical treatment during which crystal reconstruction induced by a methylamine (MA^0) vapor greatly improves perovskite film coverage, crystallinity, and perovskite solar cell (PSC) performance. In Chapter 4, another method to improve perovskite film morphology is proposed. An ion exchange method for conversion from two-dimensional (2D) to three-dimensional (3D) perovskite is developed to grow highly oriented methylammonium lead bromide ($MAPbBr_3$) thin films with much-improved substrate coverage. The enhanced film quality leads to ultra-narrow electroluminescence spectra (15.3 nm full width half maximum (FWHM) and 98.10% color purity) and demonstrates immense potential of the ion exchange method for achieving ultrahigh resolution displays. Chapter 5 presents a simple defect passivation method by post-treating $CH_3NH_3PbI_3$ ($MAPbI_3$) film with diammonium iodide $NH_3I(CH_2)_8NH_3I$ (C8). Bilateral ammonium iodide end of C8 can simultaneously passivate perovskite layer and dope adjacent electron-transporting layer in derived PSCs. Consequently, the thin-film PSC passivated by C8 show reduced recombination loss and a much-improved power conversion efficiency (PCE) of 17.2% compared to 14.7% of the control device.

TABLE OF CONTENTS

LIST OF FIGURES

LIST OF TABLES

ACKNOWLEDGEMENTS

I would like to gratefully acknowledge my Ph.D. advisor Dr. Alex K.-Y. Jen for his continuous support of my Ph.D. study. His passion and dedication for research sets a great example for me. His patient guidance and encouragement in the past five years help me go through many obstacles and become a better person. I would also like to express my gratitude to my undergrad research advisor Dr. Shouke Yan who fueled my passion for abroad study. Without him I won't be able to chase my dreams here. Along with my advisors, I deeply thank Dr. Chu-Chen Chueh who provided me tremendous guidance and support as my mentor. The brainstorming and discussions we had laid a solid foundation for this work. I want to thank my colleagues Dr. Spencer T. Williams and Adharsh Rajagopal for their sincere support. Through them I learned how to be both creative and pragmatic, and always be open-minded. I would also like to thank my committee members and graduate school representative, Dr. Xiaodong Xu, Dr. Lucien N. Brush and Dr. Lih Y. Lin for their effort and advices for my thesis.

During my graduate studies, I have had the opportunity to work with and learn from people with different expertise. I sincerely thank many of the Jen group members: Dr. Sei-Hum Jang, Francis (Ray) Lin, Dr. Po-wei Liang, Dr. Chang-Zhi Li, Dr. Lijian Zuo, Dr. Weifei Fu, Dr. Sae Byeol Jo, Dr. Qi Chen, Dr. Xiaobao Xu, Dr. Hongliang Zhong, Dr. Jeremy Intemann, Dr. Yunxiang Xu, Dr. Zhong'an Li, Dr. Fan Zuo, Dr. Zhibin Yang, Dr. Xueliang Shi, Dr. Kai-Wei Cai, Dr. Chen-Hao Wu, Dr. Jieyun Wu, Dr. Nathan Cernetic, Dr. Kung-Shih Chen, Dr. Jiangsheng Yu, Dr. Weihua Tang, and Dr. Shengqiang Liu. Collaborators and technical staff at the University of Washington including Dr. Dane W. De Quilettes, Dr. Mark E. Ziffer, Hongbin Liu, Dr. David S. Ginger, Dr. Werner Kaminsky, and Dr. Liam Bradshaw have profoundly improved the quality of this work.

I would like to thank all my friends who shared happiness and sorrow together with me through my study. There have been lots of excitements and gain in my entire graduate experience, but most of them were obtained through learning from mistakes and being persistent which is not an easy process. I owe sincere thankfulness to below individuals who comforted me through difficult times and taught me never to give up: Dian Yuan, Weiwei Xu, Wentao Lu, Yun Li, Xiao Yang, Dr. Chu Han, Junyi Sun, Zhiyuan Deng, Yunshan Fan and Ye Zhang.

More than everything, I would like to thank my beloved parents for all their love and support. As the first member in my immediate and extended family to earn a doctoral degree and pursue my dream outside China, my father Junmin Zhao and my mother Jinfeng Zhang always provide me unconditional love and encourage me to be courageous. Thank you for everything you have done for me.

Chapter 1. INTRODUCTION

1.1 INTRODUCTION TO HYBRID PEROVSKITE MATERIALS

1.1.1 *Crystal Structure*

Perovskite refers to a crystallographic family with general ABX_3 3D structural framework. (**Figure 1.1a**) Monovalent cation A is either inorganic (Cs^+) or organic ($CH_3NH_3^+$ (MA^+) or $HC(NH_2)_2^+$ (FA^+)), and the relative sizes of B and X, where B is a divalent metal cation (Pb^{2+} or Sn^{2+}) and X is a halogen anion (Cl^-, Br^-, or I^-).[1]

Space filling ionic size constraints dictate whether a certain set of "A", "B", or "X" ions may adopt the perovskite framework, which involves a corner-sharing network of BX_6 octahedra, with the "A" cations occupying 12-fold coordinated holes within the structure and counterbalancing the charge of the BX_3 extended anion.[2] Therefore, the A cation is limited by the space of the hole and a too large A cation cannot be accommodated into it. To predict the perovskite formability, tolerance factor t and octahedral factor μ were introduced.[3] (**Equation 1.1**), where R_A, R_B, and R_X are the ionic radii for the corresponding ions and the tolerance factor must satisfy $t \approx 1$, empirically it is found that $0.8 \leq t \leq 1.0$ for most 3D perovskites. If t locates in the range 0.89-1.0, a more symmetric cubic structure would be formed. Tetragonal or orthorhombic structures are preferred if a lower t value derived. Calculated and estimated t and μ factors for a range of perovskites are shown in **Figure 1.1b**.

$$t = \frac{R_A + R_X}{\sqrt{2}(R_B + R_X)} \tag{1.1}$$

$$\mu = \frac{R_B}{R_X} \tag{1.2}$$

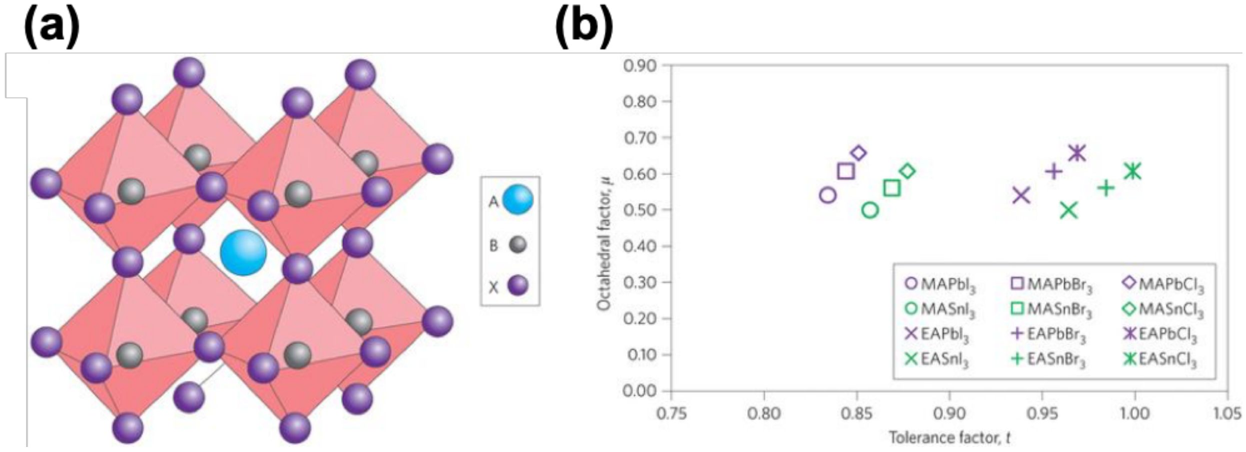

Figure 1.1. (a) Crystal structure of metal halide perovskite with a chemical formula of ABX_3. **(b)** Calculated tolerance factor t and octahedral factor μ for 12 halide perovskites. [1]

When ionic size of cation A is too large to fit into the hole, low-dimensional (LD) perovskites (2D, 1D, 0D) can potentially form; structure shown in **Figure 1.2**. Most common large organic cation A is aliphatic or aromatic ammonium salt. It can be monoammonium $R\text{-}NH_3^+$ or diammonium (NH_3^+- $R\text{-}NH_3^+$) cations that either one or both ends of the organic molecules is ammonium group.[4] For 2D perovskites, each $[PbI_6]^{4-}$ octahedron is connected with four halides forming a 2D network layer that is sandwiched between two organic layers. For the 1D case, each octahedron is connected at two opposite corners with its neighbor forming separate infinite chains. In the quantum dot (0D) analogue, where each $[PbI_6]^{4-}$ complex is neutralized by four cations to form a molecule.[5]

The great chemical flexibility of lead halide perovskites enables great structural tunability for functional material design, which provide a rich material database with varying physical properties for different applications.

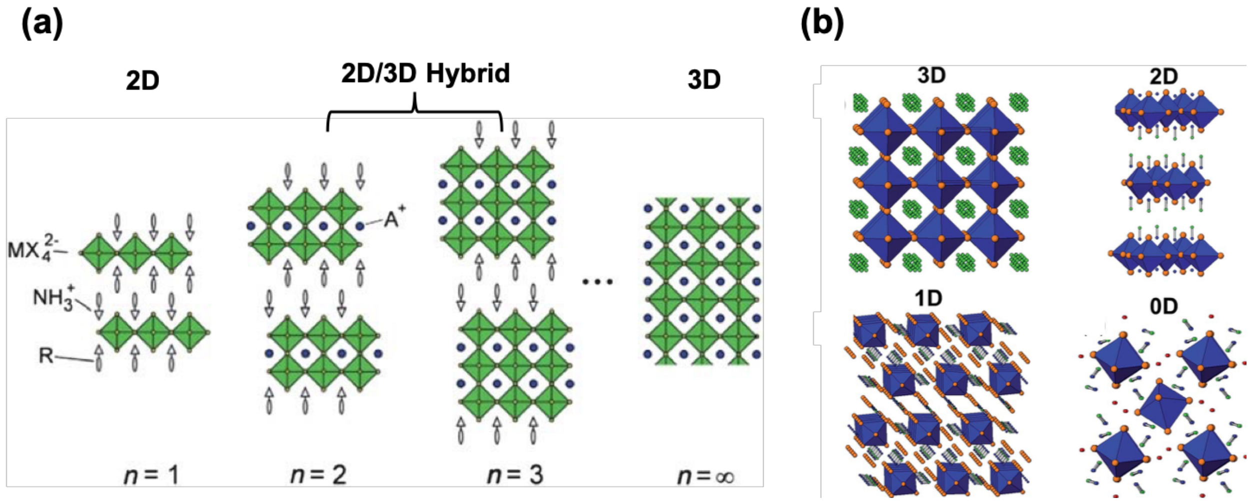

Figure 1.2. (a) The <100>-oriented hybrid perovskite series with general formula of $(RNH_3)_2A_{n-1}M_nX_{3n+1}$. The thicknesses of inorganic slabs increase and toward 3D structure with increasing n.[4] **(b)** Crystal structures of $CH_3NH_3PbI_3$, $(CH_3NH_3)_2PbI_4$, $(C_{10}H_{21}NH_3)_2PbI_4$, and $(CH_3NH_3)_4PbI_6{\cdot}2H_2O$ corresponding to 3D, 2D, 1D and 0D networks. The 1D network extends into the plane of the document.[5]

1.1.2 *Electronic Structure*

Optoelectronic properties including recombination mechanisms, mobility, and intrinsic carrier concentration are highly related to material's band structure and density of states (DOS). **Figure 1.3a** is a bonding diagram for the $[PbI_6]^{4-}$ cluster (zero-dimensional system). **Figure 1.3b** is the bonding diagram of the valence band (VB) and conduction band (CB) for 3D perovskite $MAPbI_3$ and 2D perovskite $(C_4H_9NH_3)2PbI_4$ crystals based on first principle density function theory (DFT) calculation.[6] The VB for the 3D crystal consists of the Pb 6s-I 5p σ-antibonding orbital, while the Pb 6p–I 5s σ-antibonding and Pb 6p–I 5p π-antibonding orbitals form the CB. It can be learned that both organic cation MA+ and $C_4H_9NH_3^+$ can effectively stabilize this perovskite structures, but do not make considerable contribution to the electronic structure of both 3D and 2D perovskites around the band edge. **Figure 1.3c** more clearly shows that MA molecule do not have any significant contribution around the band edge but donate one electron to Pb-I framework.[7] Thus, by tuning the composition of metal and halide sites, optoelectronic properties can be effectively tailored. Even though organic cation doesn't contribute to band edge, going from MA^+ to $C_4H_9NH_3^+$ thus 3D to 2D structure, band width is narrowed and band gap (E_g) is enlarged. Thus, composition engineering and structure tuning has been effective approaches to adjust perovskite properties which will be covered in later sections.

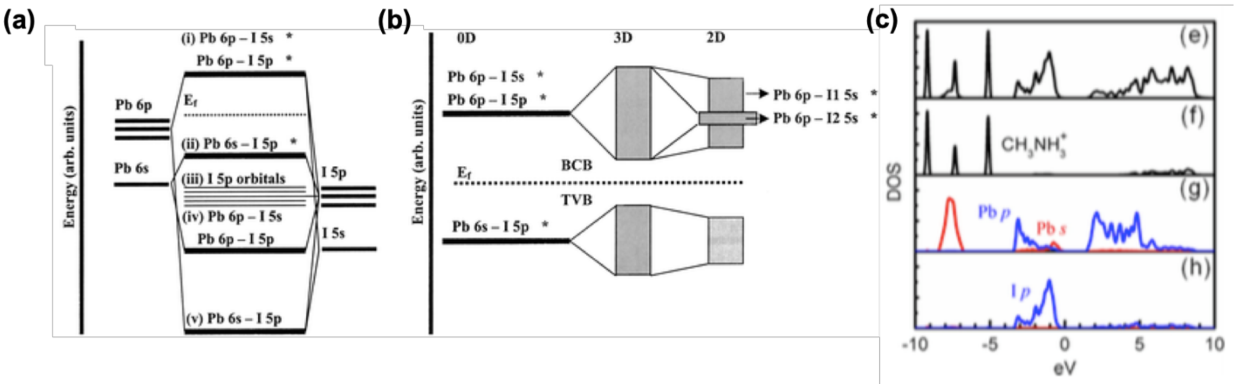

Figure 1.3. Bonding diagram of **(a)** $[PbI_6]^{4-}$ cluster (0D system), **(b)** 3D crystal $MAPbI_3$, and 2D crystal $(C_4H_9NH_3)_2PbI_4$ at the top of the VB and the bottom of CB.[6] **(c)** Band structure of $MAPbI_3$. Sub-figures are total DOS and MA^+, Pb, I partial DOS, respectively. The zero in DOS is referred to VB maximum. The Pb partial DOS has enlarged by five times for clear indication of s orbital contribution.[7]

1.2 TUNABLE OPTOELECTRONIC PROPERTIES OF PEROVSKITES

Perovskite materials possess flexible bandgaps that can be easily tuned through composition engineering. Within the three A, B, and X lattices sites, solid-solutions can be readily created by mixing different elements in each site.

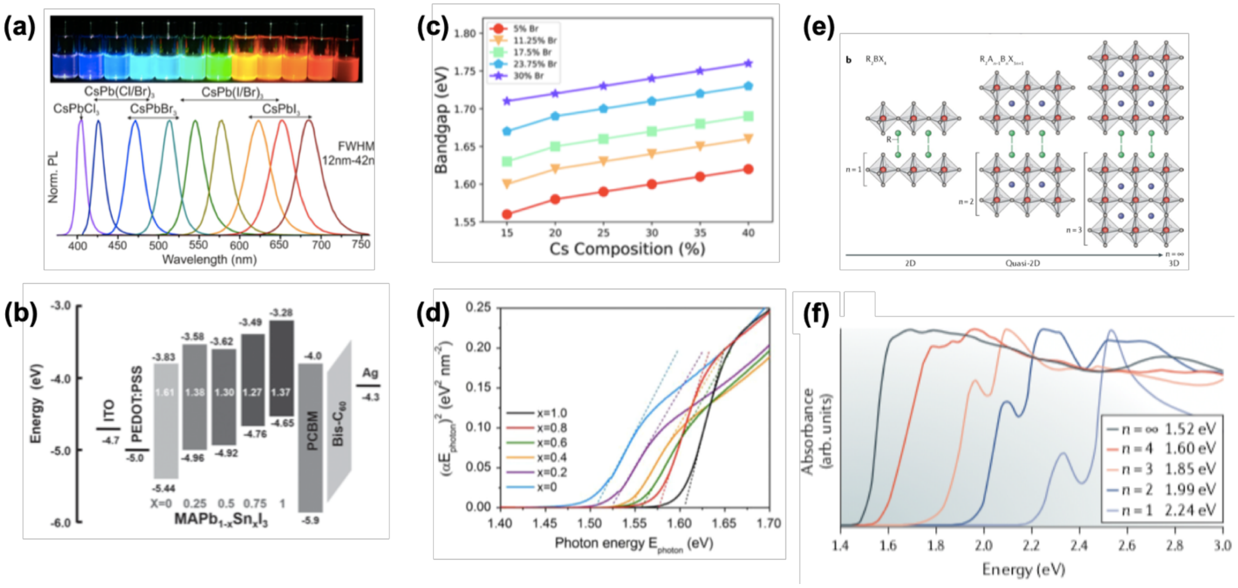

Figure 1.4. (a) Photoluminescence of $CsPbX_3$ (X = Cl, Br, and I) nanocrystals showing their broadband tunability.[8] **(b)** Energy-level diagrams of the compositional $MAPb_{1-x}Sn_xI_3$ perovskites.[9] **(c)** band gap vs perovskite composition for the $Cs_xFA_{1-x}Pb(Br_yI_{1-y})_3$ compositional space, showing a change in Cs along the x axis and a change in Br from 5-30% as separate lines.[11] **(d)** Kubelka–Munk spectra of $MA_xFA_{1-x}PbI_3$, where α is the absorption coefficient and Ephoton is the photon energy.[10] **(e)** Illustration of the structures of LD perovskites with different numbers of perovskite layers n. **(f)** Absorption spectra of quasi-2D $BA_2MA_{n-1}Pb_nI_{3n+1}$ perovskites (where BA^+ = butylammonium).[12]

As shown in **Figure 1.4a**, by mixing I, Br, Cl in different ratio, the E_g energies and emission spectra can be tuned over the entire visible spectral region of 410−700 nm,[8] showing great potential of perovskites as emitters. B-site alloying, taking the example of partial substitution of Pb with Sn in $MAPbI_3$ (**Figure 1.4b**), has been widely used to reduce the E_g from 1.5-1.6 to 1.2-1.4 eV.[9] When replacing MA^+ with FA^+ (**Figure 1.4d**), going from 0% to 100% FA^+ substitution the E_g reduced from 1.61 to 1.51eV.[10] MA^+ substitution with Cs^+ (**Figure 1.4c**) can instead increase the E_g.[11] Above two examples of A-site alloying still keeps the 3D framework. Through incorporating larger organic cations thus breaking 3D into 2D structure (**Figure 1.4e**), E_g can be greatly enlarged (**Figure 1.4f**).[12] The compositional versatility of perovskites opens up a significant opportunity to develop perovskite-perovskite tandem which requires both large and small E_g components.

The binding energy (E_b) of $MAPbI_3$ is comparable to or well below thermal energy at room temperature (k_b @ $T_{298\ K}$ =25.7 meV).[13] The majority photogenerated species in $MAPbI_3$ are free carriers, which is highly beneficial for photovoltaic (PV) applications. Excitonic contributions are generally more prominent in larger band gap materials as a result of reduced background screening, thus $ABBr_3$, $ABCl_3$, and their associated solid solutions.[14,15] In the case of LD OIHPs, quantum and dielectric confinement effect dramatically increase E_b. (**Figure 1.5**) Thus, utilizing Br-based perovskites and incorporation of large cation to introduce LD perovskites have been two common methods to increase radiative recombination efficiency for light emitting diodes (LEDs) applications.

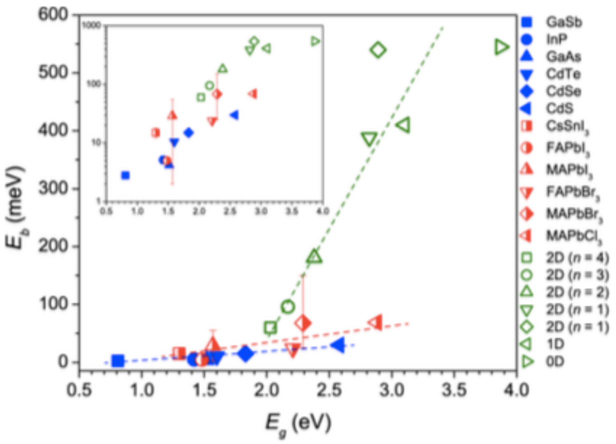

Figure 1.5. Empirical relationship between E_g and E_b in a number of 3D and LD OIHPs and selective conventional compounds. Inset shows the same data on a semi-log plot.

The charge diffusion length (L_D) and charge mobility are key parameters of a light absorbing material for application in solar cells. Thin films of 3D OIHPs possess extremely high charge-carrier mobility values considering its facile processibility. For mixed halide $MAPbI_{3-x}Cl_x$ polycrystalline thin film, the electron and hole diffusion length were characterized to be both over 1 μm with transient absorption and photoluminescence-quenching measurements.[16] $MAPbI_3$ and $MAPbBr_3$ single crystals showed a value of as long as 10 and 4.3 μm respectively.[17] In the same year, Dong *et al* achieved a diffusion length of 175 μm from $MAPbI_3$ single crystal under 1 Sun illumination.[18] The μm scale charge-carrier L_D under solar illumination densities highly exceeds the absorption depth of photons with energy larger than the band gap of perovskites, and this directly contributed for the high efficiency of perovskite thin film PV devices.

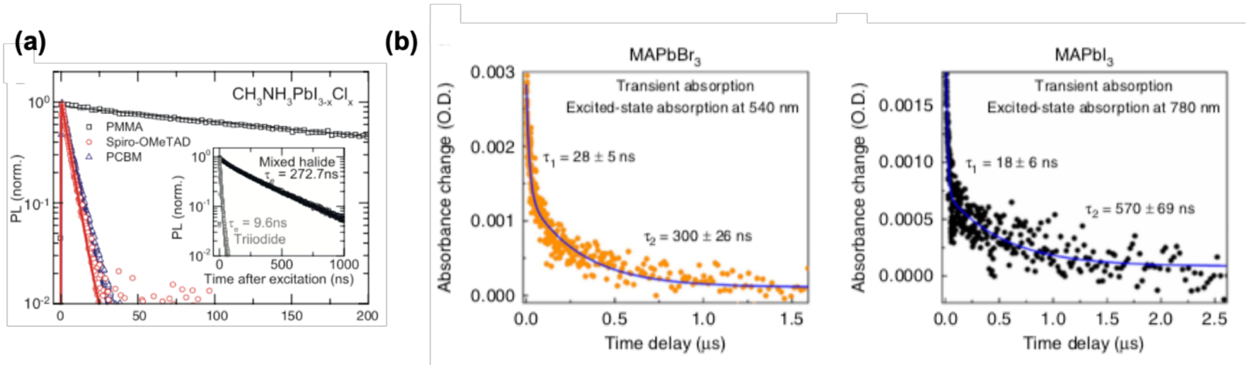

Figure 1.6. (a) Time-resolved PL measurements taken at the peak emission wavelength of $MAPbI_{3-x}Cl_x$ with an electron (PCBM; blue triangles) or hole (Spiro-OMeTAD; red circles) quencher layer. **(b)** Transient absorption of $MAPbBr_3$ and $MAPbI_3$ crystals.

Due to their outstanding optoelectronic merits as mentioned above, OIHPs are shown to be promising materials in various optoelectronic applications including PV, LED and photodetection devices. For 3D OIHPs especially, they possess high absorption coefficient, small exciton E_b (~kT), ambipolar charge mobility, and long charge carrier diffusion lengths. As shown in the National Renewable Energy Laboratory best solar cell efficiency chart (**Figure 1.7a)**, perovskite solar cells have seen a remarkable rise in PCE over a period of only a few years, now exceeding 22% (**Figure 1.7b**).[19,20] OIHPs have also demonstrated wide color tunability, size-insensitive high color purity, and good mechanical flexibility.[21] Within the last 2 years, external quantum efficiency (EQE) of perovskite LEDs have been boosted from 0.76% to 20.1% (**Figure 1.7c**).[22,23] Perovskites have also obtained tremendous attentions in lasers (**Figure 1.7d**) and photodetectors (**Figure 1.7e**).[24–26]

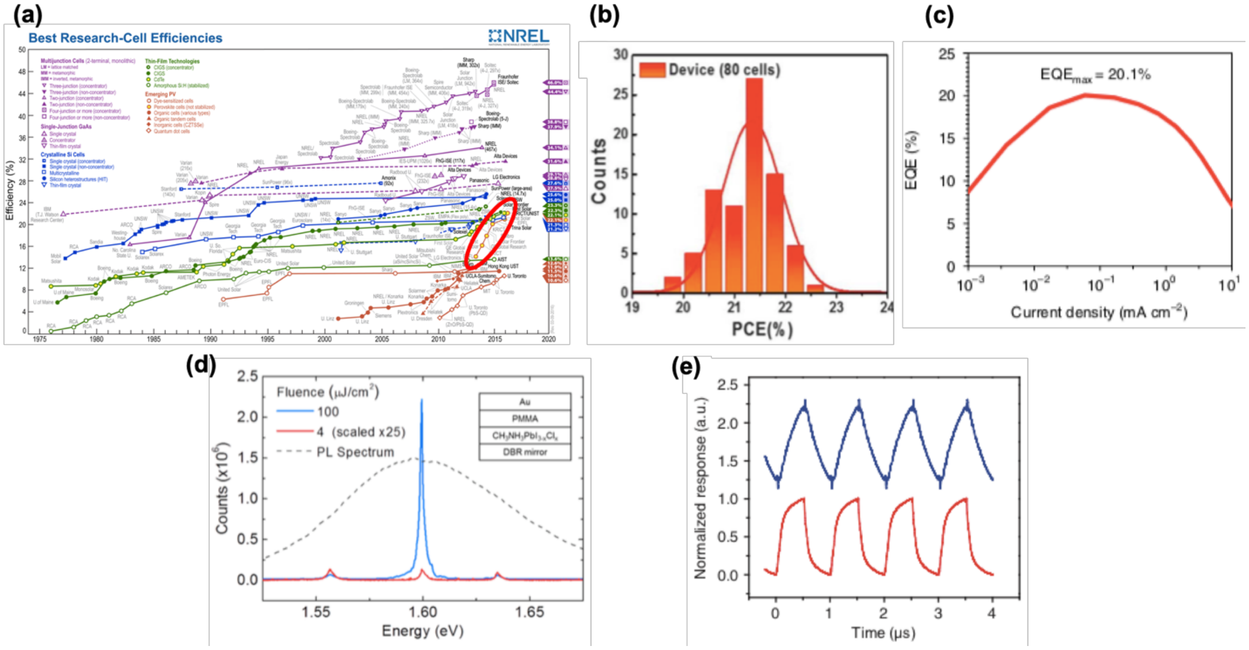

Figure 1.7. (a) National Renewable Energy Laboratory best solar cell efficiency chart **(b)** Histogram of the average power conversion efficiency determined for 80 perovskite solar cell devices with best device exceeds 22% PCE.[20] **(c)** EQE–current density characteristics of the best PPBH LED (peak EQE = 20.1%).[23] **(d)** Emission spectrum of a vertical microcavity with the structure as shown in the inset using a perovskite film as the gain medium.[25] **(e)** Transient photocurrent response at a pulse frequency of 1 MHz with a photodetector device area of 0.1 cm2 (blue line) and 0.01 cm2 (red line).[26]

1.3 CURRENT CHALLENGES AND RESEARCH FOCUS

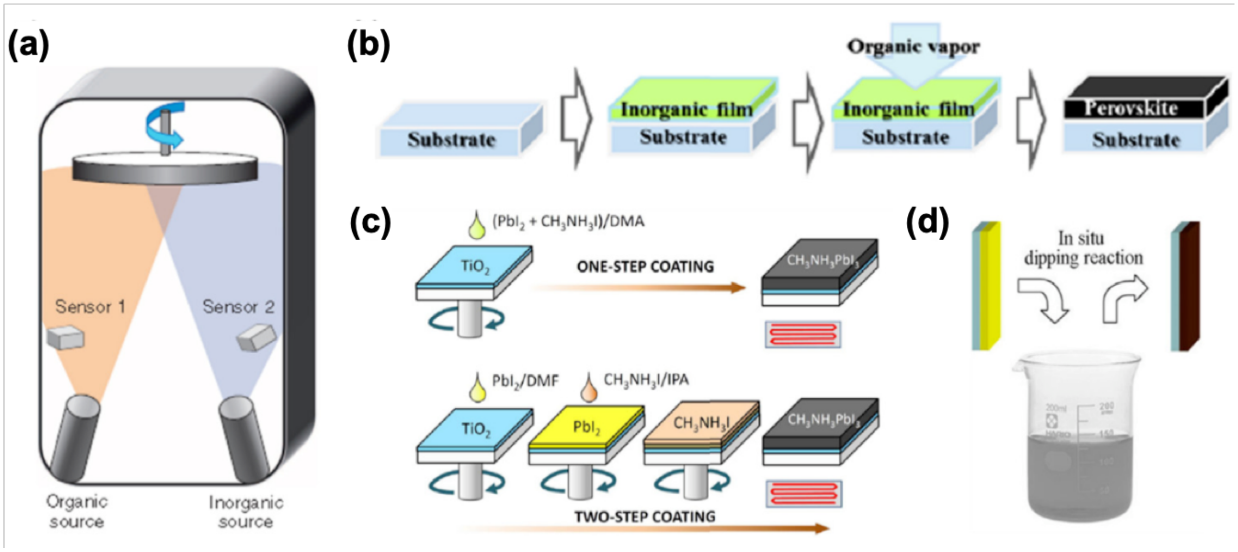

Figure 1.8. The preparation of $MAPbX_3$ films using different deposition methods: **(a)** dual source co-evaporation using $PbCl_2$ and MAI sources; **(b)** vapor-assisted solution process using MAI organic vapors to react with pre-deposited PbI_2 films **(c)** single-step solution processes based on a mixture of PbI_2 and MAI, and sequential coating of PbI_2 and MAI; **(d)** sequential deposition by dipping the PbI_2 film into MAI solution.[27]

Although OIHPs possess low-cost solution processability, a factor that makes them serious rivals for existing photovoltaic materials, this facile processing comes at the cost of complex and competing growth processes that frustrate control of film quality and coverage. Pin-hole formation, low crystallinity, and phase inhomogeneity are common obstacles to carrier transport and ultimate device performance. Crystallization is a complex process that involves two main steps – nucleation and growth. Nucleation from a continuous phase can occur homogeneously or heterogeneously. Nucleation barrier is much lower for heterogeneous compared to homogeneous nucleation. Thus, nucleation and growth of perovskite crystals will occur more easily when the solution is deposited on substrates with larger surface area. Compared to the mesoporous-structure based device configuration, morphological control is more challenging for the planar heterojunction (PHJ) structure because of its lower surface area caused by the lack of porosity. Nevertheless, the PHJ configuration still attracts significant research interests due to the versatility of emerging low-temperature fabrication techniques and materials. Therefore, effective ways to manipulate nucleation and growth of perovskite crystals in solution-processed systems, particularly in planar systems, in order to achieve optimum film morphology are highly sought after.

Apart from the standard one step spin-coating process, several methods have been developed (**Figure 1.8**) to better control perovskite nucleation and growth.[27] Sequential deposition from solution,[28-29] dual-source evaporation,[30] and the vapor-assisted solution process[31] all use a variety of phase transformations to circumvent direct perovskite growth from solution. For example, solution and vapor-based two-step deposition methods both utilize a compact lead halide template to encourage uniform growth, eliminating the complexities inherent in direct $MAPbI_3$ growth.

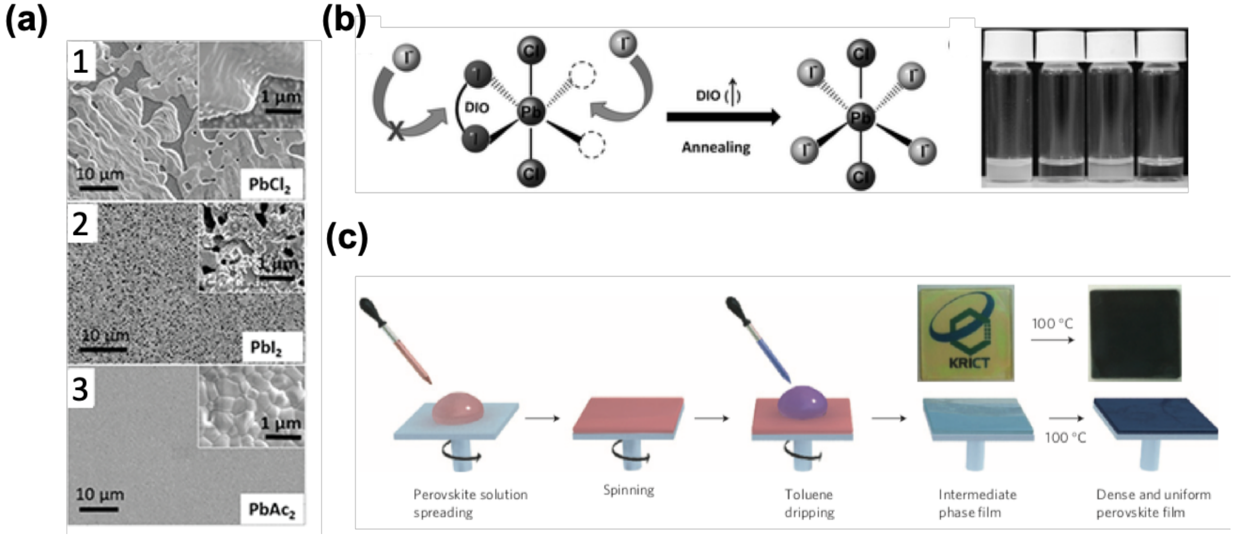

Figure 1.9. (a) SEM images of methylammonium lead iodide made using $PbCl_2$ (1), PbI_2 (2), and PbAc2 (3) as the lead source.[34] **(b)** Schematic diagram for the transient chelation of Pb^{2+} with DIO, and solubility of the $PbCl_2$ and PbI_2 in DMF with or without additives.[35] **(c)** Solvent engineering procedure for preparing the uniform and dense perovskite film.[37]

To control this complexity rather than avoid it, techniques have focused on thermal processing[32] and compositional tuning of the precursor solution through spectator ions (**Figure 1.9a**),[33-34] additives (**Figure 1.9b**),[35,36] and co-/anti-solvents (**Figure 1.9c**),[37] all of which provide improved film morphology through kinetic control of competing growth processes.[38]

Despite the significant improvements these strategies offer, the complexity of competing processes implicit in growth hinder reproducibility and mechanistic understanding. These challenges have motivated the development of many post deposition treatments that expand upon simple thermal annealing,[39] such as solvent annealing,[40] multi-cycled dimethylformamide (DMF) vapor treatment (**Figure 1.10b**),[41] and hot-pressing (**Figure 1.10a**).[42] While these post treatments markedly improve film morphology, they are relatively time-consuming and complex. Efficient, reproducible techniques are necessary to access the high throughput fabrication the material's solution processability enables.

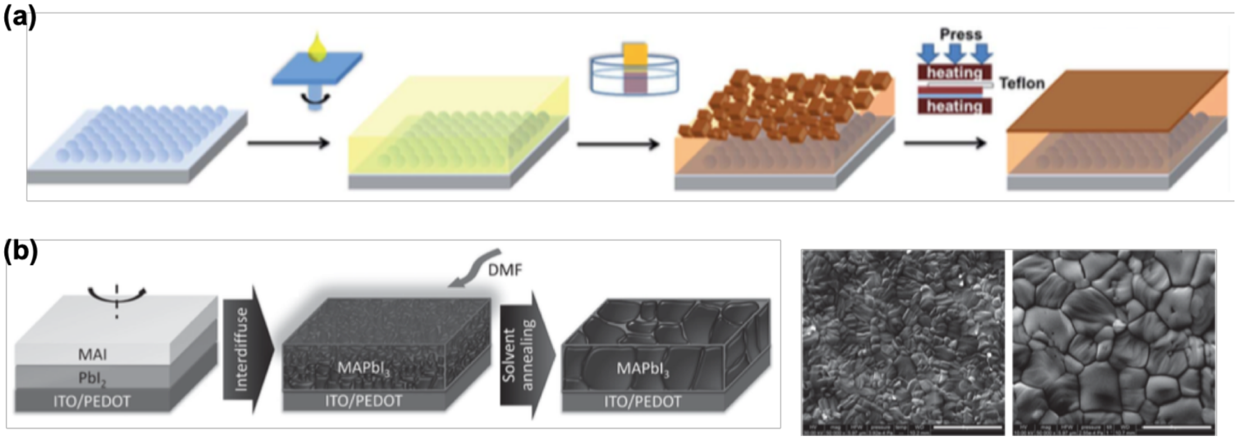

Figure 1.10. (a) Preparation procedure of perovskite $CH_3NH_3PbI_3$ on FTO/mesoporous TiO_2.[42] **(b)** Schematics of the interdiffusion approach and solvent-annealing-induced grain size increase. Two SEM images on the right compares film morphology before and after solvent annealing.[40]

Besides morphology control being a challenging aspect, substantial structural disorder and crystallographic defects (**Figure 1.11a**) inside polycrystalline perovskite thin film as a consequence of solution process is also crutial.[43–45] Several reports have identified the prevalence of vacancy and interstitial defects in OIHP thin films due to their low formation energies.[7,46–48] In an ionic crystal such as OIHP, dangling bonds at the surface and GBs introduce trap states and non-radiative recombination centers. Polycrystalline nature of solution-processed OIHP films further aggravates this issue because of increased GB density and structural disorder, in contrast to a single-crystalline perovskite that shows an extremely long electron-hole diffusion length of 175 μm.[18]

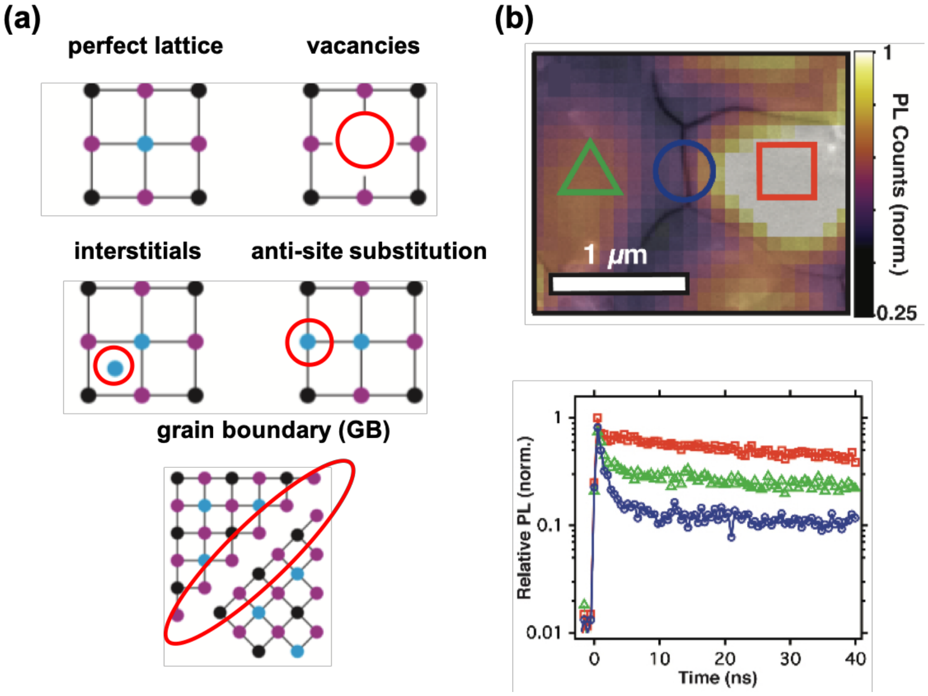

Figure 1.11. (a) Defects in a perovskite crystal lattice (blue, black, and purple dots represent the A-, B-, and X-site ions, respectively.[45] **(b)** Fluorescence image of $CH_3NH_3PbI_3(Cl)$ film on glass showing PL intensity variations at a bright grain (red square), grain boundary (blue circle), and dark grain (green triangle), and time resolved photoluminescence traces showing grain boundaries (blue circle) quench PL significantly more than dark (green triangle) and bright regions (red square).[52]

Several studies have manifested that surface defects and GBs can serve as photoluminescence (PL) quenching sites (**Figure 1.11b**) and thus result in loss of photo-generated carriers.[49–52] Additionally, vacancy defects provide a pathway for ion migration, which adversely affects the charge collection and results in current-voltage hysteresis.[53–56] Ion migration become more pronounced in a at GBs due to higher diffusivity of ions across these extended defects.[57] Therefore, effective mitigation of defects in the solution-processed perovskite films is an important research subject to further enhance the performance of PSCs towards their thermodynamic limits.

Chapter 2. METHODOLOGY

This chapter describes the experimental details including materials and thin film preparation, device fabrication and characterization methods commonly shared by chapter 3,4 and 5 in this thesis.

2.1 SYNTHETIZATION OF PEROVSKITE FILMS

2.1.1 *Purchased material sources*

Indium tin oxide (ITO) glasses were purchased from TFD Inc. (for 6.08mm^2 devices) and Colorado Concept Coatings LLC. (for 3.14mm^2 and 14mm^2 devices). PEDOT:PSS were purchased from Heraeus (Clevis P VP Al 4083). TPBI and poly-TPD were purchased from Lumtec. All other materials were purchased from Sigma-Aldrich.

2.1.2 *Synthesis of ammonium salts*

CH_3NH_3I (MAI) was synthesized by reacting 33 wt% CH_3NH_2 in ethanol with 57% HI in water solution at a 2:1 molar ratio of CH_3NH_2 to HI and 0ºC for 2h.[58] The product was collected by removing solvent through rotary evaporation, followed by diethyl ether washing until colorless and recrystallized twice in methanol. The crystalline white powder was finally dried in a vacuum oven at 60 ºC for 24 h.

$CH_3(CH_2)_3NH_3I$ (C4-mono-I) and $C_6H_5(CH_2)_2NH_3I$ (PEAI) were synthesized and purified in a similar way except that C4-mono and PEA are mixed with HI at a 1:1.1 molar ratio in ethanol.

$NH_3I(CH_2)_4NH_3I$ (C4-di-I$_2$), $NH_3I(CH_2)_8NH_3I$ (C8-di-I$_2$), $NH_3I(CH_2)_2O(CH_2)_2O(CH_2)_2NH_3I$ (EDBE-di-I$_2$) are synthesized and purified in a similar way except that $NH_2(CH_2)_4NH_2$,

$NH_2(CH_2)_8NH_2$ and $NH_2(CH_2)_2O(CH_2)_2O(CH_2)_2$ NH_2 are mixed with HI at a 1:1.2 molar ratio in ethanol respectively.

2.2 DEVICE FABRICATION

2.2.1 *Substrate cleaning*

ITO glass substrates were cleaned sequentially with detergent, deionized water, acetone, and isopropanol under sonication for 10 min each. After drying under a N_2 stream, substrates were further cleaned by a ultraviolet (UV) ozone treatment for 10 min.

2.2.2 *Fabrication of PSCs*

PSC processed from MA^0 vapor treatment: PEDOT:PSS solution filtered through a 0.45 µm nylon filter was first spin-coated onto the ITO substrates at 5k rpm for 30 s and annealed at 150 °C for 10 min in air. To avoid any possible influence from oxygen and moisture, the substrates were transferred into a N_2-filled glovebox. The perovskite precursor solution was made by dissolving an equimolar ratio of PbI_2 (1 M) and MAI (1 M) in DMF at 60°C and filtering through 0.45µm PTFE filter. Perovskite layers were formed by spin-coating the precursor solution at 6k rpm for 45s and then annealing at 100ºC for 15 min. After annealing, MA^0 vapor treatment was conducted by holding the perovskite film upside down right above a 20 mL open vial (28 mm outer diameter x 61 mm height and 22 mm aperture diameter) with 6 mL of 33 wt% CH_3NH_2 solution in ethanol at room temperature. Upon turning clear (less than 1s), the film was immediately removed vertically. Rapid vertical removal of the film from the MA^0 vapor source is important to prevent inhomogeneities that develop when the film is moved laterally through a MA^0 concentration gradient. The film was annealed again at 100 ºC for 15 min to further increase thin-film crystallinity. Atop the $MAPbI_3$ film, C_{60} (15 mg/ mL in ortho-dichlorobenzene (DCB)) and

C_{60}-bis surfactant (2 mg/mL in isopropyl alcohol) were sequentially deposited by spin coating at 1k rpm for 60 s and 3k rpm for 60 s, respectively. Silver electrodes with a thickness of 120 nm were finally evaporated under vacuum (<2 x 10^{-6} Torr) through a shadow mask. The device area was defined as 3.14 mm^2.

PSC processed from solvent washing method: Cu-doped NiOx precursor[59] were spin coated onto the cleaned ITO substrate at 3000 rpm for 60 s and annealed at 400 °C for 1 h in air. The perovskite precursor solution was made by dissolving an equimolar ratio of PbI_2 (1 M) and MAI (1 M) into a mixed solvent of dimethyl sulfoxide (DMSO) and gamma-butyrolactone (GBL) (volume ratio of 3:7) at 60°C and filtering through 0.45µm PTFE filter. Perovskite layers were formed by spin-coating the precursor solution at 1000 rpm for 15 s and 4000 rpm for 45 s sequentially. During the last 15 s of the second spin-coating step, the substrate was treated with toluene drop-casting (0.7 mL). The resulting thin films were annealed at 100°C for 10 min. After annealing, the film was cooled down to room temperature. C4-di-I_2, C8-di-I_2 and EDBE-di-I_2 were dissolved in isopropyl alcohol (IPA) in a concentration of 1 mg/mL, 2 mg/mL and 2 mg/mL respectively. 20mL vials with 3mL solution in it were used for post treatment through 10s immersion. Following that the substrate was blow dried by N_2 blow gun and further immersed in a 20mL vial containing 3mL IPA for 2s washing followed by N_2 blow gun drying. Atop the $MAPbI_3$ film, PCBM (15 mg/ mL in chloroform (CF)) and C_{60}-bis surfactant (2 mg/mL in IPA) were sequentially deposited by spin coating at 4k rpm for 30 s and 3k rpm for 30 s, respectively. Silver electrodes with a thickness of 150 nm were finally evaporated under vacuum (<2 x 10^{-6} Torr) through a shadow mask. The device area was defined as 3.14 mm^2.

2.2.3 *Fabrication of perovskite LEDs*

After PEDOT:PSS solution were spin coated onto the cleaned ITO, the substrates were then transferred to N_2 filled glovebox for further fabrication process. 0.3M $(PEA)_2PbBr_4$ solution in DMF was then spin-coated on top at 5k rpm for 50s followed by thermal annealing at 100°C for 10 min. The thin films were then treated with ion exchange processing as described above, except that 10mg/mL MABr was used here instead of MAI. Thickness of $(PEA)_2PbBr_4$ and $MAPbBr_3$_ex thin film is ~170nm and ~100nm respectively. Atop the $MAPbBr_3$, 30nm TPBI and 1nm LiF were sequentially evaporated under vacuum ($< 1 \times 10^{-6}$ Torr). Aluminum electrodes with a thickness of 120nm were finally evaporated under vacuum ($<4 \times 10^{-7}$ Torr) through a shadow mask.

2.3 CHARACTERIZATION METHODS

2.3.1 *Characterizations of perovskite materials and films*

1D XRD: X-ray diffraction (XRD) experiments with 1D detector were performed using a Bruker F8 Focus Powder XRD operating at 40 kV and 40 mA with a Cu K-alpha (1.54 A) X-ray source.

2D XRD: XRD experiments were performed using a Bruker D8 Discover Microfocus operating at 50 kV and 1000 μA with a Cu K-alpha (1.54 A) X-ray source. Gamma scans were performed by setting the incidence angle to half of the 2θ value for the diffraction peak to be analyzed. After the measurement, we use EVA Software to integrate the diffraction intensity over the selected 2θ range which covers the whole diffraction peak.

UV-vis absorption: The absorbance spectra were measured by a Varian Cary 5000 UV–vis-NIR spectrometer. The absorptance spectra (equivalent to fraction of absorbed light, F_A) measured in Chapter 5 used the internal diffuse reflectance accessory (integrating sphere) on a Cary 5000i UV–vis-NIR spectrometer. The integrating sphere was used to measure the near-normal incidence total reflectance (R) and normal incidence transmittance (T) spectra of films on glass substrates, and F_A was calculated as 1-R-T. The absorptance data is shown only in the spectral region where F_A of the glass substrate ≈ 0.

Time-resolved photoluminescence (TRPL): TRPL decay traces were acquired by a time-correlated single photon counting (TCSPC) system (FluoTime 100, PicoQuant GmbH). Samples were photoexcited using a 467 nm laser beam (LDH-P-C-470, PicoQuant GmbH) pulsed at frequencies between 0.5-10MHz, with a pulse duration of 60 ps and fluence of ~10 nJ/cm2. The lifetime was obtained by fitting the PL measured from perovskite films with a bi-exponential decay function of the form:

$$\mathrm{I(t)} = A_1 \exp\left(-\frac{t}{\tau 1}\right) + A_2 \exp\left(-\frac{t}{\tau 2}\right) \tag{2.3}$$

Steady state photoluminescence: For steady state PL measured in chapter 3, a 470 nm pulsed diode laser (PDL-800 LDH-P-C-470B, 300 ps pulse width) was used for excitation at a fluence of 10 nJ/cm^2 ($n_0 \sim 10^{15}$ cm^{-3}) with a repetition rate of 500 kHz for time resolved measurements and a continuous-wave 532 nm (CrystaLaser, GCL532-005-L) at a power density of 90 mW/cm^2 (~1.5 sun) was used for steady state measurements. Samples were excited face-on (not through the substrate) and the emission was filtered through a 700-850 nm bandpass filter (700 LP and 850 SP). Photoluminescence from the sample was directed to a Micro Photon Devices (MPD) PDM Series single photon avalanche photodiode with a 50 µm active area for TRPL measurements or a portable charge coupled device spectrometer (USB2000, Ocean Optics) for steady state PL measurements.

In chapter 5, the PL spectra were measured on a home-built set up consisting of a LN_2 cooled Si CCD detector (Princeton Instruments Spec-10) coupled with a spectrograph (Princeton

Instruments 2300i). For PL measurements, the films were excited using a 488 nm CW laser (CrystaLaser DL488-020-O) with a 1mm diameter collimated beam at an intensity of ~30mW/cm^2. PL was measured with the samples mounted in a custom built optical vacuum chamber, and the set up was aligned such that emission at the excitation spot was imaged onto the spectrometer entrance slit using lenses matched to the f/# of the spectrograph. The PL spectra were spectrally corrected for the spectrometer response using a calibrated white light source (Ocean Optics HL-3P-CAL-EXT).

Secondary electron microscopy (SEM) images were taken with a FEI Sirion scanning electron microscope at 5 kV.

Transmission electron microscopy (TEM): TEM samples of MA^0 treated perovskites (chapter 3) were prepared by first adhering a finder TEM grid with a Carbon B coating to a cleaned ITO glass substrate (specifically EF400-Ni from Electron Microscopy Services). Before mounting, grids were glow discharge treated for 30 seconds with an oxygen/hydrogen plasma with a Solarus 950 Gatan Advanced Plasma System. The grid is mounted in slight tension on a glass slide with scotch tape to ensure intimate thermal contact. The same deposition and heat treatment procedure for first PEDOT:PSS then the desired perovskite are followed as above with the exception of the use of a 0.4 M perovskite precursor solution. Vapor exposure was also identical except for the use of a MA^0 vapor source with a smaller aperture (4 ml vial with a 10 mm diameter neck rather than 20 ml with a 22 mm diameter neck) for high vapor pressure exposure. When the grid is removed from the glass slide for characterization, the points of contact between the tape and the grid are carefully cleaned with IPA to prevent contamination of the high vacuum environment of the TEM. A Tecnai G2 F20 transmission electron microscope was used at 200 kV for all TEM measurements.

Ultraviolet photoelectron spectroscopy (UPS): UPS measurements were performed by a Kratos Axis Ultra DLD photoelectron spectrometer with an incident radiation of He I (21.2 eV).

X-ray photoelectron spectroscopy (XPS): XPS spectra were generated using a PHI Versaprobe system with an Al Kα X-ray source and a 100μm beam size. Measurements were taken while the sample was under ultrahigh vacuum (10^{-10} Torr).

Computation Methods: The VASP[60,61] code is employed to optimize the structures and calculate the related energies of the $MAPbI_3$ and (C4-di)-, $(C4\text{-mono})_2$-, $(PEA)_2$- and (EDBE)-PbI_4 perovskites. The Perdew-Burke-Ernzerhof (PBE) exchange correlation functional and the projector-augmented wave (PAW) method are used.[62,63] The wavefunctions are expanded in plane waves with an energy cutoff of 500 eV. K-meshes have been used to sample the Brillouin zone during the optimization. The convergence criterion of the total energy is set to 10^{-8} eV. The total force on each atom in the system need to be less than $5*10^{-3}$ eV/Å.

2.3.2 *Characterizations of PSCs*

All *J–V* curves were recorded using a Keithley 2400 source meter unit. The device photocurrent was measured upon illumination from a 450 W thermal Oriel solar simulator (AM 1.5G) calibrated with a standard Si photodiode detector equipped with a KG-5 filter, which can be traced back to the standard cell of the National Renewable Energy Laboratory.

2.3.3 *Characterizations of perovskite LEDs*

The electroluminescence (EL) spectrum was measured using a Konica Minolta spectroradiometer CS-2000. LED EQE, J-V-L, and current efficiency measurements were made using a homebuilt set up that consisted of a large area calibrated Si photodiode (Hamamatsu S3204-08) mounted in a light-tight enclosure inside of a N_2 glovebox. The LED EQE set up was designed based on the principle of “under filling” a large area detector. The device holder was designed such that waveguided emission was effectively blocked from the detector. A Keithley 2400 source meter unit was used to bias the LED and measure the current density (J), while a Keithley 237 source meter simultaneously measured the short circuit photocurrent from the Si photodiode. Luminance, EQE, and current efficiency were then calculated considering the EL spectrum and spectral responsivity of the detector.[64]

Chapter 3. METHYLAMINE VAPOR BASED HYBRID PEROVSKITE POST DEPOSITION TREATMENT

This chapter presents a facile post deposition treatment utilizing coordination between MA^0 vapor and $MAPbI_3$ perovskite that rapidly improves film quality, enhancing PCE by ~9%. The following material is reproduced from the article titled *Design Rules for the Broad Application of Fast (< 1 s) Methylamine Vapor Based, Hybrid Perovskite Post Deposition Treatments*.[65] This publication is co-first authored with Spencer T. Williams.

3.1 INTRODUCTION

As been discussed in the chapter 1, different processing methods or post-treatment techniques have been developed to optimize perovskite layer morphology. While these post treatments markedly improve film morphology, they are relatively time-consuming and complex. Efficient, reproducible techniques are necessary to access the high throughput fabrication the material's solution processability enables. In this work, we describe a fast (<1s) and simple post deposition chemical treatment in which crystal reconstruction induced by a MA^0 vapor greatly improves perovskite film coverage, crystallinity, and device performance. We not only demonstrate the efficacy of this chemical treatment in improving the photovoltaic performance of a PHJ device, we also mechanistically study the process to reveal the role of hydrogen bonding between methylamine vapor and the perovskite's organic sublattice in mediating the material's reactivity toward the vapor through the exploration of a variety of hybrid perovskite systems. Furthermore, through detailed microscopy, we also demonstrate that the nature of MA^0-perovskite coordination and its microstructural consequences are a function of MA^0 vapor pressure, interaction time, and composition of the organic sublattice. Ultimately, we offer design rules for amine vapor-based hybrid perovskite post chemical treatments.

3.2 RESULTS AND DISCUSSION

3.2.1 *Vapor treatment and its physical consequences*

Inspired by work reported by Zhu *et al.*[66] in which a reversible perovskite phase transformation upon exposure to amine gas was revealed, we speculated that this kind of chemistry can be utilized to establish a facile post deposition treatment to improve perovskite crystallinity and quality through the recrystallization responsible for the regeneration of the perovskite phase from a similar transparent intermediate state. To explore this concept, we used methylamine rather than amine vapor because of its increased similarity to species (MA^+) already within the $MAPbI_3$ lattice. To apply this in a device context, we fist prepared a $MAPbI_3$ film through simple one-step spin coating from DMF atop PEDOT:PSS, and then exposed this film to MA^0 vapor (**Figure 3.1a**). Immediate loss of pigment was observed in the perovskite upon introduction to a MA^0-rich environment followed by rapid reversal back to perovskite upon removal of the film from the vapor. Herein, PEDOT:PSS serves as a hole-transporting layer (HTL) in our devices, but it also provides the necessary interfacial energy to prevent film dewetting during vapor treatment. This is an important component of this treatment's success in the PHJ architecture as compared to the findings of Cui *et al.* reported on a mesoporous growth substrate where capillary action helps direct material diffusion.[67]

This technique potentially enables the use of one-step solution processing without the meticulous control typically required for high quality material growth. To apply this methodology broadly at many scales with many materials, we need a rigorous physical and chemical understanding of the process as a whole. Macroscopically, XRD suggests that perovskite crystallinity markedly increases upon vapor exposure and subsequent annealing at 100 °C for 15 min (**Figure 3.1b**). SEM of the film before and after vapor treatment (**Figure 3.1c-f**) reveals massive material diffusion resulting in almost complete film coverage, a huge improvement over the very poor coverage generated by unmodified 1-step perovskite growth from solution. It should be noted that ethanol itself does not induce any color or morphology change of the prepared $MAPbI_3$ thin film, thus the reaction results solely from MA^0. While key to the utility of the process, these two insights leave a significant hole in our understanding: What within the material is changing and how is it affecting performance and photophysical properties?

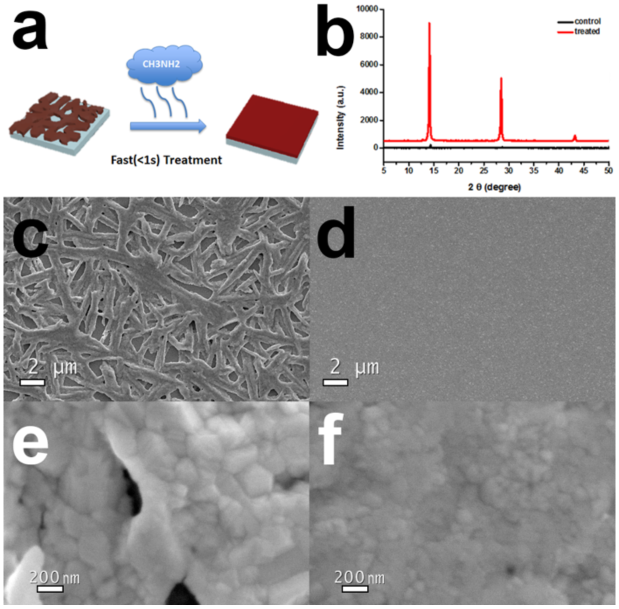

Figure 3.1. Comparison of a $MAPbI_3$ film before and after the vapor process in **(a)**: **(b)** XRD, **(c)-(d)** SEM low magnification, and **(e)-(f)** SEM high magnification.

To address this, we first generated PHJ devices with the configuration in **Figure 3.2a**. Control devices fabricated with unmodified 1-step perovskite growth from DMF showed a low PCE of ~3%, but after the simple vapor treatment devices reached 12% PCE through marked increases in all photovoltaic parameters (**Figure 3.2b, Table 3.1**). From XRD and SEM (**Figure 3.1**), this is likely due to a combination of shunt pathway elimination through improved film coverage and possible material enhancement.

Table 3.1. Photovoltaic performance values of the control and treated devices shown in Figure 2d (outside the parenthesis) and the average value with deviation calculated from 10 representative devices (inside the parenthesis).

	Voc (V)	Jsc (mA/cm^2)	FF	PCE (%)
Control	0.62 (0.63 ± 0.06)	11.23 (11.73 ± 1.64)	0.47 (0.48 ± 0.01)	3.27 (3.46 ± 0.30)
Treated	0.85 (0.83 ± 0.02)	17.59 (16.48 ± 1.17)	0.81 (0.80 ± 0.01)	12.08 (10.92 ± 0.81)

To better understand how MA^0 vapor treatment affects the photophysical properties of $MAPbI_3$, we studied the PL decay kinetics from perovskite films on glass. **Figure 3.2c** shows representative PL decays of the perovskite before and after MA^0 vapor exposure on glass measured in air. After MA^0 treatment, the PL decay is faster and the PL intensity is slightly decreased (**Figure 3.2d**). Since we do not see an increase in the PL lifetime or integrated intensity indicative of defect annihilation or surface passivation we conclude that while MA^0 vapor treatment may improve device performance by removing macroscopic film defects (e.g. pinholes) as observed in SEM (**Figure 3.1**), it does not effectively eliminate the structural defects responsible for non-radiative recombination losses.

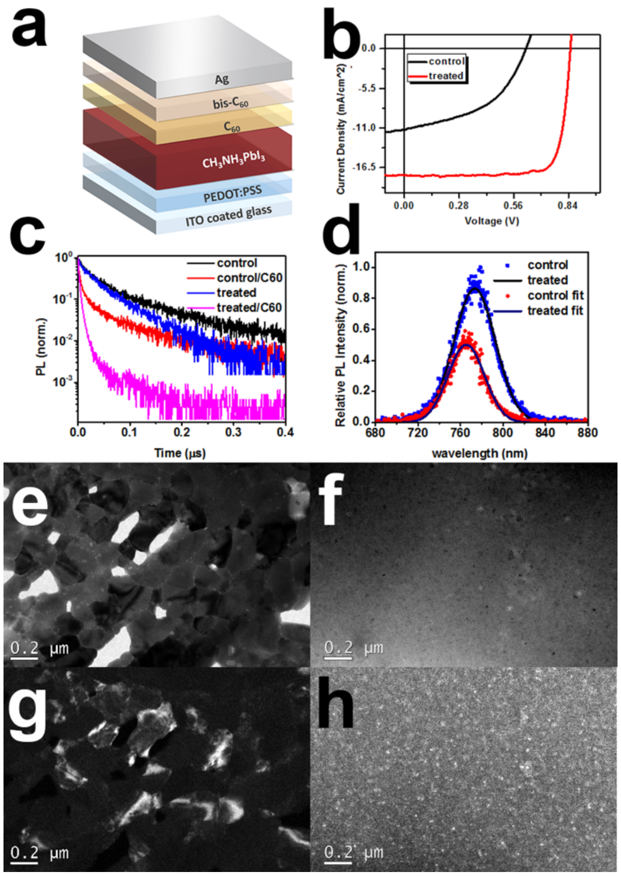

Figure 3.2. The J-V curve of the planar heterojunction photovoltaic device architecture in **(a)** with and without MA^0 vapor treatment is in **(b)** $MAPbI_3$'s photophysical quality as an absorber before and after vapor treatment is analysed with **(c)** transient and **(d)** steady state PL spectroscopy. With transient PL spectroscopy, we examine both the material on glass and on C_{60}. **(e)-(f)** and **(g)-(h)** are bright and dark field TEM images, respectively, of an identical region before and after vapor exposure.

In the steady state PL spectrum in **Figure 3.2d**, MA^0 treated films show a slight reduction in the PL intensity, consistent with the lifetime measurements. We also observe a ~ 7 nm blue-shift upon vapor treatment, and also ~10% reduction in the FWHM (**Figure 3.3**). We observed similar trends for films encapsulated with poly (methyl methacrylate) (PMMA) in a nitrogen atmosphere, suggesting that the reduction in PL is intrinsic to the MA^0/perovskite interaction and not a result of improved diffusion to (and quenching at) the perovskite/air interface. The correlation with improved crystallinity in the films studied and the PL shift may suggest a link between disorder and emissive states within the band gap, but the shift is small enough to have multiple possible origins.[68]

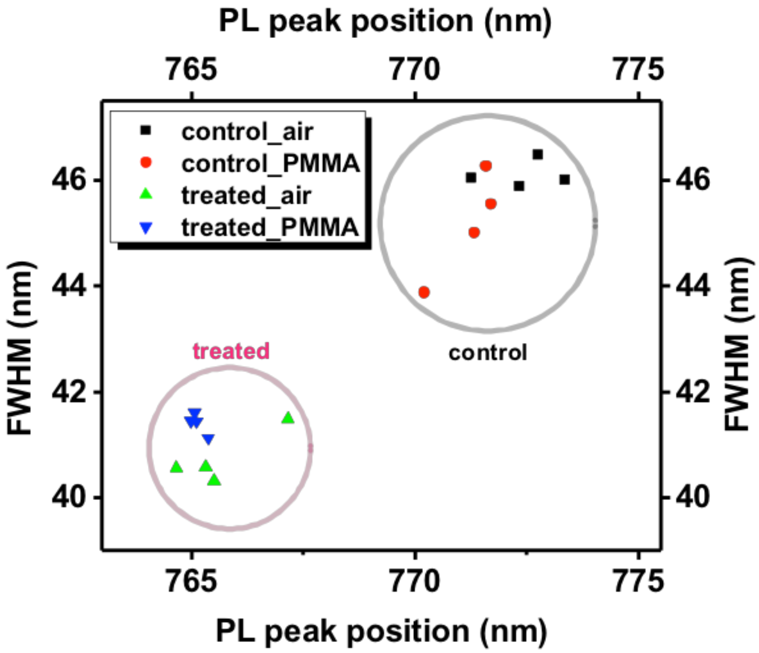

Figure 3.3. Gaussian fitting of the steady state PL spectra yields a parameter plot of the PL peak position and FWHM of $MAPbI_3$ films on glass before treatment (black), before treatment with PMMA on top (red), after treatment (green), and after treatment with PMMA on top (blue).

While intrinsic material properties are important, comparison of PL quenching before and after interfacing the material with a charge extraction layer is more immediately relevant to device performance. We constructed a perovskite/C_{60} bilayer film and found that vapor treated films quenched photogenerated charges more efficiently (~ 90 % quenching) than untreated films (~ 75 % quenching), which is evidenced by the faster PL decay (**Figure 3.2c**). In the treated films, these data suggest the charge transfer process to C_{60} is more efficient in treated films and likely outcompetes any additional non-radiative pathways introduced after MA^0 vapor treatment. We attribute faster PL decay to the increased interfacial quality between perovskite and C_{60} in vapor treated films. In contrast, Cui *et al.*[67] observed an increase in photoluminescence intensity after vapor treatment for films on compact TiO_2, which is opposite to what one would expect for more efficient charger transfer in MA^0 treated films.

These data illustrate an important device relevant consequence of MA^0 vapor treatment, but it leaves significant questions about the microstructural consequences of this process. Thus, we fabricated perovskite thin-films for TEM *via* a methodology identical to that used for device fabrication with the exception of using a diluted perovskite solution and a PEDOT:PSS coated TEM grid substrate.

Although it may be tempting to conclude from SEM that grain size doesn't change greatly upon MA^0 vapor treatment (**Figure 3.1e-f**), bright and dark field TEM (**Figure 3.2e-f** and **g-h** respectively) reveal that vapor treatment induces gain size reduction rather than growth by more than an order of magnitude. Final microstructure after MA^0 vapor treatment can be best described as a densely packed distribution of nanoscale crystallites. This microstructural change correlated with a decrease in PL intensity (**Figure 3.2c**) and points to increased grain boundary area as a limitation of this process.[69] Grain size reduction initially seems contradictory to the increase in crystallinity (**Figure 3.1b**) and the suggestion of less disorder in the steady state PL of the vapor treated film (**Figure 3.2d**).

A closer analysis of perovskite grain structure before vapor exposure with dark field TEM reveals a variety of morphological features that are persistently unapparent both in SEM and often even in bright field TEM (**Figure 3.4**).

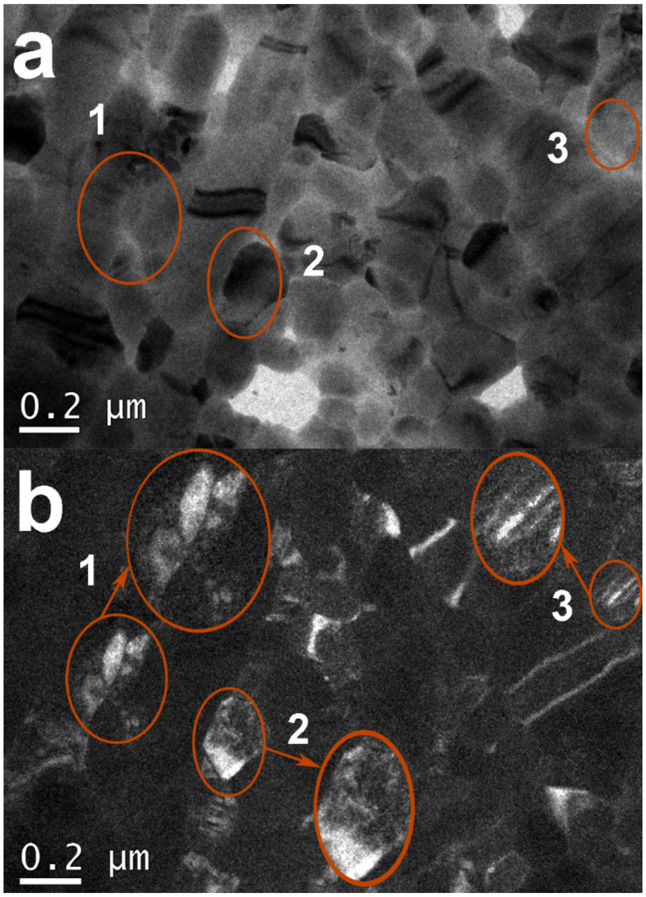

Figure 3.4. **(a)** Bright- and **(b)** dark- field TEM of a region before vapor treatment showing the microstructural complexity of $MAPbI_3$ grown by 1-step deposition. Regions that are highlighted show: (1) difficult to detect polycrystallinity, (2) highly strained and defective grains, and (3) dense and highly oriented grain boundaries. This technique cannot directly detect truly disordered domains.

Generally, we find (1) buried polycrystallinity, (2) highly strained and defective single crystals, and (3) densely packed, highly oriented grain boundaries throughout films grown from unmodified 1-step deposition. This is in addition to the predominantly disordered regions that remain undetectable and "dark" in dark field imaging. This level of microstructural complexity is unsurprising because of the existence of both $MAPbI_3 \cdot DMF$[70] and inherently disordered[43,71] phases prominent in spin-cast film growth, compounded with the transformation from cubic to tetragonal

$MAPbI_3$ in the temperature window typical annealing traverses that is known to induce grain boundary formation in similar materials through processes like twinning in previously single crystalline domains.[72] This complexity makes it challenging to define an exact grain size, as there is a continuum of disorder and a variety of grain and grain boundary sizes and aspect ratios. Ultimately, the shift from this microstructure to the nanocrystalline microstructure shown in **Figure 3.2f & h** is beneficial for device function, but this analysis reveals the important diminishing returns implicit in the application of this process. There is a short discussion of the interpretation of these dark field data.

3.2.2 *Chemical sources of reactivity toward MA^0 vapor*

To broaden the application of this process to the expanding family of hybrid organic-inorganic perovskites, factors determining lattice reactivity toward MA^0 vapor must be established. The coordination chemistry between $MAPbI_3$ and neutral molecules such as DMF,[73] DMSO,[74] and H_2O[75] has garnered a great deal of interest because of its importance in growth and degradation. Amine gases like NH_3,[66] MA^0, and larger analogues[67] demonstrate the ability to disrupt the $MAPbI_3$ lattice with differing degrees of readiness and reversibility. Van der Waals interaction, hydrogen bonding, water bridging, ion-dipole coordination, and electron transfer have all been proposed to govern host-guest interactions during the intercalation of neutral species in a solid.[76] The diverse coordination chemistry of lead halides and their hybrid analogues in both solution[77,78] and the solid state[66,67,70,75,79] makes the mechanisms that govern MA^0 vapor's interaction with the lattice somewhat difficult to pinpoint. It has been suggested that Lewis bases, specifically pyridine and thiophene, preferentially coordinate Pb dangling bonds[80] which points to the metal ion's potential reactivity. The $MAPbI_3 \cdot DMF$ crystal structure[70] suggests that DMF, also a Lewis base, preferentially hydrogen bonds with MA^+ which points to the potential reactivity of the organic sublattice. While this at first seems to simplify the matter, the halogen ion's reactivity toward the vapor cannot be neglected by virtue of the key role bonding between the halide and the organic cation plays in stabilizing the hybrid perovskite's 3D inorganic sublattice over the 2D lattice of PbI_2.[81]

To build an understanding of how these competing factors determining hybrid perovskite reactivity toward MA^0 vapor, we systematically varied each component of the lattice and examined the response to vapor exposure. First, and most importantly, exposure of PbI_2 to MA^0 vapor causes a transition to a transparent state followed by the brief formation of brown perovskite before most of the film reverts to yellow PbI_2 which is accompanied by a drastic change in microstructure (**Figure 3.5a-b**). This is unsurprising as the $PbI_2 \cdot xMA^0$ system is essentially analogous to $MAPbI_3 \cdot xMA^0$ with an iodide deficiency. The fact that MA^0 vapor does not possess the formal positive charge of methylammonium while demonstrating a similar capacity for transformation and even perovskite formation is an excellent illustration of the importance of hydrogen bonding in the formation and cohesion of $MAPbI_3$ itself. This is a simple but poignant demonstration of the core importance of the nature of the inorganic halide polyhedra in determining reactivity, and the rapid generation of the 3D perovskite analogue from the 2D PbI_2 lattice shows that interaction between MA^0 and the lead halide framework is not limited to intercalation.

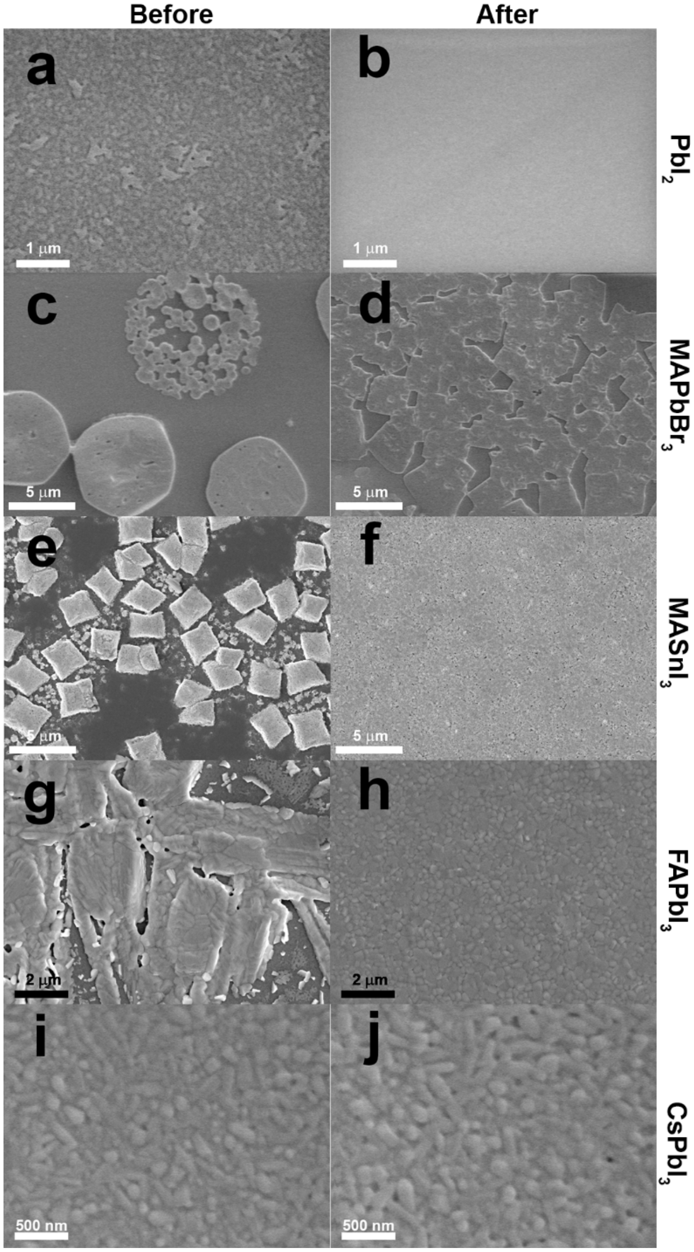

Figure 3.5. These SEM images show the effects of MA^0 vapor treatment on **(a)-(b)** PbI_2, **(c)-(d)** $MAPbBr_3$, **(e)-(f)** $MASnI_3$, **(g)-(h)** $FAPbI_3$, and **(i)-(j)** $CsPbI_3$ at scales necessary to see relevant microstructural detail.

Bonding within each hybrid perovskite lattice is unique, and thus the intrinsic reactivity of the metal halide framework toward MA^0 vapor is likely altered by changes in components of the crystal. We first addressed the influence of halogen and metal ions by fabricating $MAPbBr_3$ and

$MASnI_3$ films respectively. Upon vapor exposure, we found the same rapid, reversible transformation to the transparent intermediate state and subsequent rapid reversion to the original perovskite that is characteristic of $MAPbI_3$, and again this transformation is accompanied by dramatic microstructural changes (**Figure 3.5c-f**). As such, we more closely investigated the role of the organic cation by fabricating $FAPbI_3$ and $CsPbI_3$ films. As both the capacity to hydrogen bond and the cohesivity offered to the lattice as a whole vary as a function of the composition of the organic sublattice, we expected significant differences between each system's response to MA^0 vapor exposure. In keeping with the other systems, $FAPbI_3$ rapidly becomes transparent upon vapor exposure, but reverts back to its initial state from this transparent intermediate state much less readily, even after annealing at 100 °C for 15 min. Even though the intermediate phase is far more stable in the case of $FAPbI_3$ exposed to MA^0 vapor, there are still huge microstructural changes that occur (**Figure 3.5g-h**). Finally, we explore the more extreme case of $CsPbI_3$ in which we find no reactivity toward the vapor by virtue of no change in the film's pigment. SEM reveals no significant microstructural changes upon vapor exposure which, when combined with the behavior of $FAPbI_3$, indicates that the nature of bonding within the organic sublattice strongly mediates the reactivity toward MA^0 vapor that is initially imparted to a hybrid perovskite lattice by the nature of the inorganic polyhedra contained within. This means that Cui et al.'s assumption that the source of reactivity is the presence of lead halide polyhedra is reasonable, and the organic sublattice determines the final nature of this reactivity after a hybrid lattice has been established.

By virtue of the fact that in $MAPbI_3$ the conduction and valence band edges are composed primarily of I 5p and Pb 6s orbitals,[48] the transparency of the intermediate state in these various systems likely results from a complete loss of structure within the inorganic sublattice. This loss of pigment upon vapor exposure can point both to a solvation event[67] or a dramatic but coherent change in structure via the formation of a crystalline intermediate. Although Cui *et al.* did an excellent job of showing the accessibility of the solvated state and its prevalence under a high concentration of MA^0 vapor, they also demonstrated that although a transparent state can be established under NH_3 vapor,[66] complete solvation is not feasible. This illustrates the potential existence of multiple intermediate states within a single system, the nature of which likely playing a decisive role in determining the morphological consequences of the process.

3.2.3 *Mapping vapor induced phase transformation*

It has been demonstrated that in solution the nature of perovskite formation depends upon MA^+ concentration.[82] Specifically, low concentrations allow topotactic transformation preserving structural elements of PbI_2, while at high concentrations dissolution occurs resulting in structure determined by the precipitation event rather than the nature of the starting material. Because of the dramatic but unique responses of $MAPbI_3$ and $FAPbI_3$ to the vapor, we compared their transformations under high and low methylamine vapor pressure to more completely map MA^0 induced hybrid perovskite transformations. High vapor pressure exposure is identical to the vapor treatment process discussed above and enabled by the high volatility of MA^0 in ethanol at room temperature. Low vapor pressure exposure entails placing $MAPbI_3$ and $FAPbI_3$ films in chambers with a slow leak of MA^0 vapor for three hours. (**Figure 3.6**)

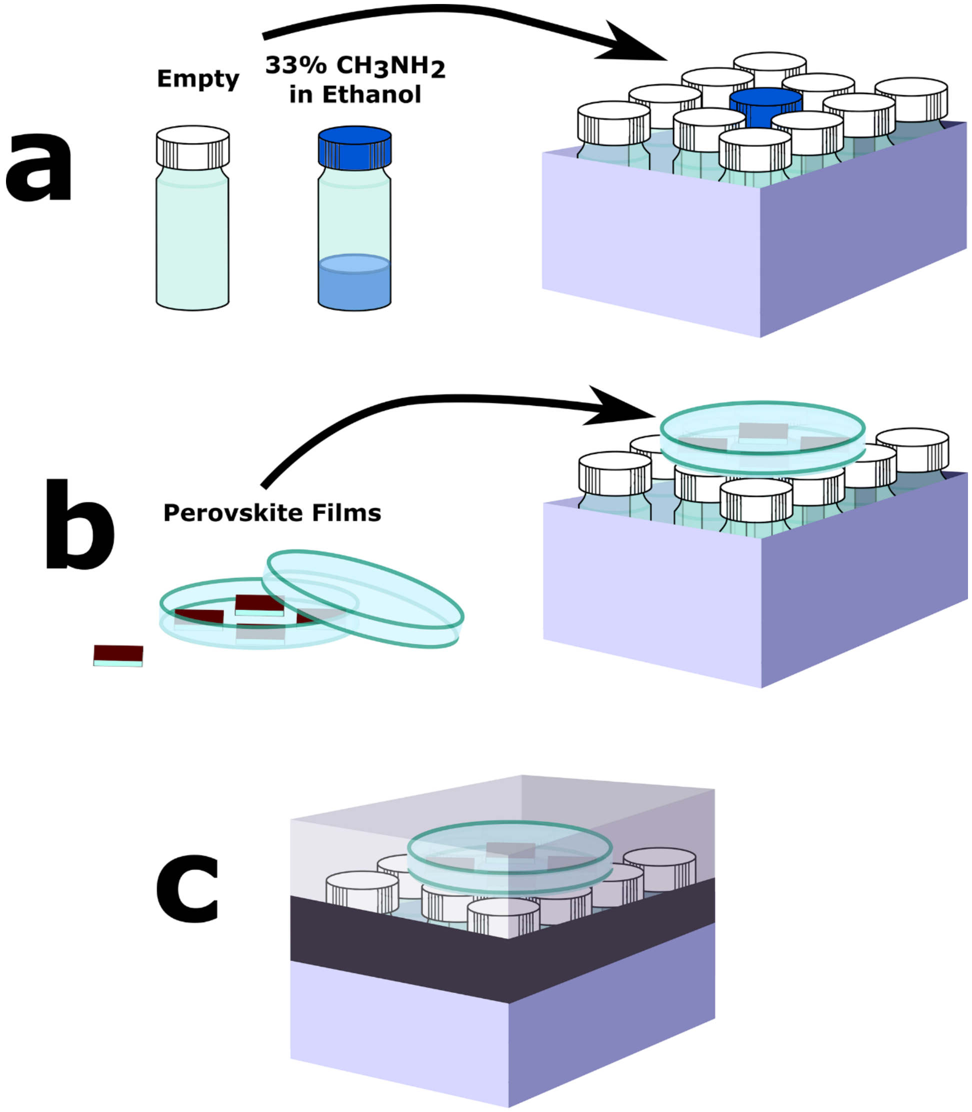

Figure 3.6. Schematic outline of the low MA^0 vapor treatment process illustrating: **(a)** inserting capped, 20 ml vials, one with methylamine solution in the center and empty vials around it for support; **(b)** placing perovskite films in a closed petri dish resting on the vials, centered on the vapor source; **(c)** sealing of the chamber.

Although direct analysis of intermediate states during vapor exposure is complicated by the incredible rapidity of transformation under high vapor pressure and the necessity of a closed system under low vapor pressure, we conducted XRD analysis of each perovskite film before vapor exposure, after exposure, and after annealing at 100 °C for 15 min. For $MAPbI_3$ exposed to a high concentration of MA^0 vapor (**Figure 3.7a**), the intermediate state is too transient to be observed after vapor removal. But based on the work of Cui *et al.* it is clear that solvation occurs under these conditions. Perovskite crystallinity dramatically increases immediately after vapor exposure and increases relatively little upon subsequent annealing. Exposure of $MAPbI_3$ to a low concentration of MA^0 vapor results in a relatively long lived, structurally coherent transparent state characterized by reflections marked as I_1 in (**Figure 3.7b**). The solitary strong reflection at low 2θ of the intermediate's primary peak (~7.2°) suggests a swelling of the lattice consistent with the perturbation of the inorganic sublattice implicated by the intermediate's transparency, but we lack sufficient detail to solve the structure. Annealing almost completely regenerates $MAPbI_3$, but with less crystallinity than in the case of high concentration MA^0 vapor exposure. For continued reference to the vapor treatments with high and low MA^0 vapor concentration, we will use the terms high $[MA^0]$ treatment and low $[MA^0]$ treatment.

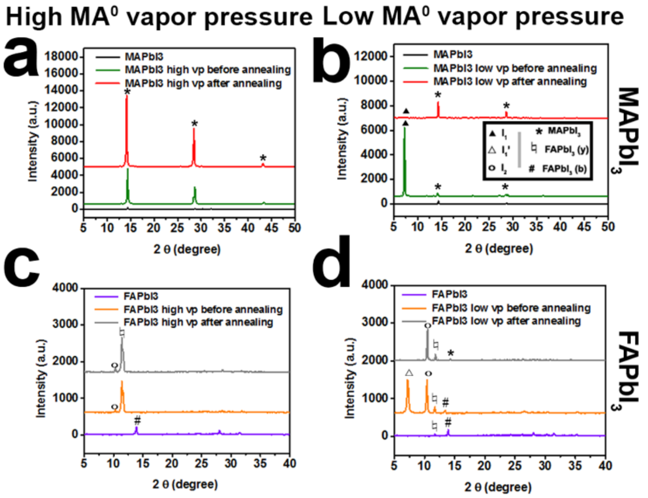

Figure 3.7. Phase evolution through XRD analysis of $MAPbI_3$ under **(a)** high $[MA^0]$ and **(b)** low $[MA^0]$ treatments, as well as $FAPbI_3$ under **(c)** high $[MA^0]$ and (d) low $[MA^0]$ treatments. Although detail is limited, the phases indicated are listed in the legend located in the center right of the figure. $FAPbI_3$ (y) and $FAPbI_3$ (b) indicate the yellow and black $FAPbI_3$ polymorphs respectively.

Intermediate states formed by $FAPbI_3$ are distinct between high and low [MA^0] treatments, and one is long lived even after annealing. Because of the well-known instability of the black polymorph at room temperature.[83] the $FAPbI_3$ film contains both yellow and black polymorphs before vapor exposure. Upon high [MA^0] treatment (**Figure 3.7c**), the black polymorph disappears and is replaced by the yellow polymorph and an intermediate phase distinct from I_1 with a primary peak at ~11° 2θ which we have marked as I_2. Annealing causes little change in this phase distribution. Low [MA^0] treatment (**Figure 3.7d**), leads primarily to a greater fraction of stable I_2 and an phase bearing the same solitary strong peak at ~7.2° 2θ as I_1. This intermediate was labeled as I_1'.

As a function of time (**Figure 3.8**), low [MA^0] treatment of $FAPbI_3$ initially causes I_2 formation followed by I_1' formation over time. This indicates that while I_2 forms more rapidly under MA^0 vapor, the state analogous to $MAPbI_3$'s preferred state under low concentration MA^0 is the same eventual fate of $FAPbI_3$. Annealing primarily causes elimination of I_1' and the generation of only a small amount of $MAPbI_3$ while the fractions of the yellow $FAPbI_3$ polymorph and I_2 remain relatively unchanged. This suggests that while the primary product of I_1' is $MAPbI_3$, the readiness with which the transformation proceeds is significantly reduced compared to I_1, which is part of the reason we draw a distinction between them. Although detail in **Figure 3.7** is limited, the structural similarities between I_1 and I_1' suggest that atomic spacing may primarily be determined by the neutral MA^0 molecule's interaction with the lattice. $MAPbI_3$ formation within $FAPbI_3$ is a demonstration of the proton transfer between cations in the lattice and MA^0. The stark kinetic differences in the transformation of each intermediate discussed above shows that bonding within the hybrid perovskite organic sublattice plays a significant role in determining the readiness with which vapor induced intermediate states regenerate the desired perovskite, and in the extreme case of $CsPbI_3$ prevents reaction entirely.

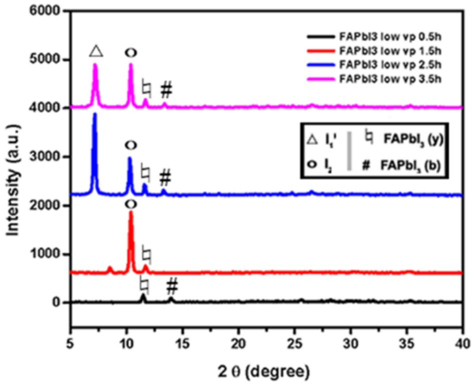

Figure 3.8. XRD showing the phase evolution of $FAPbI_3$ during low $[MA^0]$ treatment as a function of time. Phases indicated are listed in the inset legend with $FAPbI_3$ (y) and $FAPbI_3$ (b) indicating the yellow and black polymorphs respectively.

While the phase evolution presented in **Figure 3.7** illustrates the role of vapor concentration and organic sublattice composition in mediating available transformations, we cannot directly discern whether these intermediate phases persist exclusively during exposure or they are the result of equilibration after vapor removal. That said, through the microstructural consequences of each transformation just discussed, we can gain increased mechanistic insight as well as improved intuition in the rational design of vapor-based post deposition treatments. To this end we correlated SEM and detailed TEM analysis (**Figure 3.8 and 3.9**) of regions in each system before vapor exposure, after vapor exposure, and after subsequent annealing. Because films for SEM analysis are fabricated under conditions identical to device fabrication, we can directly see the macroscopic consequences of the vapor treatments in a device context. As TEM samples are fabricated via an identical method with the only exception of a diluted perovskite precursor solution, we have analogous growth conditions with reduced coverage and film density enabling us to more easily define microscopic differences in material diffusion and grain reconstruction inherent to each process.

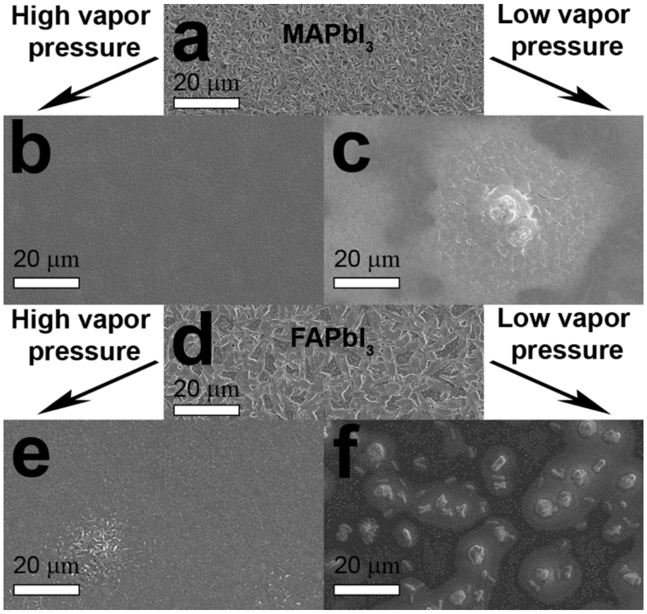

Figure 3.9. SEM of **(a-c)** $MAPbI_3$ and **(d-f)** $FAPbI_3$ before and after MA^0 vapor exposure for both high and low [MA] treatments.

SEM characterization of each transformation shows a great degree of diffusion in all cases. Both high [MA^0] cases (**Figure 3.8 a-b, d-e**) result in excellent film coverage. Both low [MA^0] cases (**Figure 3.8 a & c, d & f**) result in coarsening which generated thick and barren regions. Even though plentiful pin-holes are in the initial films (**Figure 3.8 a & d**), the density of material is great enough so that a reasonably large amount of material surrounds any given point in the film. This is not the case in the TEM samples in which coverage was sparse enough to isolate individual features and observe their microscopic transformation upon vapor exposure, a key distinguishing feature between the data sets in **Figures 3.9 and 3.10**. Each pane of **Figure 3.10** correlates bright field TEM images (top), select area electron diffraction (SAED) patterns (inset), and one representative dark filed image (bottom) of a region before and after vapor treatment. For $MAPbI_3$ high [MA^0] exposure, the phase purity confirmed by SAED (**Figure 3.10a,** inset) and the dramatic reduction in grain size apparent in the dark field images (**Figure 3.10a**, bottom) were already discussed in detail at the beginning of the manuscript. The bright field images (**Figure 3.10a**, top) show a great deal of diffusion unconstrained by the initial physical bounds of the material consistent with the liquid intermediate discussed by Cui *et al.* In contrast, diffusion in $MAPbI_3$ during low [MA^0] exposure (**Figure 3.10b**, top) remained constrained to the physical extent of the material before vapor exposure. Although coarsening still drives large scale diffusion which thickens some regions and depletes others, we can more clearly see the way diffusion is facilitated by the preexisting solid framework, an issue distinguishing low [MA^0] treatment from the high [MA^0] case. The dark field images (**Figure 3.10b**, bottom) show that although grain size is still reduced compared to the initial state, final average grain size is slightly larger than in the high [MA^0] treatment. This is likely due both to grain growth within the solid intermediate and the reduction of perovskite nucleation rate caused by the more gradual change in MA vapor pressure upon process completion inherent to the low [MA^0] treatment.

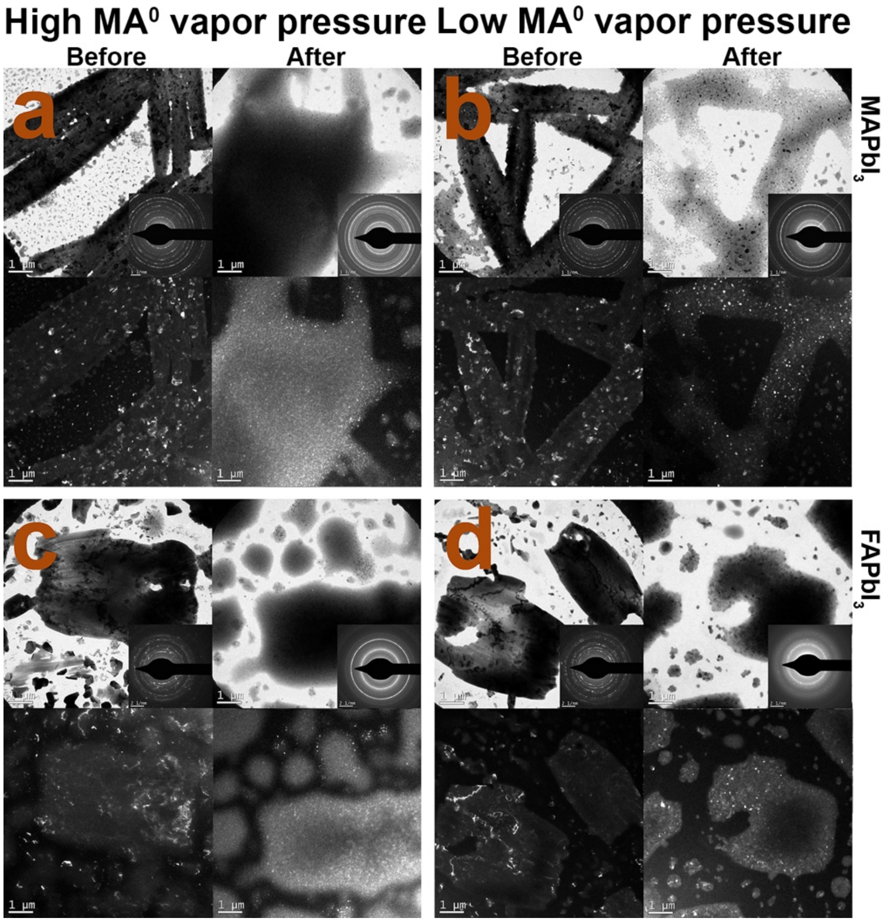

Figure 3.10. Each pane compared an identical region before and after MA^0 vapor exposure with bright field imaging (top), select area electron diffraction (inset), and dark field imaging (bottom) with transmission electron microscopy of **(a-b)** $MAPbI_3$ and **(c-d)** $FAPbI_3$ at both (a & c) high and (b & d) low $[MA^0]$ treatments.

Even though transformation back from the intermediate state is incomplete in high $[MA^0]$ treated $FAPbI_3$, grain size revealed by dark field imaging (**Figure 3.10c**) is quite comparable to that of high $[MA^0]$ treated $MAPbI_3$ indicating that dramatic disruption to the original perovskite grain structure occurs upon initial intermediate formation, an issue related to the swelling of the lattice. That said, diffusion is once again constrained by material distribution before exposure, implicating the prevalence of a solid intermediate and suggesting that pervasive lattice disruption occurs regardless of solvation.

Low [MA^0] treatment of $FAPbI_3$ leads to diffusion that is again facilitated by the solid framework existing before exposure (**Figure 3.10d**). Coarsening facilitated by large scale diffusion similar to $MAPbI_3$ under low [MA^0] vapor can be observed. Also, in keeping with $MAPbI_3$, average grain size is smaller than it was initially but larger than the high [MA^0] analogue. Coupled with the distinctly different phase content of each system (**Figure 3.8**), this points to MA^0 vapor pressure as a function of time as a dominant determinant of final grain size even though the nature of accessible phases and their transformations are largely determined by the composition of the organic sublattice. This slight increase in grain size comes at the cost of coverage and overall perovskite crystallinity in the low [MA^0] treatment of both systems. The dramatic changes in morphology evident in **Figure 3.9** show that regardless of intermediate state, MA^0 vapor facilitates massively enhanced diffusion. The subtler distinctions apparent in **Figure 3.10** suggest that $MAPbI_3$ can readily reach an essentially solvated state under high MA^0 vapor pressure, but both reducing the vapor pressure and altering composition of the organic sublattice (i.e. $FAPbI_3$ and $CsPbI_3$) impedes the formation of this truly solvated state. Combining this with the sharp kinetic distinction between the intermediates and the complete transformation back to perovskite from this solvated state versus the slow and incomplete transformation after structurally coherent intermediate stabilization under low [MA^0] vapor, it becomes apparent that circumventing the formation of metastable states during vapor based post deposition treatment may be an important component of gaining the full value the process offers in increased film quality. The solvation event thus has the dual purpose of facilitating diffusion and kinetically excluding metastable, crystalline intermediates that frustrate transformation.

3.3 CONCLUSION

From our physical and chemical analysis of hybrid perovskite MA^0 vapor post deposition treatment, we offer the design rules summarized in **Figure 3.11** for the broad application of this process in contexts involving different materials and scales. In general, obliteration of original perovskite grain structure occurs regardless of solvation. The cost of massively improved film coverage is greatly reduced grain size regardless of the nature of the intermediate formed during vapor exposure and promoting grain growth is a challenge because of a dependence on vapor removal and coarsening processes. Our PL results show the utility this process offers in establishing a perovskite interface with more intimate contact for charge extraction, as well as the diminishing returns inherent in the process. Taken together, this work demonstrates the successful implementation of this process in PHJ architecture. Using the mechanistic insight generated here, it is clear that these microstructural trends and physical insights have very little dependence upon initial perovskite growth route and thus starting morphology. While it is clear that a variety of amine vapors can induce massive material changes, choice of vapor determines both accessible phases and how the system can move through them.

The methodology of this facile and high throughput post deposition treatment is potentially useful for translation to industry, and sensitivity to the issues summarized in **Figure 3.11** may minimize the detriments and maximize the benefits it entails. Ultimately, this comes down to controlling the microstructural consequences of the process and ensuring phase purity upon completion. These issues quickly become complex when large scale systems with implicit inhomogeneities and non-ideal time scales are implemented, especially with materials with more complex phase behavior like $FAPbI_3$. We hope to extend the understanding here to such processes.

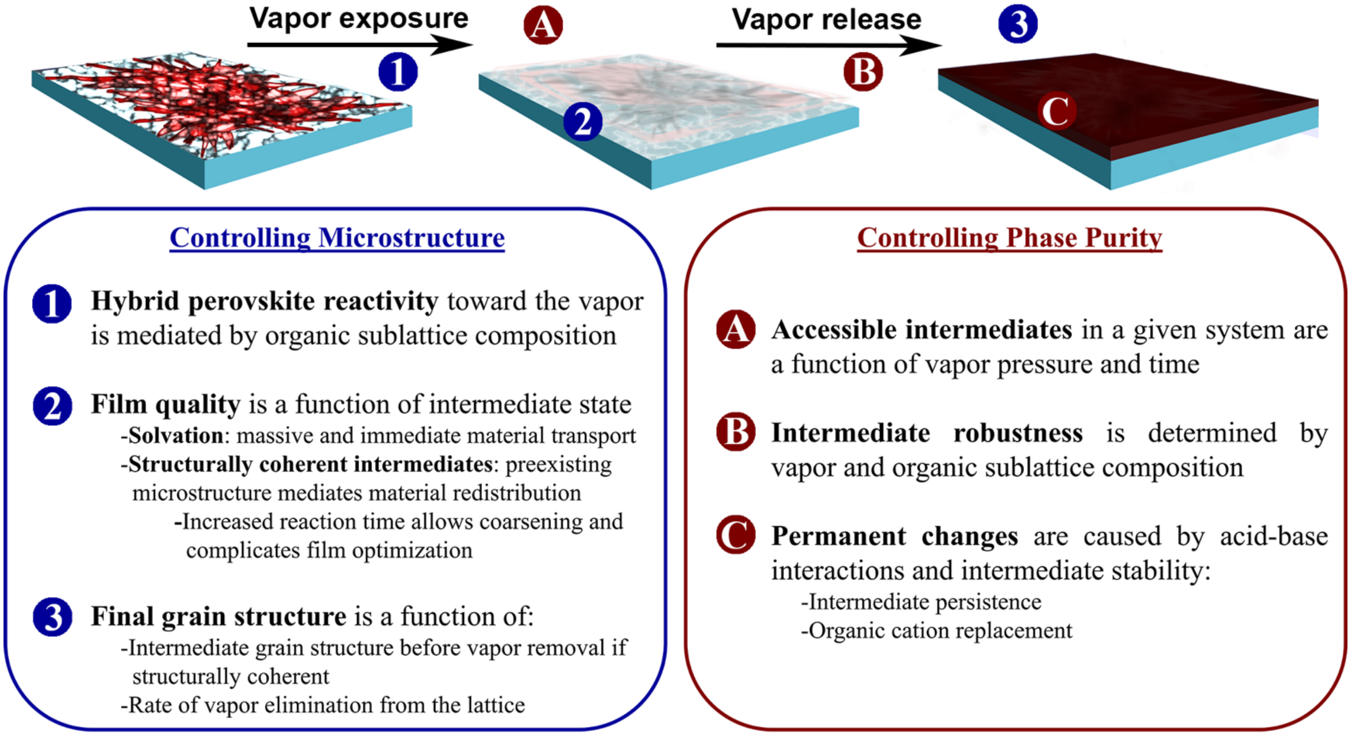

Controlling Microstructure

① **Hybrid perovskite reactivity** toward the vapor is mediated by organic sublattice composition

② **Film quality** is a function of intermediate state
- **Solvation**: massive and immediate material transport
- **Structurally coherent intermediates**: preexisting microstructure mediates material redistribution
  - Increased reaction time allows coarsening and complicates film optimization

③ **Final grain structure** is a function of:
- Intermediate grain structure before vapor removal if structurally coherent
- Rate of vapor elimination from the lattice

Controlling Phase Purity

Ⓐ **Accessible intermediates** in a given system are a function of vapor pressure and time

Ⓑ **Intermediate robustness** is determined by vapor and organic sublattice composition

Ⓒ **Permanent changes** are caused by acid-base interactions and intermediate stability:
- Intermediate persistence
- Organic cation replacement

Figure 3.11. Design rules for MA^0 vapor-based post deposition treatments for OIHPs in general.

Chapter 4. DEFECT PASSIVATION OF ORGANIC-INORGANIC HYBRID PEROVSKITES BY DIAMMONIUM IODIDE TOWARDS HIGH-PERFORMANCE PHOTOVOLTAIC DEVICES

This chapter presents a simple defect passivation method by post-treating $MAPbI_3$ film with a rationally selected diammonium iodide. The following material is reproduced from the article titled *Defect Passivation of Organic-Inorganic Hybrid Perovskites by Diammonium Iodide towards High-Performance Photovoltaic Devices*[84] and the supporting information of this publication has been integrated into the main text.

4.1 INTRODUCTION

The polycrystalline feature of solution-processed perovskite film and its ionic nature inevitably incur substantial crystallographic defects, especially at the film surface and GBs. Recently, several approaches have been reported to be able to passivate the surface/interfaces and GBs of solution-processed OIHP films. For example, PbI_2 preferably formed at GBs through high temperature annealing creates a type I band alignment at GBs, resulting in defect passivation and retardation of carrier recombination.[85–87] Meanwhile, small molecules have also been employed to passivate dangling bonds in OIHPs by exploiting the associated intermolecular interaction.[88–90] Lately, we and several groups have discovered that the commonly used fullerene-based electron-transporting layers (ETLs) can also passivate surface trap states and GB defects in OIHPs to eliminate trap states and suppress device hysteresis.[91–93]

However, the role of fullerene in eliminating the dominant vacancy defects is limited. We and several groups have found that iodide in perovskites has the propensity to dope fullerene at the perovskite/fullerene interface.[91,94,95] In this case, iodo radicals would be inevitably generated after doping and then form iodine that can potentially sublime easily. As a result, new V_I defects can possibly be generated inside the perovskite film. Thus, for fullerene-based inverted PSCs, it would be ideal if the perovskite surface and GBs can be passivated without generating new defects due to perovskite fullerene interaction.

In this study, a series of diammonium iodides namely $NH_3I(CH_2)_4NH_3I$ (C4), $NH_3I(CH_2)_8NH_3I$ (C8), and $NH_3I(CH_2)_2O(CH_2)_2O(CH_2)_2NH_3I$ (EDBE) were explored to passivate perovskite surface and GBs considering their bilateral ammonium iodide end can simultaneously passivate perovskite layer and dope adjacent electron-transporting layer (PCBM herein) in derived PSCs, as illustrated in **Figure 4.1**. In pursuing the suitable materials for defect passivation, we surprisingly discovered that the molecular structure of diammonium iodide plays a critical role in affecting perovskite's surface morphology and phase purity. We found that both C4 and EDBE can induce 3D to 2D perovskite phase transformation during post treatment. However, the activation energy for such transition can be modulated by tailoring the molecular structure of the diammonium iodides. The C8 can successfully passivate perovskite surface and GBs without causing 2D phase transformation of $MAPbI_3$ due to its unique anti-gauche isomerization, which may elevate the activation energy for the 3D to 2D phase transformation. Consequently, the thin-film PSC passivated by C8 shows a much-improved PCE of 17.60% compared to 14.64% for the control device.

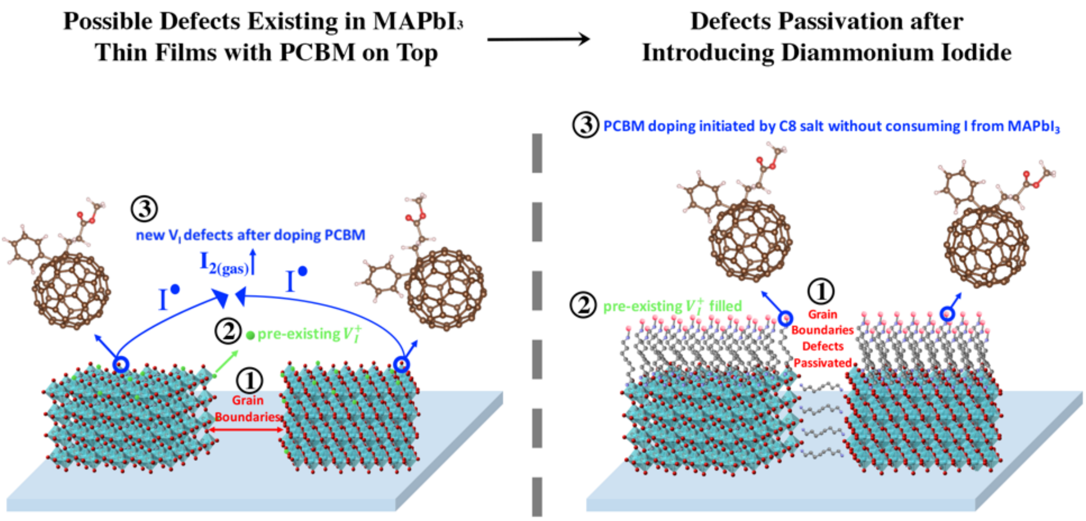

Figure 4.1. Summary scheme for left: the possible defects existing in MAPbI$_3$ thin films with PCBM on top as electron transport layer and right: defects passivation mechanism after introducing diammounium iodide through post treatment.

4.2 RESULTS AND DISCUSSION

4.2.1 *Diammonium iodides for Perovskite Passivation*

In order to effectively passivate above-mentioned defects, three diammounium iodides with different molecular structures, C4, C8, and EDBE (**Figure 4.2a**), were selected since their bilateral ammonium iodide group is capable of simultaneously passivating perovskite surface/GBs and inducing PCBM doping without consuming iodides from bulk perovskite (**Figure 4.1**). We first try to investigate the effect of alkyl chain length on electron transfer from perovskite to PCBM by comparing C4 and C8. The EDBE is included in our exploration to study whether the hydrogen bonding between adjacent EDBE molecules[96] will influence the self-assembly kinetics between the organic species and perovskite for better passivation effects.

The post-treatment procedure is illustrated in **Figure 4.2a** and detailed in Chapter 2. It is important to note that similar surface topology and bulk properties such as crystallinity and absorption coefficient of perovskite films should be retained if the diammonium iodide only distributes at perovskite surface or in the GBs. To examine this, the evolution of surface morphology of post-treated perovskite films is investigated by SEM (**Figure 4.2b**). As clearly shown, only the C8-treated film showed similar surface morphology to the pristine film, which encompasses a compact and uniform film with grain sizes ranging from tens of nanometers to 200 nm. Whereas, the C4- and EDBE-treated films showed distinct morphology with strip-like and branch-like features, respectively.

The enormous change in surface morphology of C4- and EDBE-treated films prompt us to speculate the possibility of 3D to 2D perovskite phase transformation due to the tendency of large-sized diammonium iodides to form 2D hybrid perovskites,[96,97] which induce the morphological changes through dissolution-recrystallization.[82] To probe this, XRD and UV-vis absorption of post-treated films were measured to study if the relatively larger organic cations diffuse into the pristine perovskite film and partially convert the perovskite from 3D to 2D.

As clearly evidenced from the XRD data shown in **Figure 4.2c**, the characteristic diffraction corresponding to {200} planes of $(C4)PbI_4$ and (020) plane of $(EDBE)PbI_4$ are apparent in the C4- and EDBE-treated films, respectively. In addition, their corresponding UV-vis absorption spectra (**Figure 4.2d)** clearly show the excitonic absorption peak, affirming the formation of 2D perovskite due to the intercalation of C4 and EDBE cations into the perovskite films. However, the C8-treated film seems to uniquely preserve its morphology and phase purity without going through such transition (**Figure 4.2b-d**).

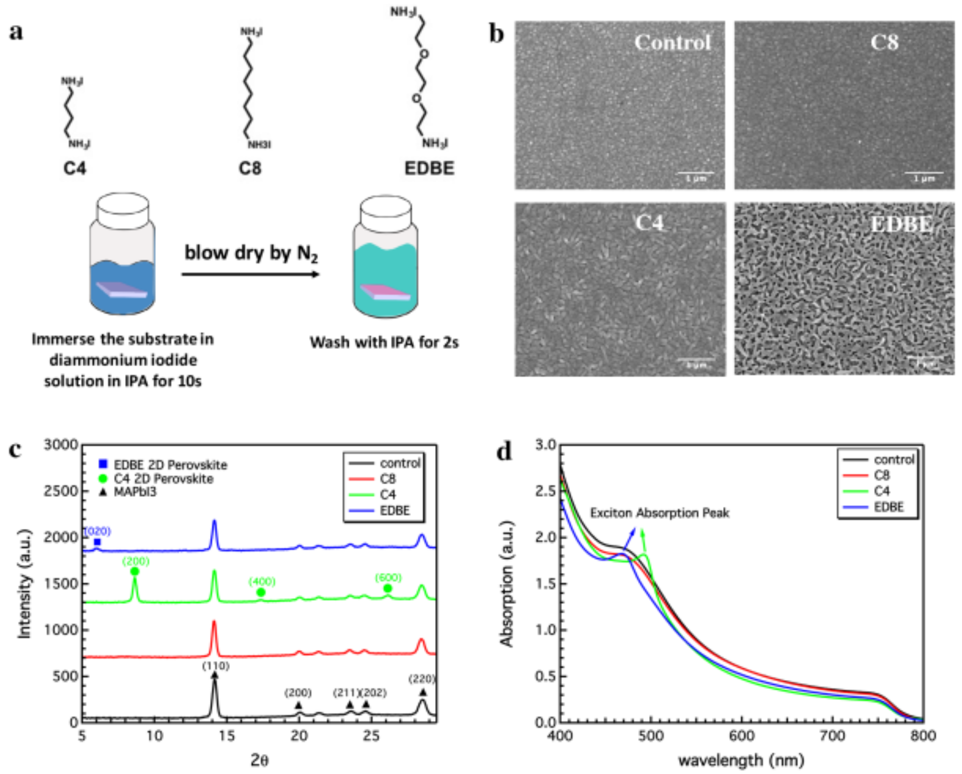

Figure 4.2. (a) Three kinds of diammonium iodide salts (abbreviated to C4, C8 and EDBE) selected for perovskite passivation and the processing details. **(b)** SEM images, **(c)** XRD, and **(d)** UV-absorption of control film ($MAPbI_3$), C8-, C4-, and EDBE-treated films.

The 3D to 2D perovskite phase transformation induced by C4 and EDBE cations can be explained by the tendency of forming more thermodynamically stable 2D hybrid perovskite.[98–101] The reaction rate for such 3D to 2D phase transformation is in principal determined by its associated activation energy. Therefore, the inhibited phase transformation observed in C8-treated films might be due to two possible reasons: i) the phase transformation from 3D $MAPbI_3$ to 2D $(C8)PbI_4$ occurs too slow to be effectively observed during the fast 10 s treatment period; ii) the $(C8)PbI_4$ in nature has a higher Gibbs free energy than $MAPbI_3$.

The distinction in morphological variation between C4/EDBE- and C8-treated films further triggered us to ponder about the structural difference of their corresponding 2D perovskites.

Interestingly, Lemmerer *et al.*[97] have found that, among all of their studied 2D lead-halide based perovskites incorporating diammonium cations, C8 is the only material that has gauche conformation in the middle of the alkyl chain while other diammomium cations consist of only anti conformation. This gauche conformation has higher energy compared to the anti conformation and the associated local energy minimum is metastable. Thus, it can be inferred that the middle part of C8 diammonium cation needs to convert from its energetically stable anti form into the gauche conformation in order to intercalate into the 2D perovskite film. Such anti-gauche isomerization necessitates additional energy barrier for 3D to 2D phase transformation, thereby slowing down the conversion.

To prove this hypothesis, the 2D hybrid perovskite (n=1) thin films based on C4, C8, and EDBE were prepared accordingly by a simple spin-coating procedure. The 2D hybrid perovskite precursor solution was made by dissolving an equimolar ratio of PbI_2 (0.3 M) and ammonium iodide (0.3 M) in DMF at 60°C and spin-coated at 3000 rpm for 60 s. The resulting thin films were annealed at 100°C for 10 min. As shown in **Figure 4.3a**, both spin-coated C4 and EDBE films convert immediately into yellow color after placing onto the pre-heated (100 °C) hotplate, whereas the C8 film remains clear after being annealed at 100 °C for 10 min. As previously reported by Lemmerer[97], the single crystal of $(C8)PbI_4$ possesses a yellow color as well, which is typical for lead-iodide based 2D hybrid perovskites. Therefore, we can conclude that the elevated activation energy for forming the corresponding 2D $(C8)PbI_4$ perovskite phase is the reason for forming the clear intermediate state (**Figure 4.3c** and will be discussed later). Interestingly, it was discovered that exposing the C8 films in air facilitates the 2D phase transformation. As shown in **Figure 4.3b**, the C8 film turns into yellow color after being stored in air overnight.

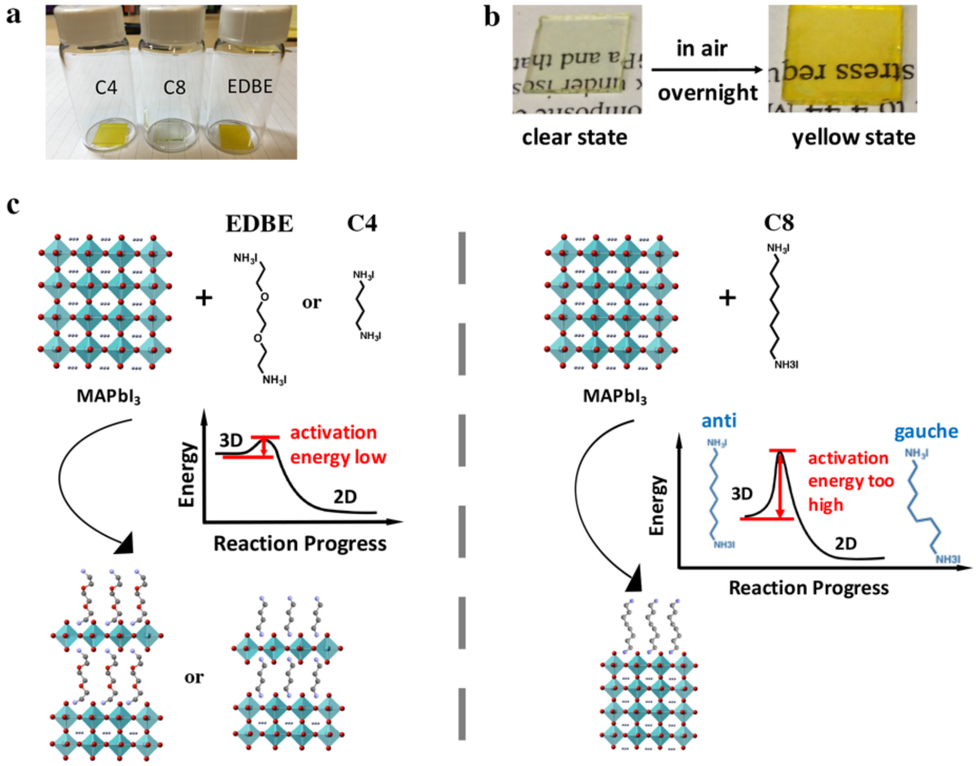

Figure 4.3. (a) Photos of C4-, C8-, and EDBE-PbI$_4$ thin films after the spin-coating and annealing process. **(b)** Photo of C8-PbI$_4$ thin film transferring from clear state to yellow state after being put in air for overnight. **(c)** Schematic demonstration of why EDBE and C4 treatment can induce respective 2D hybrid perovskite formation, while C8 only stays at the surface or grain boundaries without affecting bulk properties.

The corresponding XRD and UV-vis absorption of clear and yellow (C8)PbI$_4$ thin films are presented in **Figure 4.4**, where the yellow phase is clearly identified to be the 2D (C8)PbI$_4$. However, the C8 film remains in the clear state even after being stored in N$_2$ for a week. This result suggests that moisture or/and oxygen play a critical role in lowering the activation energy for this phase transformation and the exact mechanism is still under investigation.

Since the 2D (C8)PbI$_4$ film can be eventually formed (**Figure 4.3b**) and is quite stable in air, we hypothesize that although anti-gauche isomerization may also raise the 2D (C8)PbI$_4$ phase's Gibbs free energy, it is still lower than that of 3D MAPbI$_3$ phase. Hence, the change in Gibbs free energy should play a less important role than the elevation of activation energy in mediating 3D to 2D perovskite phase transformation in C8 post treatment. A scheme demonstrating the reaction mechanism of the studied diammonium salts is illustrated in **Figure 4.3c**. Our results thus manifest that owing to the higher thermodynamic stability of 2D perovskites relative to the 3D counterparts, most organic salts with relatively larger cations introduced for perovskite passivation will induce fast 3D to 2D phase transformation (within 10 s) due to the low activation energy of this process. However, the anti-gauche isomerization for realizing 3D to 2D phase transformation required for C8 slows down the process and thus limits itself to be only distributed at perovskite surface and GBs.

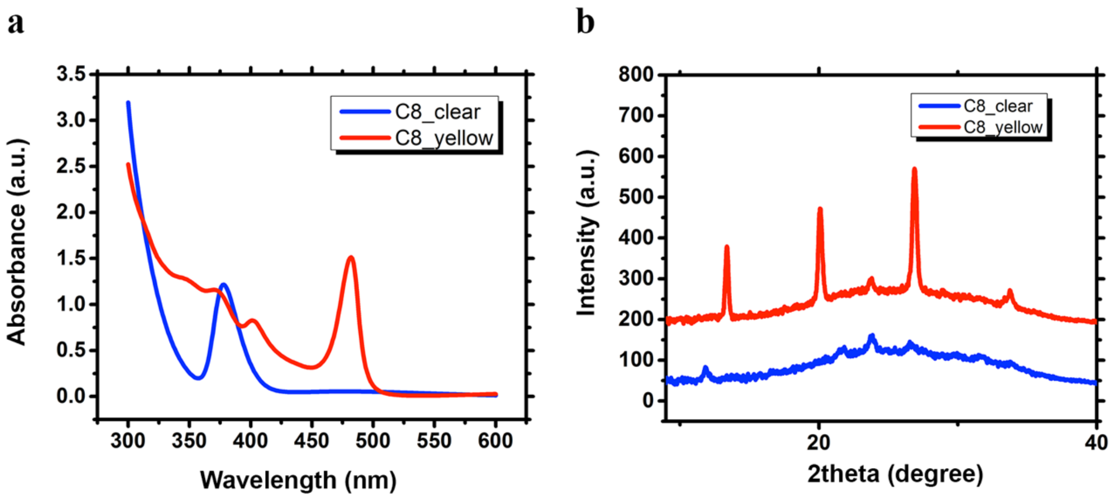

Figure 4.4. (a) UV and **(b)** XRD characterization for clear and yellow (C8)PbI_4 thin films. The clear film is obtained right after the annealing process and the yellow film here is obtained by exposing the same clear film to air under dark for overnight.

4.2.2 *Defect Passivation Characterization*

After elucidating that only C8 can successfully interact with pristine perovskite without affecting its bulk properties, we next examined its efficacy in defect passivation. Scanning kelvin probe microscopy (SKPM)[102,103] is employed to investigate the perovskite films before and after C8 treatment. **Figure 4.5A** illustrates the topography (left column) and surface potential (SP) (right column) images of the perovskite films before (top row) and after (bottom row) treatment. The root-mean-square (RMS) roughness of perovskite films before and after treatment are 7.99 nm and 5.99 nm, respectively. As can be clearly seen, both films showed similar morphology, affirming no surface reconstruction of perovskite film after C8 treatment which is consistent with the SEM image shown in **Figure 4.2b**. Notably, the small decrease in surface roughness of the treated film indicates that C8 did fill in the GBs and thus reduces the height difference between grain surface and GB.

Despite the similarity in surface morphology, two films showed distinctly different SP. For the control film without treatment, most GBs showed higher SP than that of the interior grains, indicating a downward band-bending in the GBs which will cause electron trapping.[69,85] However, the SP difference between GBs and interior grains is significantly reduced after treatment, indicating negligible band bending at this corresponding interface. This will facilitate electron transport across the GBs. It clearly validates effective perovskite passivation. In addition, the average SP of the treated film (-0.10 V) shows an increase of 0.24 V compared to that of pristine film (-0.34 V). This suggests a larger downward surface band-bending of the treated film, which can benefit charge carrier separation and facilitate the electron collection toward ETL in derived devices.[104]

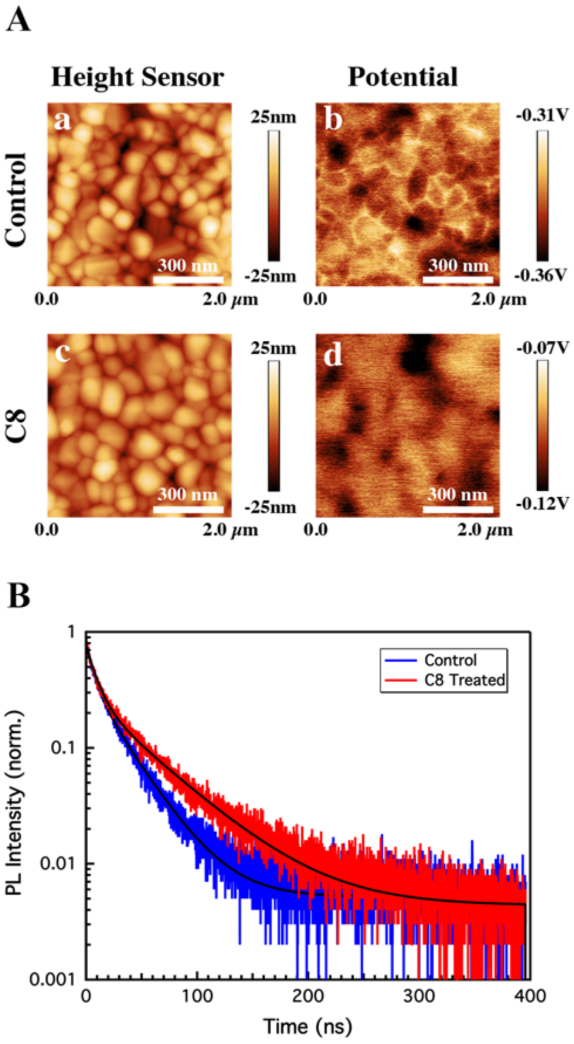

Figure 4.5. **(A)** 2D topology **(a, c)** and surface potential maps **(b, d)** for control and C8-treated perovskite films. **(B)** PL decay for control and C8-treated films on glass.

TRPL has also been utilized to further examine the effects of defect passivation on resulting photo-physical properties, as shown in **Figure 4.5B**. The average lifetime of perovskite film increased from 24 ns to 40 ns after C8-treatment with both improved fast and slow component, revealing the suppressed charge recombination in the treated film. The fitting and detailed parameters are summarized in **Table 4.2**.

Table 4.2. Fitted lifetime results of control and C8 treated films, where t1 and t2 refer to fast and slow decay lifetime respectively, and $t_{average}$ is intensity weighted.

	t1 (ns)	t2 (ns)	$t_{average}$ (ns)
Control	7	29	24
C8 treated	9	50	40

4.2.3 *Photovoltaic Performance Characterization and Recombination Kinetics Study*

To examine how C8-passivation affects the photovoltaic properties, PHJ devices were fabricated in the configuration shown in **Figure 4.6a**. The detailed fabrication procedure is described in chapter 2 and the statistical device performance with standard deviation for control, C8-, C4-, and EDBE treated devices are shown in **Table 4.3**. As expected, the PCE of the derived PSC is significantly improved from 14.64% to 17.60% after C8-treatment (**Figure 4.6b**) with a marked increase in all photovoltaic parameters (**Table 4.3**). Different to the C8-treated device, the C4- and EDBE-treated PVSCs showed inferior PCEs with a much lower short-circuit current (J_{SC}) and fill factor (FF). This can be attributed to the formation of bulk 2D perovskite, in which the intercalated insulating alkyl chains block electron transfer from perovskite to PCBM and thus impede efficient charge collection.

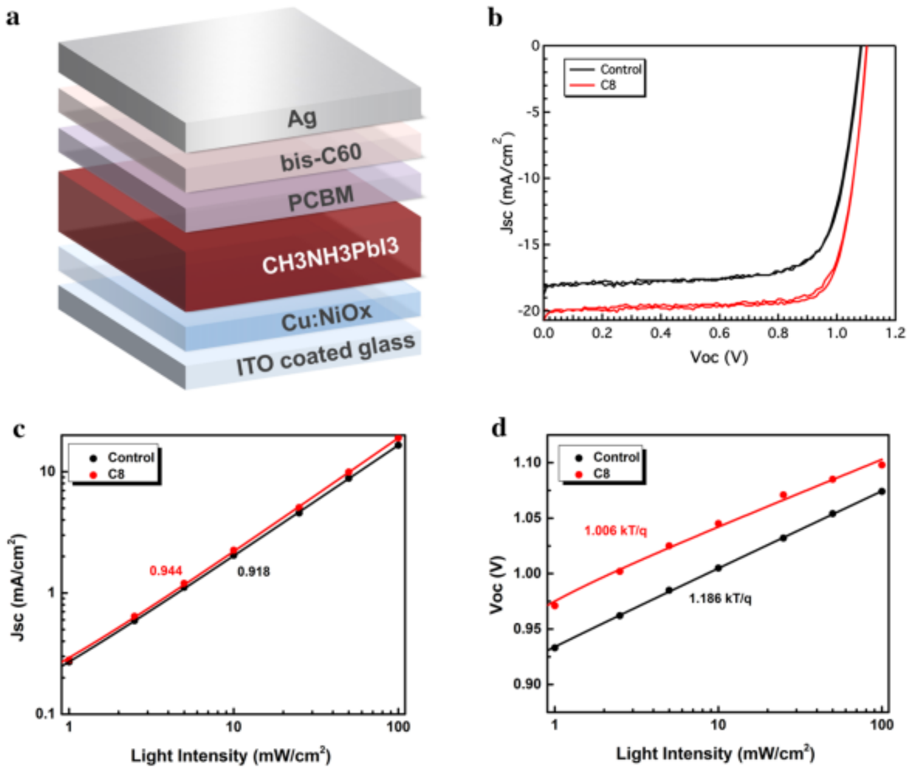

Figure 4.6. (a) The device architecture used in this study. **(b)** The *J-V* characteristics of control and C8-treated devices. The dependence of **(c)** J_{SC} and **(d)** V_{OC} on light intensity.

Table 4.3. Photovoltaic performance values of the control and treated devices. The results include average values with deviation calculated from 8 representative devices.

	Voc (V)	Jsc (mA/cm^2)	FF	PCE (%)
Control	1.09±0.01	17.89±0.40	0.75±0.02	14.70±0.22
C8 treated	1.11±0.01	19.37±0.55	0.79±0.01	17.02±0.33
C4 treated	1.10±0.01	12.10±2.38	0.72±0.04	9.75±2.22
EDBE treated	1.12±0.004	3.69±0.64	0.69±0.02	2.84±0.60

To better understand the charge carrier dynamics and enhanced performance, we have studied the device recombination kinetics by measuring the dependence of *J–V* characteristics on light intensity.[105] **Figure 4.6c** shows the dependence of J_{SC} on light intensity of the studied devices, in which the fitted slope (in accordance to power law) is 0.918 and 0.944 for the control device and

C8-treated device, respectively. This result clearly indicates that the reduced charge recombination loss for the C8-treated device is due to effective defect passivation. **Figure 4.6d** shows the relationship between open-circuit voltage (V_{OC}) and light intensity of the studied devices. Notably, the control device possesses a slope of 1.186 kT/q throughout the entire range of light intensity, showing a bimolecular recombination dominant kinetics. This supports the respectable high PCE of the control device. Neverthelessly, the C8-treated PVSC showed a further reduced slope of 1.006 kT/q, suggesting a minimized trap-assisted recombination in device. In addition to the effective defect passivation, this significantly reduced recombination loss can also be attributed to the interfacial doping at the C8/PCBM interface.[91,92,106] The other end of C8 ammonium iodide can dope PCBM without the need of creating further V_I defects inside the perovskite film, leading to a much improved device performance.

4.3 CONCLUSION

In summary, we have successfully developed a simple and effective method to passivate the surface and GB defects of $MAPbI_3$ films by employing alkyl diammonium iodide. It was discovered that the molecular structure of used diammonium salt has a profound effect on influencing the surface morphology and phase purity of perovskite. Both C4- and EDBE-diammonium salts induce 3D to 2D hybrid perovskite phase transformation during treatment, which is unfavorable for charge transport and device performance due to their insulating nature. However, the 3D to 2D transition is inhibited in C8-treated film due to its unique anti-gauche isomerization, which elevates the activation energy of this transition. Therefore, the C8 diammonium iodide treatment can successfully passivate perovskite films as evidenced by the SKPM and PL measurements. Further investigations on device recombination kinetics also showed reduced charge recombination loss in the derived device, indicating that the C8 salt can also potentially dope PCBM. As a result, the C8-treated PSC show a much-improved PCE of 17.60% compared to that of the control device with a PCE of 14.64%. This study highlights the importance of rational molecular design for perovskite surface modification and passivation.

Chapter 5. REALIZATION OF HIGHLY ORIENTED MAPBBR$_3$ PEROVSKITE THIN FILM VIA ION EXCHANGE FOR ULTRAHIGH COLOR PURITY GREEN LIGHT EMISSION

This chapter presents growth of highly oriented MAPbBr$_3$ films through ion exchange from 2D to 3D perovskite. The following material is reproduced from the article titled *Realization of Highly Oriented MAPbBr$_3$ Perovskite Thin Film via Ion Exchange for Ultrahigh Color Purity Green Light Emission*[107] and the supporting information of this publication has been integrated into the main text.

5.1 INTRODUCTION

Organic-inorganic hybrid perovskites are promising materials for optoelectronic applications. The morphology of perovskite thin films is a key determinant for the performance of functional devices. During the advancement of perovskite photovoltaics, various processing techniques[108] have been developed to control the morphology of iodide-based perovskites. Morphological control is even more crucial for bromide-based perovskites (attractive for green-light emission) because of their tendency to form large isolated crystals.[109–114] Besides morphology, grain orientation or texture also has profound effect on transport properties.[110,115–118] Better film quality facilitated by these advances in processing has been vital in the improvement of OIHP LED performance, and the reported emission spectra have shown high color purity with ~20nm EL FWHM.[21,119] High color purity is desired to realize a wide color gamut in high resolution displays. We believe with new processing to further improve perovskite film quality, the EL line width can be further narrowed to approach the 100% color purity limit. Recently, ion exchange has been used in perovskites for facile composition engineering, morphology and crystallinity control.[120,121] Thus, ion exchange can be a promising new method to further improve bromide-based perovskites film quality and realize ultrahigh color purity emission.

In this work, we have developed an ion exchange method for conversion from 2D to 3D perovskite to grow highly oriented $MAPbBr_3$ thin films. We found out that the transition between 2D and 3D perovskites through ion exchange is not reversible for all 2D perovskites. The thermodynamics and kinetics of this reaction can be affected by intermolecular interaction and ammonium functionality of 2D perovskite organic cations. A monoamine-based 2D perovskite PEA_2PbBr_4 was selected as a growth template and successfully exchanged into $MAPbBr_3$. The resulting $MAPbBr_3$ thin films show much improved substrate coverage, and preservation of the highly-aligned orientation of the original 2D perovskite. Improved film characteristics lead to extremely narrow green EL with a record 15.3 nm (67 meV) FWHM compared to ~20 nm reported so far, and thus possessed 98.10% color purity. This elucidates the potential of ion exchange in conjunction with 2D perovskite growth template as new a processing method to fabricate high quality OIHP thin films for optoelectronic applications.

5.2 RESULTS AND DISCUSSION

5.2.1 *Mechanism of Ion Exchange Reaction between 2D and 3D Perovskites*

A new growth method of multi-dimensional perovskites has been reported by Mhaisalkar *et al.* for photovoltaic applications,[120] where a 2D perovskite thin film was dipped into MAI solution to grow 2D/3D hybrid perovskites. This example shows the potential of using 2D perovskites as a growth template for 3D perovskites and facilitates morphology control. To take advantage of this approach, it is critical to pinpoint the governing reaction mechanism. In this regard, there are several key questions: 1. Is this reaction reversible and applicable to all kinds of 2D perovskites? 2. Will the strong texture of 2D perovskite affect the grain orientation feature of the resultant 3D perovskites? 3. Can this method be extended to improve the thin film quality of $MAPbBr_3$ and associated light emission characteristics? To answer these questions, understand the underlying reaction mechanism and uncover design rules, we employed a combination of experimental and theoretical studies.

Four different ammonium iodides, which can all form 2D perovskites when mixed with lead iodide, were selected to study the ion exchange reaction mechanism between the corresponding 2D perovskites and $MAPbI_3$.[97,122,123] They are $CH_3(CH_2)_3NH_3I$ (C4-mono-I), $C_6H_5(CH_2)_2NH_3I$ (PEAI), $NH_3I(CH_2)_4NH_3I$ (C4-di-I_2), and $NH_3I(CH_2)_2O(CH_2)_2O(CH_2)_2NH_3I$ ($EDBEI_2$); their molecular structures are shown in **Figure 5.1A**. All four 2D perovskite thin films were dipped into MAI solution in IPA to test if the 2D perovskites can be converted into $MAPbI_3$ (**Figure 5.1B**). Similarly, the reverse-reaction was initiated by dipping $MAPbI_3$ thin films into C4-mono-I, PEAI, C4-di-I_2 and $EDBEI_2$ solution in IPA, respectively.

Going from 3D to 2D, after ion exchange the film color changed from brown to yellow, with the appearance of exciton absorption peaks at 490-520 nm and the disappearance of $MAPbI_3$ band-edge absorption at 780 nm. (**Figure 5.1C**) Both features indicate successful conversion from 3D $MAPbI_3$ to 2D perovskites. Surprisingly, under these conditions, the conversion from 2D to 3D perovskite does not happen to all four materials as observed in the bottom part of **Figure 5.1C**. The failed transition from (C4-di)PbI_4 and (EDBE)PbI_4 to $MAPbI_3$ indicates a significant difference between monoamine and diamine-based 2D perovskites with regard to this ion exchange process. To uncover the origin of observed selectivity for ion exchange reaction, we subsequently performed theoretical calculations of the thermodynamics and kinetics for the ion exchange process.

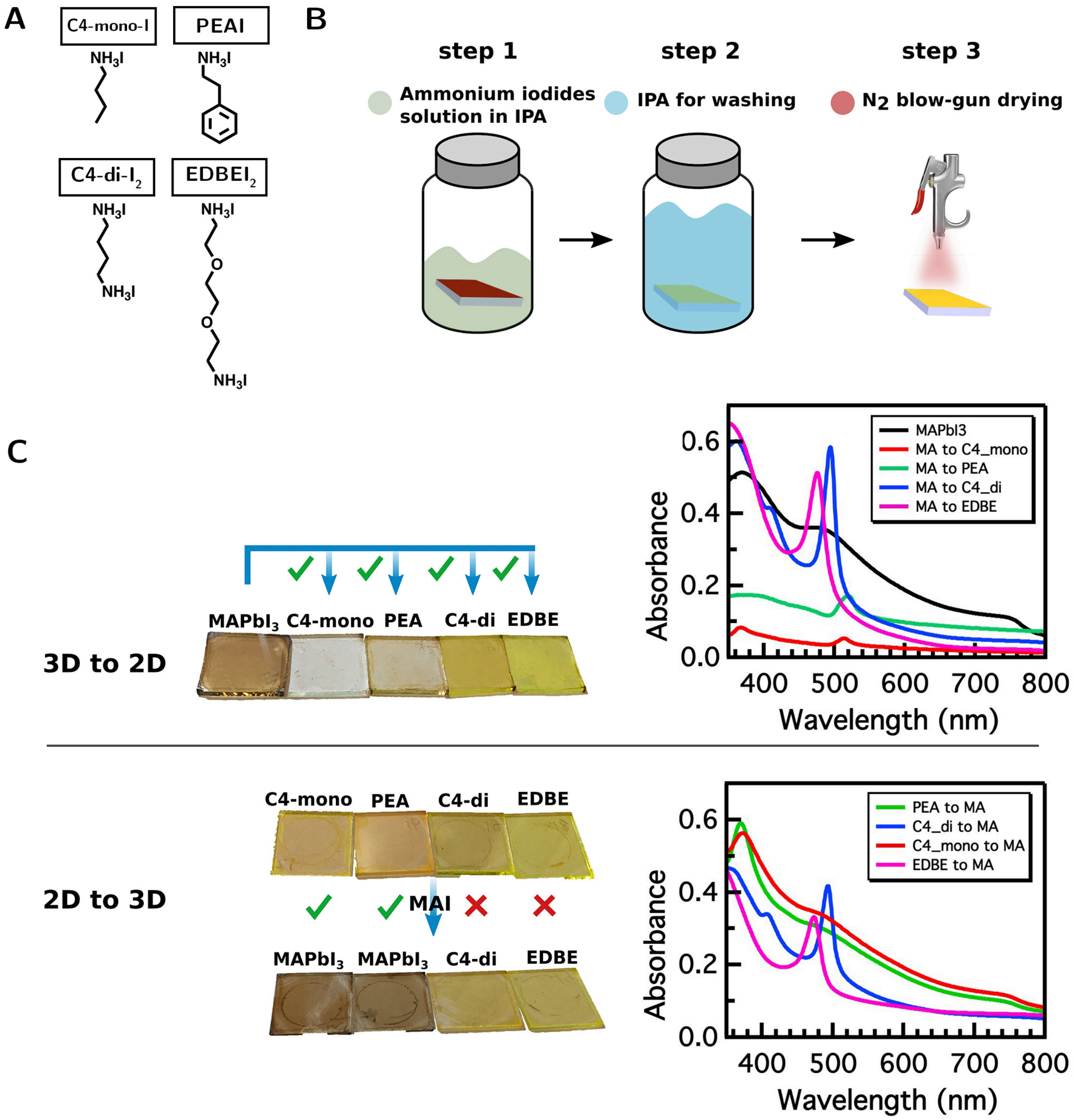

Figure 5.1. (A) Molecular structure of four ammonium iodides: C4-mono-I, PEAI, C4-di-I_2 and $EDBEI_2$. **(B)** Schematic illustration of the ion exchange process in this study. **(C)** Color change and UV-vis absorption feature evolution of thin films before and after ion exchange. The top and bottom correspond to 3D to 2D conversion, and 2D to 3D conversion, respectively.

The formation energy (E_f) of $(C4\text{-mono})_2PbI_4$, $(C4\text{-di})PbI_4$, $(PEA)_2PbI_4$ and $(EDBE)PbI_4$, (**Equation 5.4-5.7**) and the Gibbs free energies (ΔG) of the following four (**Equation 5.8-5.11**) ion exchange reactions were calculated using DFT simulations.

$$E_f = E_{(\mathrm{C4-mono})_2\mathrm{PbI}_4} - E_{\mathrm{PbI}_2} - 2E_{(\mathrm{C4-mono})\mathrm{I}} \quad (5.4)$$

$$E_f = E_{(\mathrm{C4-di})\mathrm{PbI}_4} - E_{\mathrm{PbI}_2} - E_{(\mathrm{C4-di})\mathrm{I}_2} \quad (5.5)$$

$$E_f = E_{(\mathrm{PEA})_2\mathrm{PbI}_4} - E_{\mathrm{PbI}_2} - 2E_{(\mathrm{PEA})\mathrm{I}} \quad (5.6)$$

$$E_f = E_{(\mathrm{EDBE})\mathrm{PbI}_4} - E_{\mathrm{PbI}_2} - E_{(\mathrm{EDBE})\mathrm{I}_2} \quad (5.7)$$

$$MAPbI_3 + 2(C4 - mono - I) \rightarrow MAI + (C4 - mono)_2PbI_4 \quad (5.8)$$

$$MAPbI_3 + (C4 - di - I) \rightarrow MAI + (C4 - mono)_2PbI_4 \quad (5.9)$$

$$MAPbI_3 + 2(PEAI) \rightarrow MAI + (PEA)_2PbI_4 \quad (5.10)$$

$$MAPbI_3 + EDBEI_2 \rightarrow MAI + EDBEPbI_4 \quad (5.11)$$

During calculation of E_f, the energies of each components in the equations are all based on the optimized geometries. The $(MA)PbI_3$ cell of optimization has the lattice constants *a*=8.8960, *b*=8.8960, *c*=12.6370, α=90.0000, β=90.0000, γ=90.0000. The Brillouin zone is sampled using a 3*3*2 K-space grid. (**Figure 5.2A**) The $(C4\text{-di})PbI_4$ cell of optimization has the lattice constants *a*= 8.4736, *b*=8.4736, *c*=11.0722, α=76.6790, β=70.2470, γ=89.2350. The Brillouin zone is sampled using a 3*3*3 K-mesh. (**Figure 5.2B**) The $(C4\text{-mono})_2PbI_4$ cell of optimization has the lattice constants *a*=8.8764, *b*=8.6925, *c*=27.6014, α=90.0000, β=90.0000, γ=90.0000. The Brillouin zone is sampled using a 3*3*1 K-mesh. (**Figure 5.2C**) The $(PEA)_2PbI_4$ cell of optimization has the lattice constants *a*=12.3279, *b*=12.3279, *c*=32.2770, α=90.0000, β=94.3110, γ=90.0000. The Brillouin zone is sampled using a 2*2*1 K-space grid. (**Figure 5.2D**) The $(EDBE)PbI_4$ cell of optimization has the lattice constants *a*=6.4940, *b*=29.4610, *c*=9.2621, α=90.0000, β=91.7770, γ=90.0000. The Brillouin zone is sampled using a 3*1*2 K-space grid. (**Figure 5.2E**)

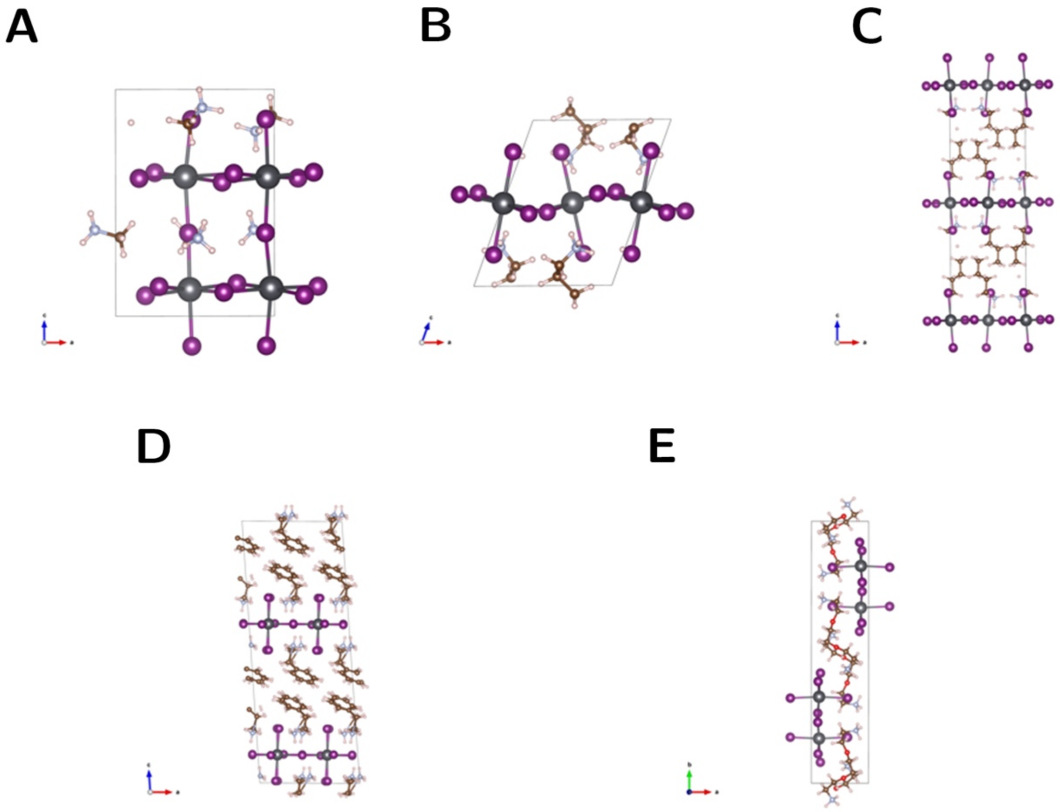

Figure 5.2. Optimized geometry for (A) $MAPbI_3$ (B) $(C4\text{-di})PbI_4$ (C) $(C4\text{-mono})_2$PbI4 (D) $(PEA)_2PbI_4$ and (E) $(EDBE)PbI_4$.

As expected, all four 2D perovskites show large E_f value ranging from 4.44 eV to 5.96 eV (**Figure 5.3A**), confirming their higher thermodynamic stability than $MAPbI_3$.[124] $(EDBE)PbI_4$ has ~0.5 eV higher E_f value than others. This is attributed to the strong hydrogen bonding between adjacent EDBE molecules that significantly stabilizes the structure.[123] From the comparison of ΔG, it shows that the reverse-reaction of **Equation 5.11** is most unfavorable thermodynamically, which correlates well with the exceptionally large E_f value of $(EDBE)PbI_4$. Based on similarity of

ΔG value for other three reactions (**Figure 5.3A**), their reverse-reaction should have a similar tendency to proceed thermodynamically. However, reverse-reaction of **Equation 5.9** didn't proceed, while $(C4\text{-mono})_2PbI_4$ and $(PEA)_2PbI_4$ in **Equation 5.8** and **Equation 5.10** successfully transformed into $MAPbI_3$. The conflict between the ΔG calculations and the experimental results reveals that besides the influence of reaction thermodynamics on 2D to 3D conversion, consideration of reaction kinetics is also important.

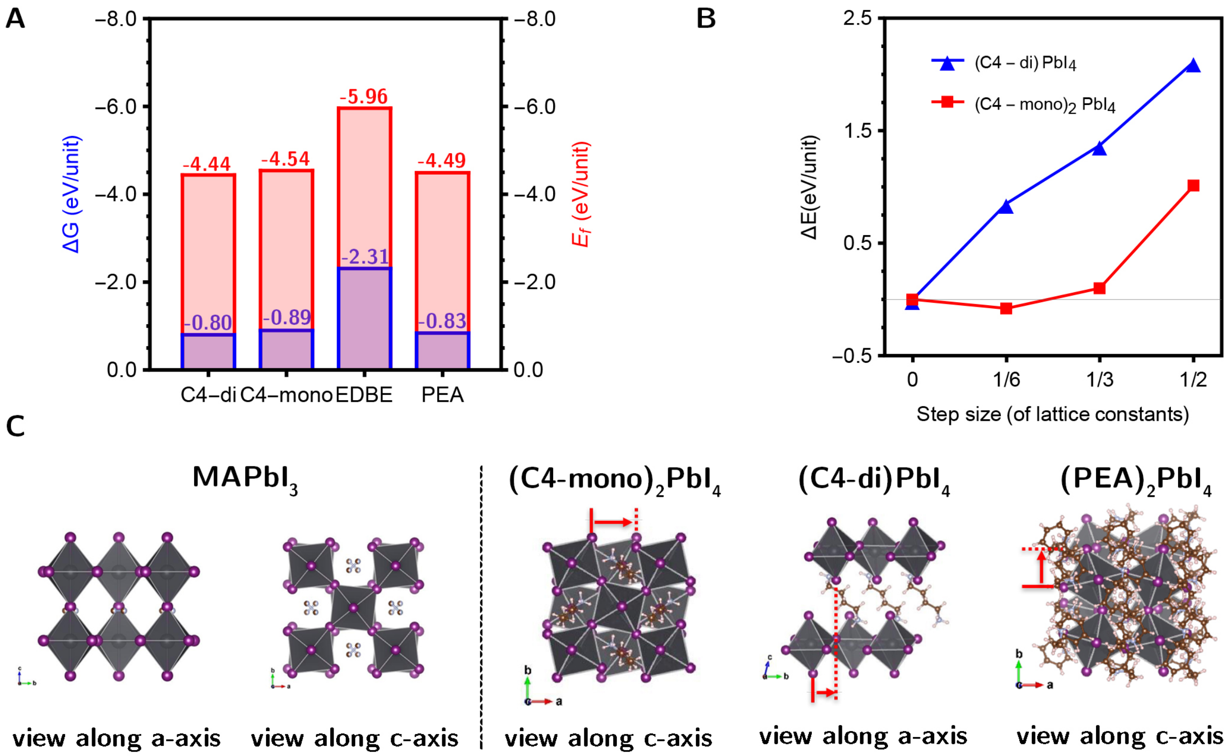

Figure 5.3. (A) The Gibbs free energies of reaction 1-4 and the formation energies of the four 2D perovskites. **(B)** The lateral translation barrier in three layer $(C4\text{-di})PbI_4$ and $(C4\text{-mono})_2PbI_4$. The total energies of $(C4\text{-mono})_2PbI_4$ and $(C4\text{-di})PbI_4$ are scanned along the red arrow by half of the lattice constants. **(C)** The scheme of lateral translation in $MAPbI_3$, $(C4\text{-mono})_2PbI_4$, $(C4\text{-di})PbI_4$ and $(PEA)_2PbI_4$ crystals.

When the $MAPbI_3$ lattice is viewed along the normal of (001) plane, two adjacent (001) planes consisting of Pb and I are almost overlapped (**Figure 5.3C**). However, $(C4\text{-}mono)_2PbI_4$, $(C4\text{-}di)PbI_4$, and $(PEA)_2PbI_4$ all show a lateral translation between adjacent planes by around half unit cell. Thus, the 2D to 3D conversion is accompanied by lateral translation of inorganic planes, which eventually bonds two originally separated inorganic layers together with corner-shared octahedra. This observation led us to propose that the failure of reverse-reaction of **Equation 5.9** is mainly due to its high reaction barrier for lateral translation. This can arise from the high rigidity of diamine-based perovskites, where both ammonium ends of each organic molecule are hydrogen/ionic bonded to inorganic layers. Whereas in monoamine-based perovskites, the weak Van der Waals interaction between two organic sub-layers gives much higher flexibility.

The complicated potential energy surface of this system adds a lot of difficulty for accurate calculation of transition states to study kinetics. As a result, we used an alternative strategy here to calculate the lateral transition barrier along the *ab* plane. We chose C4-mono and C4-di for comparison due to their similar molecular structure differing only in ammonium functionality. Here, 3-layer slab models have been extracted from the optimized $(C4\text{-}di)PbI_4$ and $(C4\text{-}mono)_2PbI_4$ geometries. A 30 Å vacuum layer has been added to the *c* axis. The top layer of the $(C4\text{-}mono)_2PbI_4$ was translated by ($a/6$, 0, 0), ($a/3$, 0, 0) and ($a/2$, 0, 0). The top layer of the $(C4\text{-}di)PbI_4$ was translated by ($a/6$, $b/6$, 0), ($a/3$, $b/3$, 0) and ($a/2$, $b/2$, 0). After the translation, the three PbI_6 layers are fixed and the interlayer molecules are relaxed for a geometry re-optimization. The energies of the re-optimized geometries are then used to calculate the translation barriers. (**Figure 5.4**)

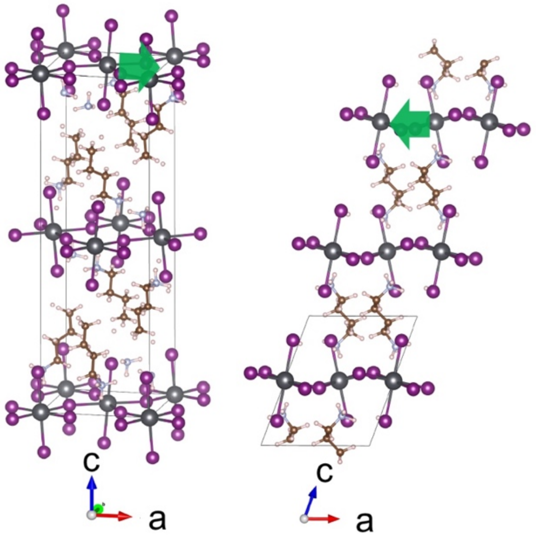

Figure 5.4. The scheme of lateral translation in three layer (C4-di)PbI_4 and (C4-mono)$_2PbI_4$ slab models. The total energies are scanned along the green arrow by half of the lattice constants.

The results are shown in **Figure 5.3B**. The translation barrier of (C4-di)PbI_4 is consistently much higher than that of (C4-mono)$_2PbI_4$, which implies that the former has a higher repulsion during ion exchange and the reaction is not kinetically favored. The conversion between 2D perovskites and $MAPbI_3$ is thus not universally reversible. Its selectivity is governed by both thermodynamics and kinetics of the exchange process. Thermodynamically the 3D to 2D conversion is always energetically favorable and can proceed successfully. However, the reverse-reaction can be inhibited if strong intermolecular interaction (such as hydrogen bonding between EDBE molecules) exists. In addition, diammonium functionality introduces large rigidity into the lattice, which can restrain lateral translation of inorganic planes and prevent the reverse-reaction from happening.

5.2.2 *Orientation and Morphological Control of MAPbBr3 through Ion Exchange*

With the above mechanistic understanding about ion exchange reaction between 2D and 3D perovskites, we learned that monoamine-based 2D perovskites are desirable to be exchanged into 3D perovskites. To study the effectiveness of this processing method in controlling $MAPbBr_3$ thin film morphology, PEA_2PbBr_4 was chosen as the 2D perovskite growth template and exchanged into $MAPbBr_3$ following the same process shown in **Figure 5.1B**. To examine whether the ion exchange reaction was complete, XRD and Ultraviolet-visible (UV-vis) absorption analysis were performed for one-step spin-coated $MAPbBr_3$ (as reference film), PEA_2PbBr_4, and $MAPbBr_3$ exchanged from PEA_2PbBr_4 (referred as exchanged film). From **Figure 5.5A**, it is clear that the diffraction from (002) plane of PEA_2PbBr_4 at 2θ value of 5.32° was not observed in XRD pattern for exchanged film and the diffraction from (100) plane of $MAPbBr_3$ appeared strongly at 14.96°. Consistently, the exciton absorption peak of PEA_2PbBr_4 at 400 nm has completely disappeared after ion exchange, and the UV-vis absorptance spectrum matches that of reference film, (**Figure 5.5B**) but has higher absorbance at shorter wavelengths due to better surface coverage.[125] We also noticed that a characteristic exciton absorption peak appeared around 530 nm in the exchange film, which may indicate large grain size (>200nm) according to previous reports.[126]

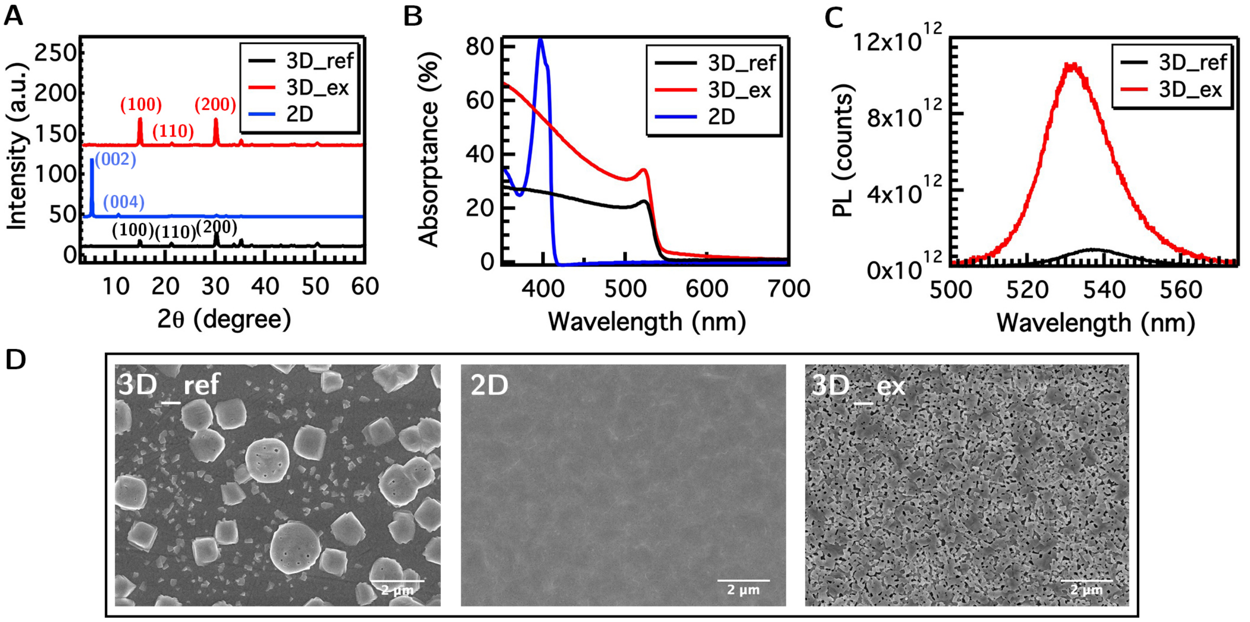

Figure 5.5. (A) XRD, **(B)** UV-vis absorption, and **(D)** SEM of reference 3D_ref, 3D_ex and 2D. **(C)** Steady-state PL of 3D_ref and 3D_ex. Note: '3D_ref', '3D_ex', and '2D' correspond to reference $MAPbBr_3$, exchanged $MAPbBr_3$, and PEA_2PbBr_4 films respectively. Traces in Figure 3A are offset vertically.

Knowing the completeness of 2D to 3D perovskite conversion, SEM characterization was then conducted to investigate the morphological differences (**Figure 5.5D**). The µm-sized cube-shaped crystals were observed in the control $MAPbBr_3$ film,[111] and the 2D perovskite PEA_2PbBr_4 template film showed a continuous film. Importantly, the $MAPbBr_3$ grown from the 2D template film showed a clear distinction in morphology as compared to the control film: large separated cubic crystals no longer exist, instead a much denser film with plate-like crystallites is produced. It should be noted that small voids formed after ion exchange is probably due to the lattice translation during this process (**Figure 5.5D**). The single crystal structure of (PEA)2PbBr4 (**Figure 5.6D**) shows that there's an around half unit cell lattice translation along a-axis.

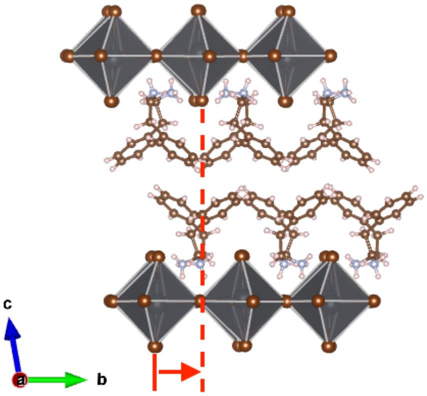

Figure 5.6. Scheme of half unit cell lattice translation in $(PEA)_2PbBr_4$ viewed along a-axis.

However, the bottom layer was not exposed in exchanged film (confirmed by surface analysis measurements) and thus no direct leakage pathway was created. UPS and XPS surface analysis were performed on reference $MAPbBr_3$ and exchanged $MAPbBr_3$ films to study film surfaces. Films studied here are spin-coated on ITO/PEDOT:PSS substrate, where PEDOT:PSS is a hole-transporting material commonly used in OIHP LED devices.

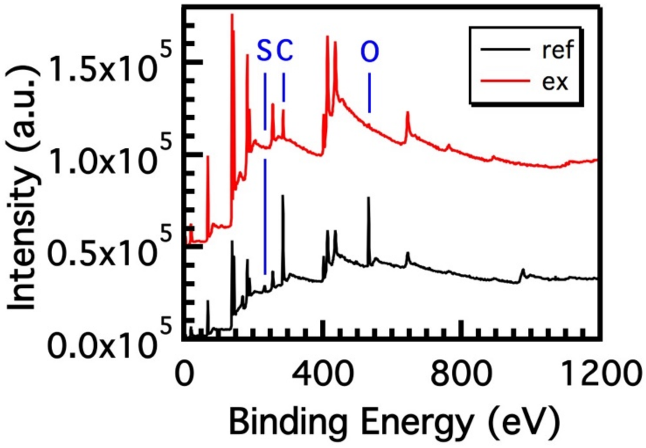

Figure 5.7. XPS spectra of reference and exchanged $MAPbBr_3$ films.

From the XPS composition results (**Table 5.4 and Figure 5.7**), the reference $MAPbBr_3$ film shows strong O and S signals, with the ratio between the two matching that in PEDOT:PSS composition. This suggests that PEDOT:PSS was not fully covered in reference film, which is obvious from the SEM results. However, no S and negligible O signal could be found in the exchanged $MAPbBr_3$ film. This result indicates that, although lattice translation can introduce voids between crystallites, it doesn't create direct pathways from the bottom layer to top surface, which is a benefit of using the layered 2D perovskite structure as growth template. XPS spectra of reference and exchanged $MAPbBr_3$ films. The valence band maximum of extracted from UPS characterization were 6eV for reference film and 6.15eV for exchange film, (extracted from **Figure 5.8**) consistent with previous reports.[127]

Table 5.4. Composition of reference and exchanged $MAPbBr_3$ films extracted from XPS analysis.

	C 1s	O 1s	Pb 4f	Br 3p	N 1s	Na 1s	S 2s
Control	61.06%	16.91%	1.91%	6.52%	9.31%	0.60%	3.70%
C8 treated	34.96%	1.99%	8.02%	29.7%	25.33%		

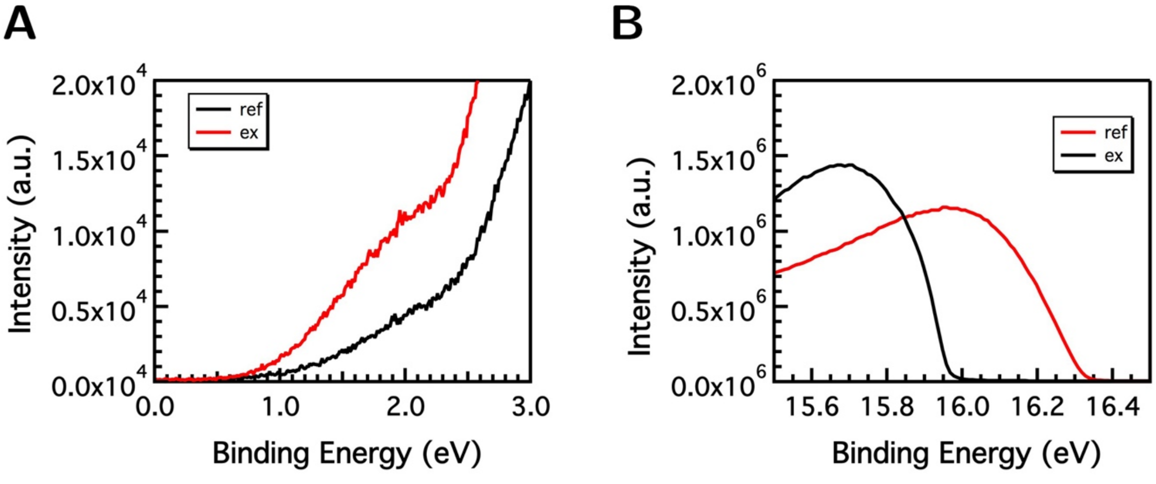

Figure 5.8. (A) UPS spectrum of top occupied states and **(B)** photoemission cut-off for reference and exchanged $MAPbBr_3$ films.

In addition to the difference in film coverage between reference and exchanged $MAPbBr_3$ films, a huge improvement in crystallinity and orientation order was found in the exchanged film. The 2D XRD patterns of the three films are shown in **Figure 5.9A**. In 2D XRD, γ degree is defined as direction of diffracted beam on the diffraction cone, so that the distribution of γ of a specific 2θ diffraction represents the orientation order of the related plane in the crystal.

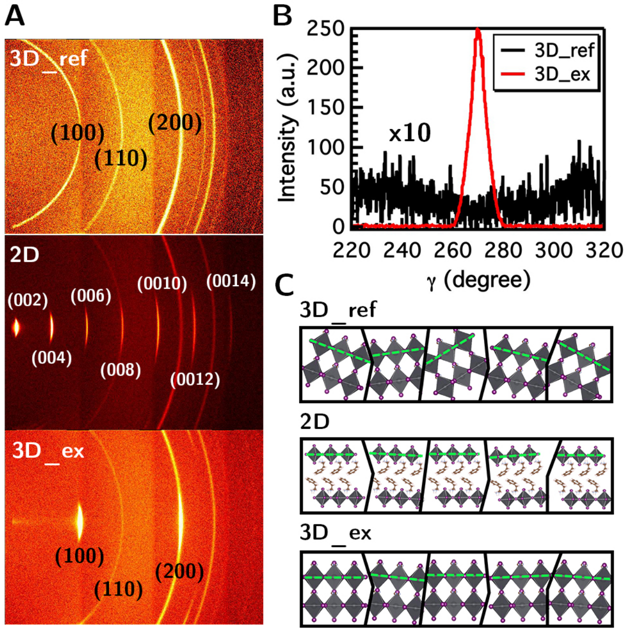

Figure 5.9. (A) 2D XRD pattern and **(C)** Schematic demonstration of crystallite orientation in 3D_ref, 2D, and 3D_ex. **(B)** XRD intensity versus gamma of 3D_ref and 3D_ex thin films (magnified 10 times for 3D_ref film due to its weak XRD intensity). Note: '3D_ref', '3D_ex', and '2D' correspond to reference $MAPbBr_3$, exchanged $MAPbBr_3$, and PEA_2PbBr_4 films respectively.

Comparing the (100) diffraction from the reference and the exchanged $MAPbBr_3$, the former shows a ring spanning over the whole detector area and the intensity at different γ degree is similar. Strikingly, the latter shows very confined diffraction signals concentrated at the middle region of the detector. This indicates that the reference film is polycrystalline with random crystallite orientation, while the exchanged film is highly oriented with (100) plane mostly parallel to the substrate.[117,128] The preferred [100] growth in exchanged film can also be evidenced by the weakening of (110) diffraction in **Figure 5.9A**.

To quantitatively analyze the orientation order, a γ scan was conducted on reference and exchanged films for (100) diffraction. As shown in **Figure 5.9B**, the reference film shows no observable feature confirming its random crystallite orientation, while the exchanged film shows a distinct peak with a FWHM of 7.06°. This much-improved orientation order after ion exchange can be attributed to templating provided by 2D perovskites, which preferably grow in [001] direction. (**Figure 5.10**)

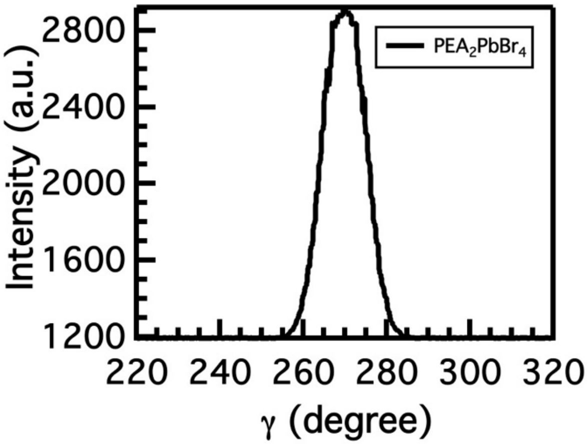

Figure 5.10. XRD intensity versus gamma of PEA_2PbBr_4 thin film.

A scheme showing the possible crystallite orientation distribution is shown in **Figure 5.9C**. To test the generality of ion exchange from 2D to 3D perovskite to control the orientation of perovskite thin films, we performed same 2D XRD characterization on iodide-based perovskites.

Strong texture can be observed in the resulting $MAPbI_3$ film exchanged from PEA_2PbI_4 (**Figure 5.11**), similar to the bromide-based perovskites discussed above. This result demonstrates the effectiveness of this method in tuning grain orientation independent of the halide composition.

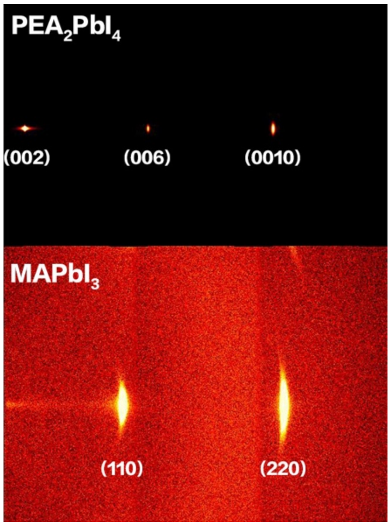

Figure 5.11. 2D XRD pattern of PEA_2PbI_4 and $MAPbI_3$ thin films.

It has been demonstrated by Zhu *et al.*[116] that uniaxially-oriented perovskite thin films have 300% higher mobility and much reduced defect density compared to randomly oriented films. Besides higher orientation order, the excess amount of MABr in solution during ion exchange can potentially reduce the equilibrium defects concentration of vacancy defects (V_{MA} and V_{Br}),[84] which are otherwise readily formed in large concentration because of their low formation energies.[129] We therefore performed PL studies to assess the optoelectronic quality of exchanged film in comparison to reference $MAPbBr_3$. As observed from the PL spectra (**Figure 5.5C**), the exchanged film has ~10 times higher PL intensity compared to reference film. The dramatic PL intensity increase implies enhanced radiative recombination and is indicative of the improved quality of exchanged film. It was noted that there is 7.2nm (31meV) PL blue-shift in exchange film compared to reference from 539.2nm to 532.0nm. The blue-shift can possibly result from several reasons, including residual 2D perovskite phase in exchanged films, reduction of sub-band gap trap states, and different morphology feature. To uncover the origin of PL blue-shift in exchange film, we conducted 1D powder XRD to find out whether there's residual $(PEA)_2(MA)_{n-1}Pb_nBr_{3n+1}$ phase with large n value in exchanged film. Although the absorption feature and XRD pattern is almost indistinguishable between n=60 and n= infinity films, it has been shown[124] that the XRD pattern of a powder scratched from thin film shows diffraction at small angle ($2\theta<10^o$) even when n=60.

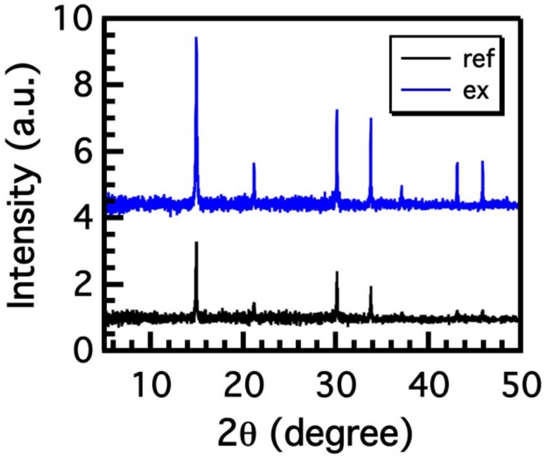

Figure 5.12. 1D XRD of powder scratched from reference and exchange films.

We performed similar experiment on reference and exchange films by taking XRD measurements with a 1D detector on powder scratched from thin films. From the results (**Figure 5.12**) we find there is no diffraction signal from small 2θ angles and we therefore exclude the possibility that residual quasi 2D perovskites are responsible for the changes in PL properties. Pinpointing the exact reason for PL blue-shift is not within the scope of this work and will need detailed investigation in the future. To further assess the optoelectronic quality of the exchange film, we measured time-resolved photoluminescence and observed a 33% average lifetime increase in exchanged film compared to the reference (**Figure 5.13**), which indicates reduction of trap states. Thus, the increased PL intensity, PL blue-shift and higher average lifetime altogether confirm the higher quality of exchanged film with reduced non-radiative recombination centers compared to the reference film.[130,131] The higher orientation order and improved optoelectronic quality achieved using ion exchange technique is promising, and the exchanged $MAPbBr_3$ has immense prospects for high color purity light emission applications.

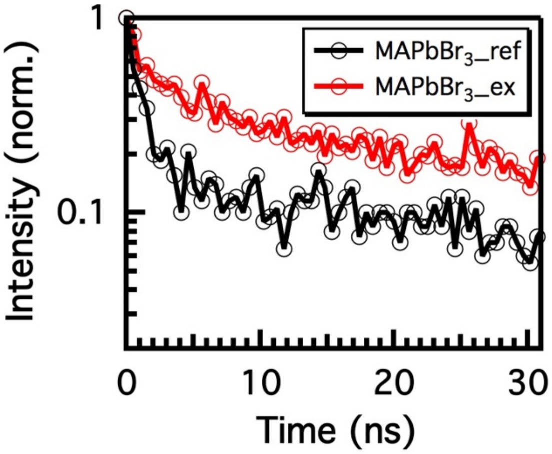

Figure 5.13. Time-resolved photoluminescence of reference and exchange $MAPbBr_3$ films, the intensity weighted average lifetimes of which are 11.528ns and 15.283ns respectively.

5.2.3 *Color Purity of Green Light Emission*

The definition of color purity or color saturation of a light source is demonstrated in **Figure 5.14A**.[132] The perimeter of the chromaticity diagram corresponds to a color purity of 100%, as desired for monochromatic light sources. To achieve a broad color reproduction range for displays, high color purity is critical. Requirements are more stringent for green light since the human eye has a higher sensitivity to green, and thus can identify a larger number of tones in the green spectral region.[119,133]

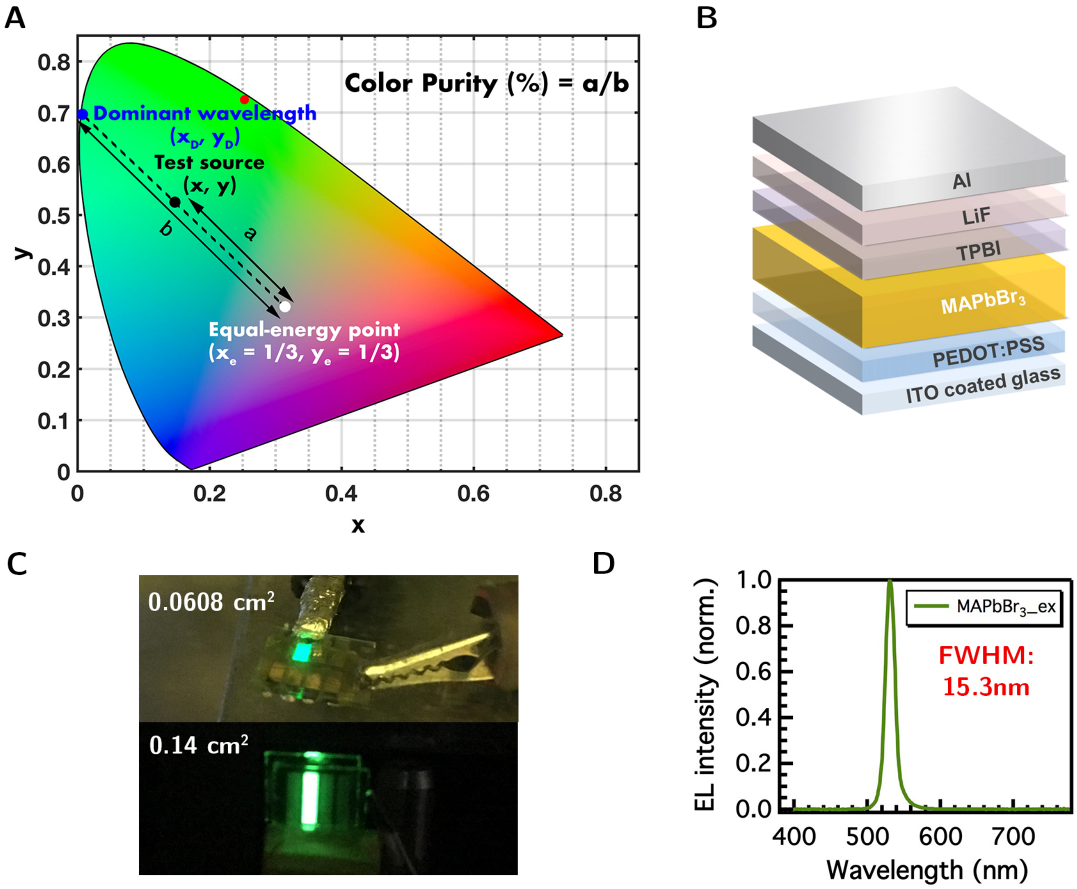

Figure 5.14. **(A)** The color coordinates of our device and definition of color purity on the CIE 1931 color space. The color purity or color saturation of a light source is the distance in the chromaticity diagram between the (x, y) color-coordinate point of the test source and the coordinate of the equal-energy point ($x_e = 1/3$, $y_e = 1/3$) divided by the distance between the equal-energy point and the dominant-wavelength point (x_D, y_D). **(B)** Device architecture, **(C)** Green light emission photos, and **(D)** EL spectrum of $MAPbBr_3$ LEDs using ion exchange processing method.

To analyze the impact of the improved morphology and orientation order of $MAPbBr_3$ obtained by ion exchange method on emission characteristics, LED devices were constructed with a standard architecture of ITO/PEDOT:PSS/$MAPbBr_3$/TPBI/LiF/Al. (**Figure 5.14B**) Devices exhibited pure green-light emission (**Figure 5.14C**). The EL spectrum (**Figure 5.14D**) measured at 3V bias shows a narrow peak centered at 531nm with 15.3 nm FWHM. Statistical EL FWHM distribution is shown in **Figure 5.15**.

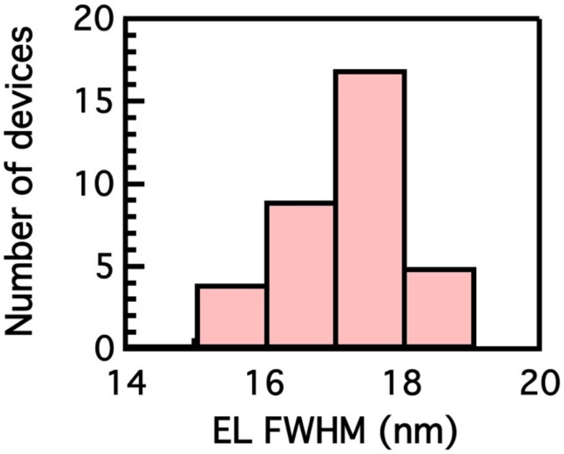

Figure 5.15. EL FWHM distribution of $MAPbBr_3$ LED devices processed from ion exchange method.

This is by far the narrowest EL FWHM reported for 3D perovskite thin film LEDs at room temperature. The previously reported state-of-the-art EL FWHMs for different types of perovskite LEDs are: 17nm from $CsPbBr_3$ nanocrystals,[134] 16nm from polymer-assisted $CsPbBr_3$ bulk thin film,[135] and 14nm from PEA_2PbBr_4 nanoplates.[136] For $MAPbBr_3$ however, EL FWHMs are >20 nm. 2D/3D hybrid perovskite LEDs have much wider EL emission (FWHM > 40nm)[137] due to the compositional heterogeneity between grains. The emitted green light of our device corresponds to Commission Internationale de l'Eclairage (CIE) color coordinates of (0.2539, 0.7291), labeled as the red dot in **Figure 5.14A**. It has dominant wavelength of 543nm located at (0.2513, 0.7366). The color purity of this light is then calculated to be as high as 98.10%.

The narrow EL linewidth is of technological importance and its origin in the context of this work can be attributed to factors ranging from unique crystallographic properties of the exchanged $MAPbBr_3$ film to device photonic effects. To understand the role of weak microcavity effects related to the thin film interference in LED device stack on the observed narrow EL linewidth, we compared the PL spectrum of exchanged $MAPbBr_3$ on glass with the PL spectrum from a device pixel on an exchanged $MAPbBr_3$ LED (**Figure 5.16**).

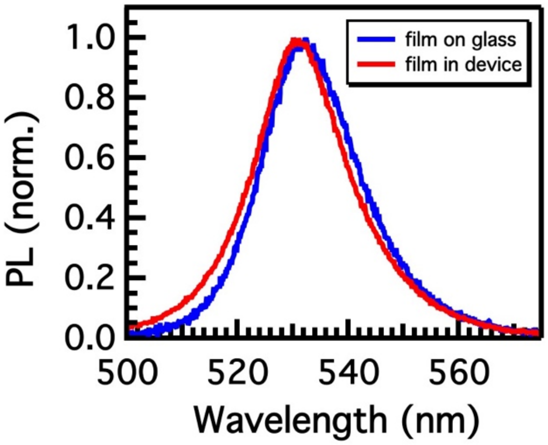

Figure 5.16. Comparison between PL of exchanged $MAPbBr_3$ on glass and exchanged $MAPbBr_3$ in LED device. The PL FWHM of the film on glass and the film in the device structure are 19.9nm and 19.7nm respectively. The similar PL FWHM for the films on glass and in device structure suggests that there is not a strong photonic effect related to the device structure alone that is responsible for EL linewidth narrowing.

We find that the FWHM of the PL spectra of the film on glass and the device pixel are very similar, suggesting that photonic effects related to the device structure play only a minor role in the narrow EL linewidth. Thus, we propose that the narrow EL is most likely be due to the unique thin film properties, including the ordered crystal orientation, relatively large grain size, and perhaps a concomitant reduction in trap density. Future studies will be required to solidify this hypothesis.

The corresponding current density and luminance versus voltage (J-L-V), EQE and current efficiency versus voltage characteristics of devices based on exchange film are shown in **Figure 5.17.** Devices based on reference films either don’t light up at all or die instantly when turned on even when they are encapsulated, due to the poor coverage and high roughness of reference films. Currently, the performance metrics (EQE and current efficiency) of our devices based on exchanged films are constrained by voids between grains in exchanged films possibly arising from lattice translation during ion exchange. Further process and device optimization can relieve constraints to improve device performance and fully capitalize the potential of platform developed here. In this work, we focus on unveiling mechanistic picture for ion exchange and associated process development. The ultrahigh color purity demonstrated here shows the importance of orientation control and great potential of this new processing in realization of high-resolution displays. In future work, broad perovskite compositional space can be explored to utilize different 2D perovskite templates for further improvement in perovskite layer quality. Besides that, through tuning the ammonium salt composition in IPA, 2D/3D hybrid perovskite, or mixed cation perovskites can be fabricated with high orientation order, which are valuable for a wide range of optoelectronic applications.

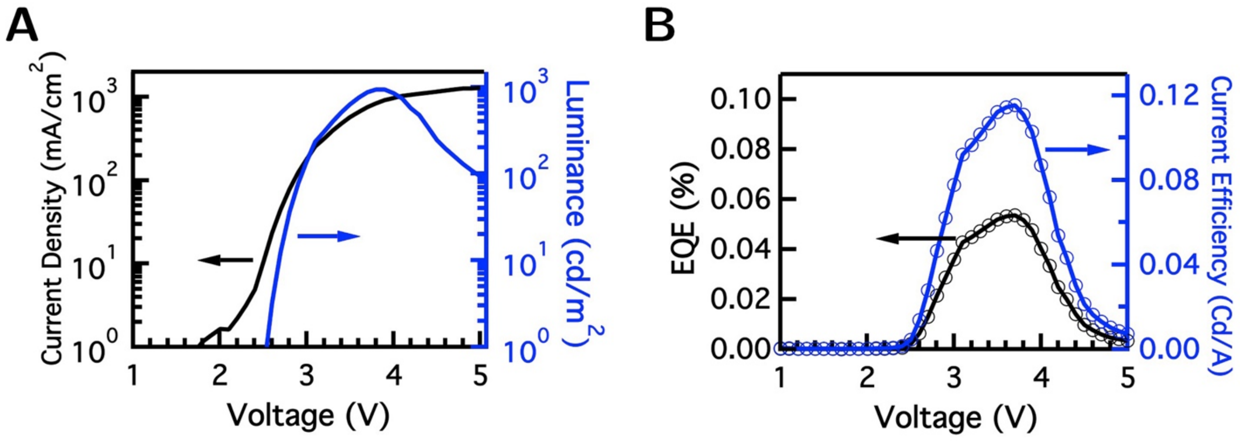

Figure 5.17. **(A)** J-V-L, and **(B)** EQE and current efficiency versus voltage for 0.0608cm^2 $MAPbBr_3$ device processed through ion exchange. The highest luminance of 945 cd/m^2 was achieved at J of 918 mA/cm^2 and V of 3.9V, and the turn-on voltage (luminance reaching 1 cd/m^2) was 2.52V. Highest EQE and current efficiency were achieved at 0.05% and 0.12 cd/m^2 respectively under 3.7V bias.

5.3 CONCLUSION

In this study, we have discovered selective ion exchange reactivity between 2D and 3D perovskites. Through theoretical calculations we found out that the intermolecular interaction and ammonium functionality of organic cations largely affect the thermodynamics and kinetics of this ion exchange reaction. Conversion from 2D to 3D perovskites can be inhibited thermodynamically when strong hydrogen bonding exists between adjacent organic cations which stabilizes the structure. Diammonium functionality can induce a more rigid crystal lattice, which raises the energy barrier of lattice translation during ion exchange reaction and thus prevents the 2D to 3D conversion from happening kinetically. With a better understanding of the reaction conditions and mechanism, we successfully exchanged PEA_2PbBr_4 thin film into $MAPbBr_3$. The resulting film has an improved morphology and better coverage. Benefitting from the preferred growth of PEA_2PbBr_4 in the [001] direction, the $MAPbBr_3$ after exchange exhibits high orientation order. This improved order is associated with a reduce crystallographic defect density and the resulting films exhibit extremely narrow green light emission with a FWHM as narrow as 15.3 nm and color purity as high as 98.10%. The outstanding thin film and emission characteristics achieved by 2D to 3D ion exchange demonstrates the great potential of this processing method in realizing high quality perovskite thin films for high resolution displays. We believe this study opens up a new realm of opportunities for future development of highly-oriented hybrid perovskite thin film for optoelectronic applications.

Chapter 6. CONCLUSION AND FUTURE PERSPECTIVES

This chapter first summarizes the improvement of OIHPs thin film quality through morphological and interfacial manipulation covered through this dissertation. Future perspectives on how to further improve OIHP film quality based on this study is also provided.

6.1 CONCLUSION

OIHPs are promising semiconductors for various optoelectronic devices including photodetection, energy harvesting, and light-emitting devices. The device performance however, is highly dependent on film quality including surface morphology and defects level. This study utilizes the versatile chemistry OIHPs share due to contribution from both organic and inorganic components.

In chapter 3, MA vapor post-treatment was introduced to improve $MAPbI_3$ film coverage, crystallinity and PSC device performance. Hydrogen bonding between MA^0 and organic sublattice of $MAPbI_3$ can result in an intermediate phase formation when film was exposed to MA vapor and was dissolved into a liquid phase. Solid state $MAPbI_3$ was obtained again through recrystallization once MA vapor was removed from the environment. The sudden drop of MA vapor pressure induces supersaturation of the MAPbI3·xMA intermediate and high nucleation rate of $MAPbI_3$. As a result, film quality was hugely improved after the treatment enhancing PCE of PSC by 9%.

Chapter 4 and 5 both use ion exchange where IPA can only dissolve the organic component of OIHPs. In chapter 4, we use C8 to post-treat $MAPbI_3$ thin film. Although for this process all other organic cations can induce phase transformation from 3D to 2D perovskite in the bulk film, C8 can only exchange the surface layer and thus passivate surface and GB defects without forming 2D phase can preventing charge transport. This is due to the uniquely high activation energy of

3D to 2D phase transformation when anti-gauche isomerization is required for C8 during this process. Consequently, the thin-film PSC passivated by C8 improved PCE to 17.2% from 14.7% of control device. Instead of only exchanging the surface organic cations, chapter 5 investigated using 2D perovskite as a growth template to be fully exchanged into highly oriented 3D perovskites. The success of this exchange is dependent on ammonium functionality of the 2D perovskite organic cation. Ion exchange is accompanied by inorganic layer lattice translation. Diammonium cations are more strongly bonded to the inorganic sublattice, almost doubling the energy barrier during translation process. Thus, only monoamine-based 2D perovskites can realize phase transformation from 2D to 3D perovskites. With a better understanding of this reaction, PEA_2PbBr_4 was successfully exchanged it into high quality 3D $MAPbBr_3$ films with strong uniaxial 100-orientation. The enhanced film quality leads to ultra-narrow electroluminescence spectra with 15.3 nm FWHM and 98.10% color purity and shows great potential for achieving ultrahigh resolution displays.

6.2 FUTURE PERSPECTIVES

6.2.1 *2D perovskite capping on 3D perovskite*

In chapter 4 we tried to control the ion exchange to only happen at film surface, so that no bulk 2D perovskite phase will form to deteriorate device performance. Recently people have achieved high stability PSC devices with even enhanced device efficiency by forming a thin layer of 2D or quasi-2D perovskite on top of 3D perovskites through new processing method.[138–146]

As shown in **Figure 6.1a**, a capping layer of 2D PEA_2PbI_4 was in-situ grown on top of Cs/FA/MA triple-cation 3D perovskite film to simultaneously improve the performance and stability of PSCs. This was realized by spin-coating diluted PEAI solution in IPA on top of 3D perovskite film. Light absorption of 2D perovskite phase can be observed in UV-vis absorption spectrum (**Figure 6.1b**). After 2D perovskite capping, PCE was improved from 17% to 18.5% (**Figure 6.3c**) and PL lifetime measurements (**Figure 6.4d**) suggest suppressed nonradiative recombination. The device with PEA_2PbI_4 stacked on top demonstrated great moisture stability (**Figure 6.4e**), maintaining 90% PCE after exposed to ambient environment with RH 60 ± 10 for 1000hr.

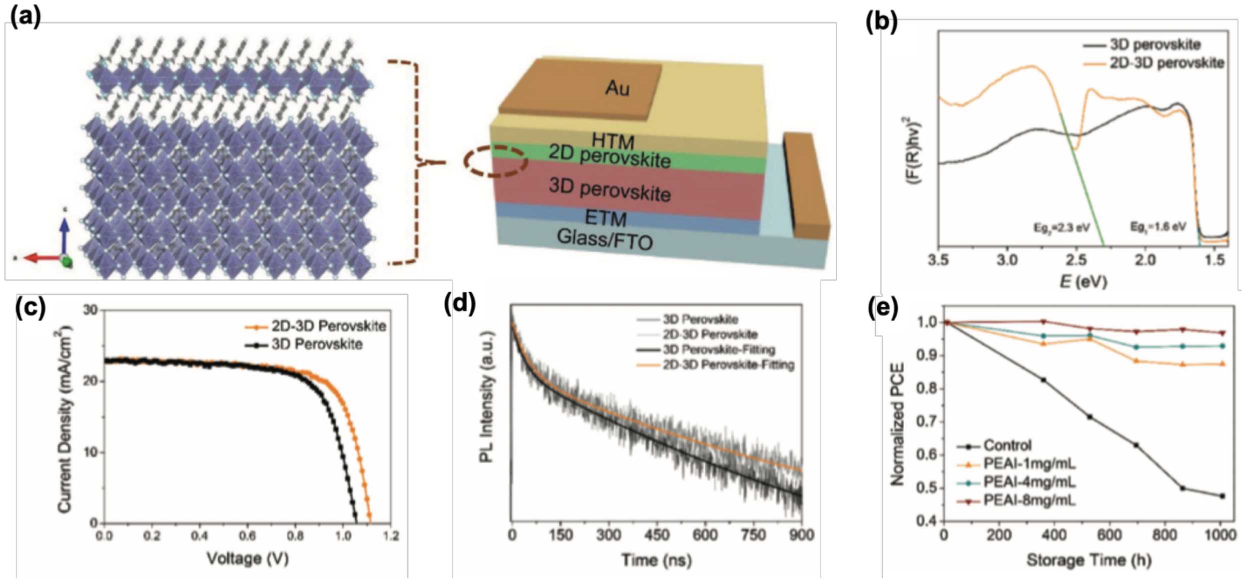

Figure 6.1. **(a)** Schematic illustrations of the crystal structure of 2D-3D perovskite films and the device architecture. **(b)** UV–vis spectra of the 3D and 2D-3D perovskite films. **(c)** *J–V* curves of the best fabricated 3D PSCs and 2D-3D PSCs under reverse scans. **(d)** Time-resolved PL decay curves of the glass/perovskite samples. **(e)** Long- term stability of normalized PCE of the fabricated 3D and 2D-3D PSCs storing in the ambient conditions with RH 60 ± 10.[141]

Although 2D perovskite capping has been shown to be a facile strategy to simultaneously improve the stability and efficiency of PSCs, PCE improvement is quite limited. This can be mainly due to the poor charge transport property of n=1 2D perovskites resulting from the insulating organic layers. Although various different large cations have been tested with similar strategy, very few studies[141] have focused on tuning the growth direction of the capping 2D perovskites on top to prevent charge transport block by horizontal growth. Since it has been demonstrated that when n is larger than 2 quasi-2D perovskite will change from horizontal to vertical growth[147], tuning its composition can be an effective way to facilitate vertical growth. Although this strategy has been tested,[141] the study is focused more on device performance enhancement without studying the composition and orientation of the top quasi-2D perovskite. In future studies, mixing large organic cations with methylammonium salts to tune growth direction can be an interesting area to dig into. Halide alloy can also be utilized to tune the surface perovskite energy level and enhance its alignment with adjacent charge transport layer on top.

6.2.2 *Highly oriented OIHP thin film with improved morphology*

Chapter 5 introduces an ion exchange processing method to fabricate almost uniaxially-oriented 3D perovskite thin film. The ion exchange process involves phase transformation from 2D to 3D perovskite. The most common 2D perovskite has around half unit cell lattice translation between adjacent inorganic layers. In 3D perovskites however, adjacent inorganic layers are almost 100% overlapped with small twist between octahedra. (**Figure 6.1a**) Thus, even though one-step spin-coated 2D perovskite film has compact and smooth surface morphology, the resulting 3D perovskite after exchange shows small pinholes. (**Figure 6.2b**) Although from UPS results discussed in chapter 5, the pinholes are not through the whole layer causing small shunt resistance, roughness can be increased and adversely impact contact between perovskite and top charge transport layer. Thus, to further extract the benefit of this processing method, new 2D perovskite material system can be explored which contain small or no lattice translation between inorganic layers. This can potentially achieve 3D perovskite thin film with high orientation and morphology similar to its 2D growth template.

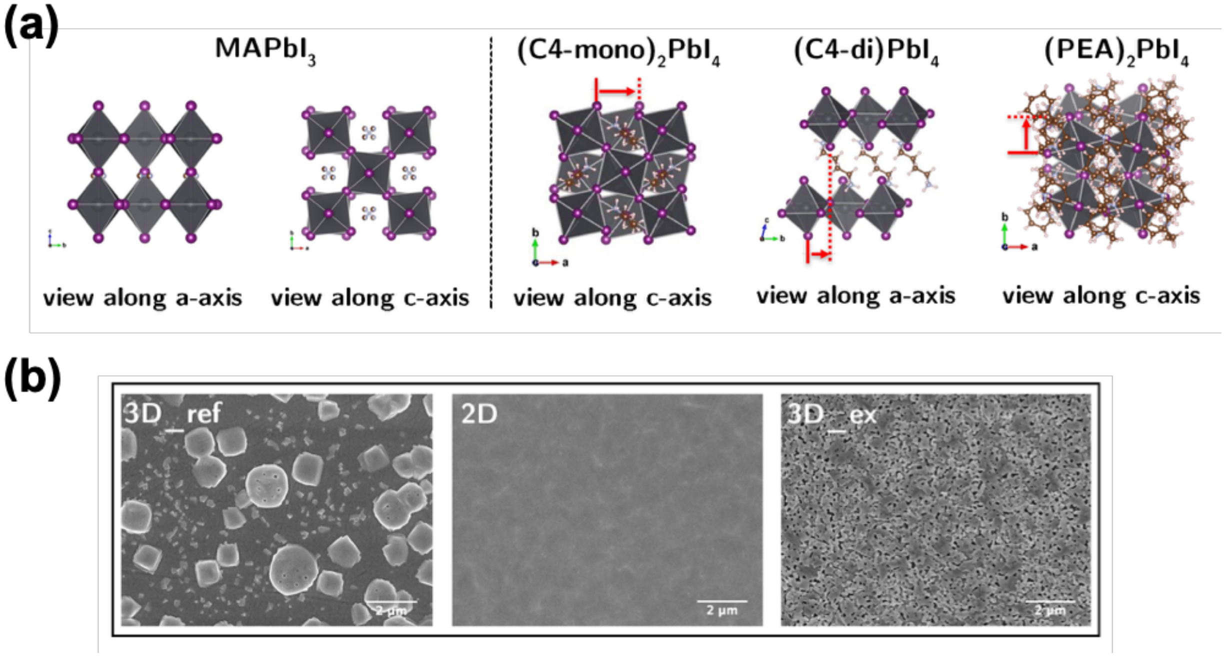

Figure 6.2. **(a)** The scheme of lateral translation in $MAPbI_3$, $(C4\text{-}mono)_2PbI_4$, $(C4\text{-}di)PbI_4$ and $(PEA)_2PbI_4$ crystals.

(b) SEM of reference 3D_ref, 3D_ex and 2D.

BIBLIOGRAPHY

(1) Green, M. A.; Ho-Baillie, A.; Snaith, H. J. The Emergence of Perovskite Solar Cells. *Nat. Photonics* **2014**, *8* (7), 506–514.

(2) Saparov, B.; Mitzi, D. B. Organic–Inorganic Perovskites: Structural Versatility for Functional Materials Design. *Chem. Rev.* **2016**, *116* (7), 4558–4596.

(3) Li, C.; Lu, X.; Ding, W.; Feng, L.; Gao, Y.; Guo, Z. Formability of ABX 3 (X = F, Cl, Br, I) Halide Perovskites. *Acta Crystallogr. Sect. B Struct. Sci.* **2008**, *64* (6), 702–707.

(4) Cheng, Z.; Lin, J. Layered Organic–Inorganic Hybrid Perovskites: Structure, Optical Properties, Film Preparation, Patterning and Templating Engineering. *CrystEngComm* **2010**, *12* (10), 2646.

(5) Sum, T. C.; Mathews, N. Advancements in Perovskite Solar Cells: Photophysics behind the Photovoltaics. *Energy Environ. Sci.* **2014**, *7* (8), 2518–2534.

(6) Umebayashi, T.; Asai, K.; Umebayashi, T.; Asai, K.; Kondo, T.; Kondo, T.; Nakao, A. Electronic Structures of Lead Iodide Based Low-Dimensional Crystals. *Phys. Rev. B - Condens. Matter Mater. Phys.* **2003**, *67* (15), 2–7.

(7) Yin, W. J.; Shi, T.; Yan, Y. Unusual Defect Physics in CH3NH3PbI3 Perovskite Solar Cell Absorber. *Appl. Phys. Lett.* **2014**, *104* (6).

(8) Protesescu, L.; Yakunin, S.; Bodnarchuk, M. I.; Krieg, F.; Caputo, R.; Hendon, C. H.; Yang, R. X.; Walsh, A.; Kovalenko, M. V. Nanocrystals of Cesium Lead Halide Perovskites (CsPbX3, X = Cl, Br, and I): Novel Optoelectronic Materials Showing Bright Emission with Wide Color Gamut. *Nano Lett.* **2015**, *15* (6), 3692–3696.

(9) Yang, Z.; Rajagopal, A.; Chueh, C. C.; Jo, S. B.; Liu, B.; Zhao, T.; Jen, A. K. Y. Stable Low-Bandgap Pb–Sn Binary Perovskites for Tandem Solar Cells. *Adv. Mater.* **2016**, *28* (40), 8990–8997.

(10) Yang, Z.; Chueh, C. C.; Liang, P. W.; Crump, M.; Lin, F.; Zhu, Z.; Jen, A. K. Y. Effects of Formamidinium and Bromide Ion Substitution in Methylammonium Lead Triiodide toward High-Performance Perovskite Solar Cells. *Nano Energy* **2016**, *22*, 328–337.

(11) Bush, K. A.; Frohna, K.; Prasanna, R.; Beal, R. E.; Leijtens, T.; Swifter, S. A.; McGehee, M. D. Compositional Engineering for Efficient Wide Band Gap Perovskites with Improved Stability to Photoinduced Phase Segregation. *ACS Energy Lett.* **2018**, *3* (2), 428–435.

(12) Grancini, G.; Nazeeruddin, M. K. Dimensional Tailoring of Hybrid Perovskites for Photovoltaics. *Nat. Rev. Mater.* **2018**, *4* (January).

(13) Ziffer, M. E.; Mohammed, J. C.; Ginger, D. S. Electroabsorption Spectroscopy Measurements of the Exciton Binding Energy, Electron-Hole Reduced Effective Mass, and Band Gap in the Perovskite CH3NH3PbI3. *ACS Photonics* **2016**, *3* (6), 1060–1068.

(14) Saba, M.; Quochi, F.; Mura, A.; Bongiovanni, G. Excited State Properties of Hybrid Perovskites. *Acc. Chem. Res.* **2016**, *49* (1), 166–173.

(15) Manser, J. S.; Christians, J. A.; Kamat, P. V. Intriguing Optoelectronic Properties of Metal Halide Perovskites. *Chem. Rev.* **2016**, *116* (21), 12956–13008.

(16) Stranks, S. D.; Eperon, G. E.; Grancini, G.; Menelaou, C.; Alcocer, M. J. P.; Leijtens, T.; Herz, L. M.; Petrozza, A.; Snaith, H. J. Electron-Hole Diffusion Lengths Exceeding 1 Micrometer in an Organometal Trihalide Perovskite Absorber. *Science (80-.).* **2013**, *342* (6156), 341–344.

(17) Saidaminov, M. I.; Abdelhady, A. L.; Murali, B.; Alarousu, E.; Burlakov, V. M.; Peng,

W.; Dursun, I.; Wang, L.; He, Y.; Maculan, G.; et al. High-Quality Bulk Hybrid Perovskite Single Crystals within Minutes by Inverse Temperature Crystallization. *Nat. Commun.* **2015**, *6* (May), 7586.

(18) Dong, Q.; Fang, Y.; Shao, Y.; Mulligan, P.; Qiu, J.; Cao, L.; Huang, J. Electron-Hole Diffusion Lengths > 175 m m in Solution-Grown CH 3 NH 3 PbI 3 Single Crystals. *Science (80-.).* **2015**, *347* (6225), 967–970.

(19) Green, M. A.; Hishikawa, Y.; Dunlop, E. D.; Levi, D. H.; Hohl-Ebinger, J.; Yoshita, M.; Ho-Baillie, A. W. Y. Solar Cell Efficiency Tables (Version 53). *Prog. Photovoltaics Res. Appl.* **2019**, *27* (1), 3–12.

(20) Yang, W. S.; Park, B.-W.; Jung, E. H.; Jeon, N. J.; Kim, Y. C.; Lee, D. U.; Shin, S. S.; Seo, J.; Kim, E. K.; Noh, J. H.; et al. Iodide Management in Formamidinium-Lead-Halide–Based Perovskite Layers for Efficient Solar Cells. *Science (80-.).* **2017**, *356* (6345), 1376–1379.

(21) Kim, Y.-H.; Cho, H.; Lee, T.-W. Metal Halide Perovskite Light Emitters. *Proc. Natl. Acad. Sci. U. S. A.* **2016**, *113* (42), 11694–11702.

(22) Tan, Z. K.; Moghaddam, R. S.; Lai, M. L.; Docampo, P.; Higler, R.; Deschler, F.; Price, M.; Sadhanala, A.; Pazos, L. M.; Credgington, D.; et al. Bright Light-Emitting Diodes Based on Organometal Halide Perovskite. *Nat Nanotechnol* **2014**, *9* (9), 687–692.

(23) Zhao, B.; Bai, S.; Kim, V.; Lamboll, R.; Shivanna, R.; Auras, F.; Richter, J. M.; Yang, L.; Dai, L.; Alsari, M.; et al. High-Efficiency Perovskite–Polymer Bulk Heterostructure Light-Emitting Diodes. *Nat. Photonics* **2018**, *12* (December).

(24) Sun, J.; Wu, J.; Tong, X.; Lin, F.; Wang, Y.; Wang, Z. M. Organic/Inorganic Metal Halide Perovskite Optoelectronic Devices beyond Solar Cells. *Adv. Sci.* **2018**, *5* (5).

(25) Deschler, F.; Price, M.; Pathak, S.; Klintberg, L. E.; Jarausch, D. D.; Higler, R.; Hüttner, S.; Leijtens, T.; Stranks, S. D.; Snaith, H. J.; et al. High Photoluminescence Efficiency and Optically Pumped Lasing in Solution-Processed Mixed Halide Perovskite Semiconductors. *J. Phys. Chem. Lett.* **2014**, *5* (8), 1421–1426.

(26) Dou, L.; Yang, Y. M.; You, J.; Hong, Z.; Chang, W.-H.; Li, G.; Yang, Y. Solution-Processed Hybrid Perovskite Photodetectors with High Detectivity. *Nat. Commun.* **2014**, *5*, 5404.

(27) Chen, Q.; De Marco, N.; Yang, Y. (Michael); Song, T.-B.; Chen, C.-C.; Zhao, H.; Hong, Z.; Zhou, H.; Yang, Y. Under the Spotlight: The Organic–Inorganic Hybrid Halide Perovskite for Optoelectronic Applications. *Nano Today* **2015**, *10* (3), 355–396.

(28) Burschka, J.; Pellet, N.; Moon, S.-J.; Humphry-Baker, R.; Gao, P.; Nazeeruddin, M. K.; Grätzel, M. Sequential Deposition as a Route to High-Performance Perovskite-Sensitized Solar Cells. *Nature* **2013**, *499* (7458), 316–319.

(29) Xiao, Z.; Bi, C.; Shao, Y.; Dong, Q.; Wang, Q.; Yuan, Y.; Wang, C.; Gao, Y.; Huang, J. Efficient, High Yield Perovskite Photovoltaic Devices Grown by Interdiffusion of Solution-Processed Precursor Stacking Layers. *Energy Environ. Sci.* **2014**, *7* (8), 2619–2623.

(30) Liu, M.; Johnston, M. B.; Snaith, H. J. Efficient Planar Heterojunction Perovskite Solar Cells by Vapour Deposition. *Nature* **2013**, *501* (7467), 395–398.

(31) Chen, Q.; Zhou, H.; Hong, Z.; Luo, S.; Duan, H.-S. S.; Wang, H.-H. H.; Liu, Y.; Li, G.; Yang, Y. Planar Heterojunction Perovskite Solar Cells via Vapor-Assisted Solution Process. *J. Am. Chem. Soc.* **2014**, *136* (2), 622–625.

(32) Nie, W.; Tsai, H.; Asadpour, R.; Blancon, J.-C.; Neukirch, A. J.; Gupta, G.; Crochet, J. J.;

Chhowalla, M.; Tretiak, S.; Alam, M. A.; et al. High-Efficiency Solution-Processed Perovskite Solar Cells with Millimeter-Scale Grains. *Science (80-.).* **2015**, *347* (6221), 522–525.

(33) Lee, M. M.; Teuscher, J.; Miyasaka, T.; Murakami, T. N.; Snaith, H. J. Efficient Hybrid Solar Cells Based on Meso-Superstructured Organometal Halide Perovskites. *Science (80-.).* **2012**, *338* (6107), 643–647.

(34) Zhang, W.; Saliba, M.; Moore, D. T.; Pathak, S. K.; Hörantner, M. T.; Stergiopoulos, T.; Stranks, S. D.; Eperon, G. E.; Alexander-Webber, J. A.; Abate, A.; et al. Ultrasmooth Organic–Inorganic Perovskite Thin-Film Formation and Crystallization for Efficient Planar Heterojunction Solar Cells. *Nat. Commun.* **2015**, *6*, 6142.

(35) Liang, P.-W.; Liao, C.-Y.; Chueh, C.-C.; Zuo, F.; Williams, S. T.; Xin, X.-K.; Lin, J.; Jen, A. K.-Y. Additive Enhanced Crystallization of Solution-Processed Perovskite for Highly Efficient Planar-Heterojunction Solar Cells. *Adv. Mater.* **2014**, *26* (22), 3748–3754.

(36) Zuo, C.; Ding, L. An 80.11% FF Record Achieved for Perovskite Solar Cells by Using the NH 4 Cl Additive. *Nanoscale* **2014**, *6*, 9935–9938.

(37) Jeon, N. J.; Noh, J. H.; Kim, Y. C.; Yang, W. S.; Ryu, S.; Seok, S. Il. Solvent Engineering for High-Performance Inorganic-Organic Hybrid Perovskite Solar Cells. *Nat. Mater.* **2014**, *1* (July), 1–7.

(38) Williams, S. T.; Chueh, C.-C.; Jen, A. K.-Y. Navigating Organo-Lead Halide Perovskite Phase Space via Nucleation Kinetics toward a Deeper Understanding of Perovskite Phase Transformations and Structure-Property Relationships. *Small* **2015**, *11* (26), 3088–3096.

(39) Dualeh, A.; Tétreault, N.; Moehl, T.; Gao, P.; Nazeeruddin, M. K.; Grätzel, M. Effect of Annealing Temperature on Film Morphology of Organic-Inorganic Hybrid Pervoskite Solid-State Solar Cells. *Adv. Funct. Mater.* **2014**, *24* (21), 3250–3258.

(40) Xiao, Z.; Dong, Q.; Bi, C.; Shao, Y.; Yuan, Y.; Huang, J. Solvent Annealing of Perovskite-Induced Crystal Growth for Photovoltaic-Device Efficiency Enhancement. *Adv. Mater.* **2014**, *26* (37), 6503–6509.

(41) Zhu, W.; Yu, T.; Li, F.; Bao, C.; Gao, H.; Yi, Y.; Yang, J.; Fu, G.; Zhou, X.; Zou, Z. A Facile, Solvent Vapor–Fumigation-Induced, Self-Repair Recrystallization of CH 3 NH 3 PbI 3 Films for High-Performance Perovskite Solar Cells. *Nanoscale* **2015**, *7* (12), 5427–5434.

(42) Xiao, J.; Yang, Y.; Xu, X.; Shi, J.; Zhu, L.; Lv, S.; Wu, H.; Luo, Y.; Li, D.; Meng, Q. Pressure-Assisted CH 3 NH 3 PbI 3 Morphology Reconstruction to Improve the High Performance of Perovskite Solar Cells. *J. Mater. Chem. A* **2015**, *3* (10), 5289–5293.

(43) Choi, J. J.; Yang, X.; Norman, Z. M.; Billinge, S. J. L.; Owen, J. S. Structure of Methylammonium Lead Iodide within Mesoporous Titanium Dioxide: Active Material in High-Performance Perovskite Solar Cells. *Nano Lett.* **2014**, *14* (1), 127–133.

(44) Manser, J. S.; Saidaminov, M. I.; Christians, J. A.; Bakr, O. M.; Kamat, P. V. Making and Breaking of Lead Halide Perovskites. *Acc. Chem. Res.* **2016**.

(45) Ball, J. M.; Petrozza, A. Defects in Perovskite-Halides and Their Effects in Solar Cells. *Nat. Energy* **2016**, *1* (11).

(46) Buin, A.; Pietsch, P.; Xu, J.; Voznyy, O.; Ip, A. H.; Comin, R.; Sargent, E. H. Materials Processing Routes to Trap-Free Halide Perovskites. *Nano Lett.* **2014**, *14* (11), 6281–6286.

(47) Walsh, A.; Scanlon, D. O.; Chen, S.; Gong, X. G.; Wei, S. H. Self-Regulation Mechanism for Charged Point Defects in Hybrid Halide Perovskites. *Angew. Chemie - Int. Ed.* **2015**, *54* (6), 1791–1794.

(48) Kim, J.; Lee, S.-H. H.; Lee, J. H.; Hong, K.-H. H. The Role of Intrinsic Defects in Methylammonium Lead Iodide Perovskite. *J. Phys. Chem. Lett.* **2014**, *5* (8), 1312–1317.

(49) Tachikawa, T.; Karimata, I.; Kobori, Y. Surface Charge Trapping in Organolead Halide Perovskites Explored by Single-Particle Photoluminescence Imaging. *J. Phys. Chem. Lett.* **2015**, *6* (16), 3195–3201.

(50) Kong, W.; Ding, T.; Bi, G.; Wu, H. Optical Characterizations of the Surface States in Hybrid Lead–Halide Perovskites. *Phys. Chem. Chem. Phys.* **2016**, *18* (18), 12626–12632.

(51) Peng, W.; Anand, B.; Liu, L.; Sampat, S.; Bearden, B. E.; Malko, A.; Chabal, Y. J. Influence of Growth Temperature on Bulk and Surface Defects in Hybrid Lead Halide Perovskite Films. *Nanoscale* **2015**, 1627–1634.

(52) de Quilettes, D. W.; Vorpahl, S. M.; Stranks, S. D.; Nagaoka, H.; Eperon, G. E.; Ziffer, M. E.; Snaith, H. J.; Ginger, D. S. Impact of Microstructure on Local Carrier Lifetime in Perovskite Solar Cells. *Science (80-.).* **2015**, *348* (6235), 683–686.

(53) Snaith, H. J.; Abate, A.; Ball, J. M.; Eperon, G. E.; Leijtens, T.; Noel, N. K.; Stranks, S. D.; Wang, J. T.-W.; Wojciechowski, K.; Zhang, W. Anomalous Hysteresis in Perovskite Solar Cells. *J. Phys. Chem. Lett.* **2014**, *5* (9), 1511–1515.

(54) Azpiroz, J. M.; Mosconi, E.; Bisquert, J.; De Angelis, F. Defect Migration in Methylammonium Lead Iodide and Its Role in Perovskite Solar Cell Operation. *Energy Environ. Sci.* **2015**, *8* (7), 2118–2127.

(55) Eames, C.; Frost, J. M.; Barnes, P. R. F.; O'Regan, B. C.; Walsh, A.; Islam, M. S. Ionic Transport in Hybrid Lead Iodide Perovskite Solar Cells. *Nat. Commun.* **2015**, *6*, 7497.

(56) Yuan, Y.; Huang, J. Ion Migration in Organometal Trihalide Perovskite and Its Impact on Photovoltaic Efficiency and Stability. *Acc. Chem. Res.* **2016**, *49* (2), 286–293.

(57) Shao, Y.; Fang, Y.; Li, T.; Wang, Q.; Dong, Q.; Deng, Y.; Yuan, Y.; Wei, H.; Wang, M.; Gruverman, A.; et al. Grain Boundary Dominated Ion Migration in Polycrystalline Organic–Inorganic Halide Perovskite Films. *Energy Environ. Sci.* **2016**, *9* (5), 1752–1759.

(58) Kim, H.-S.; Lee, C.-R.; Im, J.-H.; Lee, K.-B.; Moehl, T.; Marchioro, A.; Moon, S.-J.; Humphry-Baker, R.; Yum, J.-H.; Moser, J. E.; et al. Lead Iodide Perovskite Sensitized All-Solid-State Submicron Thin Film Mesoscopic Solar Cell with Efficiency Exceeding 9%. *Sci. Rep.* **2012**, *2*, 591.

(59) Kim, J. H.; Liang, P. W.; Williams, S. T.; Cho, N.; Chueh, C. C.; Glaz, M. S.; Ginger, D. S.; Jen, A. K. Y. High-Performance and Environmentally Stable Planar Heterojunction Perovskite Solar Cells Based on a Solution-Processed Copper-Doped Nickel Oxide Hole-Transporting Layer. *Adv. Mater.* **2015**, *27* (4), 695–701.

(60) Kresse, G.; Furthmüller, J. Efficient Iterative Schemes for *Ab Initio* Total-Energy Calculations Using a Plane-Wave Basis Set. *Phys. Rev. B* **1996**, *54* (16), 11169–11186.

(61) Kresse, G.; Furthmüller, J. Efficiency of Ab-Initio Total Energy Calculations for Metals and Semiconductors Using a Plane-Wave Basis Set. *Comput. Mater. Sci.* **1996**, *6* (1), 15–50.

(62) Perdew, J. P.; Burke, K.; Ernzerhof, M. Generalized Gradient Approximation Made Simple. **1996**, No. 3, 3865–3868.

(63) Blöchl, P. E. Projector Augmented-Wave Method. *Phys. Rev. B* **1994**, *50* (24), 17953–17979.

(64) Forrest, S. R.; Bradley, D. D. C.; Thompson, M. E. Measuring the Efficiency of Organic Light-Emitting Devices. *Adv. Mater.* **2003**, *15* (13), 1043–1048.

(65) Zhao, T.; Williams, S. T.; Chueh, C.-C.; DeQuilettes, D. W.; Liang, P.-W.; Ginger, D. S.;

Jen, A. K.-Y. Design Rules for the Broad Application of Fast (1 s) Methylamine Vapor Based, Hybrid Perovskite Post Deposition Treatments. *RSC Adv.* **2016**, *6* (33), pp 27475-27484.

(66) Zhao, Y.; Zhu, K. Optical Bleaching of Perovskite (CH3NH3)PbI3 through Room-Temperature Phase Transformation Induced by Ammonia. *Chem. Commun. (Camb).* **2014**, *50* (13), 1605–1607.

(67) Zhou, Z.; Wang, Z.; Zhou, Y.; Pang, S.; Wang, D.; Xu, H.; Liu, Z.; Padture, N. P.; Cui, G. Methylamine-Gas Induced Defect-Healing Behavior of CH 3 NH 3 PbI 3 Thin Films for Perovskite Solar Cells. *Angew. Chemie Int. Ed.* **2015**.

(68) D'Innocenzo, V.; Kandada, A. R. S.; Bastiani, M. De; Gandini, M.; Petrozza, A.; Srimath Kandada, A. R.; De Bastiani, M.; Gandini, M.; Petrozza, A. Tuning the Light Emission Properties by Band Gap Engineering in Hybrid Lead Halide Perovskite. *J. Am. Chem. Soc.* **2014**, *136* (51), 17730–17733.

(69) Impact of Microstructure on Local Carrier Lifetime in Perovskite Solar Cells. *Science (80-.).* **2015**, *348* (6235), 683–686.

(70) Hao, F.; Stoumpos, C. C.; Liu, Z.; Chang, R. P. H.; Kanatzidis, M. G. Controllable Perovskite Crystallization at a Gas–Solid Interface for Hole Conductor-Free Solar Cells with Steady Power Conversion Efficiency over 10%. *J. Am. Chem. Soc.* **2014**, *136* (46), 16411–16419.

(71) Park, B.; Philippe, B.; Gustafsson, T.; Sveinbjörnsson, K.; Hagfeldt, A.; Johansson, E. M. J.; Boschloo, G. Enhanced Crystallinity in Organic–Inorganic Lead Halide Perovskites on Mesoporous TiO2 via Disorder–Order Phase Transition. *Chem. Mater.* **2014**, *26* (15), 4466–4471.

(72) Damjanovic, D. Ferroelectric, Dielectric and Piezoelectric Properties of Ferroelectric Thin Films and Ceramics. *Reports Prog. Phys.* **1999**, *61* (9), 1267.

(73) Yongzhen, W.; Islam, A.; Yang, X.; Qin, C.; Liu, J.; Zhang, K.; Peng, W.; Han, L.; Wu, Y.; Islam, A.; et al. Retarding the Crystallization of PbI2 for Highly Reproducible Planar-Structured Perovskite Solar Cells via Sequential Deposition. *Energy Environ. Sci.* **2014**, *7*, 2934.

(74) Yang, W. S.; Noh, J. H.; Jeon, N. J.; Kim, Y. C.; Ryu, S.; Seo, J.; Seok, S. Il. High-Performance Photovoltaic Perovskite Layers Fabricated through Intramolecular Exchange. *Science (80-.).* **2015**, *348* (6240), 1234–1237.

(75) Leguy, A. M. A.; Hu, Y.; Campoy-Quiles, M.; Alonso, M. I.; Weber, O. J.; Azarhoosh, P.; van Schilfgaarde, M.; Weller, M. T.; Bein, T.; Nelson, J.; et al. Reversible Hydration of CH 3 NH 3 PbI 3 in Films, Single Crystals, and Solar Cells. *Chem. Mater.* **2015**, *27* (9), 3397–3407.

(76) Pedro, G.; Sanchez, C. *Functional Hybrid Materials*; Pedro, G., Sanchez, C., Eds.; John Wiley & Sons, 2006.

(77) Wu, Y.; Islam, A.; Yang, X.; Qin, C.; Liu, J.; Zhang, K.; Peng, W.; Han, L. Retarding the Crystallization of PbI2 for Highly Reproducible Planar-Structured Perovskite Solar Cells via Sequential Deposition. *Energy Environ. Sci.* **2014**, *7*, 2934.

(78) Yan, K.; Long, M.; Zhang, T.; Wei, Z.; Chen, H.; Yang, S.; Xu, J. Hybrid Halide Perovskite Solar Cell Precursors: Colloidal Chemistry and Coordination Engineering behind Device Processing for High Efficiency. *J. Am. Chem. Soc.* **2015**, *137* (13), 4460–4468.

(79) Ahn, N.; Son, D.-Y.; Jang, I.-H.; Kang, S. M.; Choi, M.; Park, N.-G. Highly Reproducible

Perovskite Solar Cells with Average Efficiency of 18.3% and Best Efficiency of 19.7% Fabricated via Lewis Base Adduct of Lead(II) Iodide. *J. Am. Chem. Soc.* **2015**, *137* (27), 8696–8699.

(80) Noel, N. K.; Abate, A.; Stranks, S. D.; Parrott, E. S.; Burlakov, V. M.; Goriely, A.; Snaith, H. J. Enhanced Photoluminescence and Solar Cell Performance via Lewis Base Passivation of Organic–Inorganic Lead Halide Perovskites. *ACS Nano* **2014**, *8* (10), 9815–9821.

(81) Mitzi, D. B. Synthesis, Structure, and Properties of Organic-Inorganic Perovskites and Related Materials. In *prog. inorg. chem.*; 1999; pp 1–121.

(82) Yang, S.; Zheng, Y. C.; Hou, Y.; Chen, X.; Chen, Y.; Wang, Y.; Zhao, H.; Yang, H. G. Formation Mechanism of Freestanding CH 3 NH 3 PbI 3 Functional Crystals: In Situ Transformation vs Dissolution–Crystallization. *Chem. Mater.* **2014**, *26* (23), 6705–6710.

(83) Koh, T. M.; Fu, K.; Fang, Y.; Chen, S.; Sum, T. C.; Mathews, N.; Mhaisalkar, S. G.; Boix, P. P.; Baikie, T. Formamidinium-Containing Metal-Halide: An Alternative Material for Near-IR Absorption Perovskite Solar Cells. *J. Phys. Chem. C* **2014**, *118* (30), 16458–16462.

(84) Zhao, T.; Chueh, C.-C.; Chen, Q.; Rajagopal, A.; Jen, A. K.-Y. Defect Passivation of Organic-Inorganic Hybrid Perovskites by Diammonium Iodide towards High-Performance Photovoltaic Devices. *ACS Energy Lett.* **2016**, *1*, 757–763.

(85) Chen, Q.; Zhou, H.; Song, T. Bin; Luo, S.; Hong, Z.; Duan, H. S.; Dou, L.; Liu, Y.; Yang, Y. Controllable Self-Induced Passivation of Hybrid Lead Iodide Perovskites toward High Performance Solar Cells. *Nano Lett.* **2014**, *14* (7), 4158–4163.

(86) Supasai, T.; Rujisamphan, N.; Ullrich, K.; Chemseddine, a.; Dittrich, T. Formation of a Passivating CH3NH3PbI3/PbI2 Interface during Moderate Heating of CH3NH3PbI3 Layers. *Appl. Phys. Lett.* **2013**, *103* (18), 183906.

(87) Wang, L.; McCleese, C.; Kovalsky, A.; Zhao, Y.; Burda, C. Femtosecond Time-Resolved Transient Absorption Spectroscopy of CH 3 NH 3 PbI 3 Perovskite Films: Evidence for Passivation Effect of PbI 2. *J. Am. Chem. Soc.* **2014**, *136* (35), 12205–12208.

(88) Abate, A.; Saliba, M.; Hollman, D. J.; Stranks, S. D.; Wojciechowski, K.; Avolio, R.; Grancini, G.; Petrozza, A.; Snaith, H. J. Supramolecular Halogen Bond Passivation of Organic-Inorganic Halide Perovskite Solar Cells. *Nano Lett.* **2014**, *14* (6), 3247–3254.

(89) Noel, N. K.; Abate, A.; Stranks, S. D.; Parrott, E. S.; Burlakov, V. M.; Goriely, A.; Snaith, H. J. Enhanced Photoluminescence and Solar Cell Performance via Lewis Base Passivation of Organic–Inorganic Lead Halide Perovskites. *ACS Nano* **2014**, *8* (10), 9815–9821.

(90) Zhang, J.; Wang, P.; Huang, X.; Xu, J.; Wang, L.; Yue, G.; Lu, X.; Liu, J.; Hu, Z.; Zhu, Y. Polar Molecules Modified Perovskite Surface to Reduce the Recombination in Perovskite Solar Cells. *RSC Adv.* **2015**, *6*, 9090–9095.

(91) Xu, J.; Buin, A.; Ip, A. H.; Li, W.; Voznyy, O.; Comin, R.; Yuan, M.; Jeon, S.; Ning, Z.; McDowell, J. J.; et al. Perovskite–Fullerene Hybrid Materials Suppress Hysteresis in Planar Diodes. *Nat. Commun.* **2015**, *6* (May), 7081.

(92) Shao, Y.; Xiao, Z.; Bi, C.; Yuan, Y.; Huang, J. Origin and Elimination of Photocurrent Hysteresis by Fullerene Passivation in CH3NH3PbI3 Planar Heterojunction Solar Cells. *Nat. Commun.* **2014**, *5*, 5784.

(93) Liang, P.-W.; Chueh, C.-C.; Williams, S. T.; Jen, A. K.-Y. Roles of Fullerene-Based Interlayers in Enhancing the Performance of Organometal Perovskite Thin-Film Solar

Cells. *Adv. Energy Mater.* **2015**, *5* (10), n/a-n/a.

(94) Li, C. Z.; Chueh, C. C.; Yip, H. L.; Ding, F.; Li, X.; Jen, A. K. Y. Solution-Processible Highly Conducting Fullerenes. **2013**, No. 17, 2457–2461.

(95) Li, C. Z.; Chueh, C. C.; Ding, F.; Yip, H. L.; Liang, P. W.; Li, X.; Jen, A. K. Y. Doping of Fullerenes via Anion-Induced Electron Transfer and Its Implication for Surfactant Facilitated High Performance Polymer Solar Cells. **2013**, No. 32, 4425–4430.

(96) Intrinsic White-Light Emission from Layered Hybrid Perovskites. *J. Am. Chem. Soc.* **2014**, *136* (38), 13154–13157.

(97) Lemmerer, A.; Billing, D. G. Lead Halide Inorganic–Organic Hybrids Incorporating Diammonium Cations. *CrystEngComm* **2012**, *14* (6), 1954.

(98) Quan, L. N.; Yuan, M.; Comin, R.; Voznyy, O.; Beauregard, E. M.; Hoogland, S.; Buin, A.; Kirmani, A. R.; Zhao, K.; Amassian, A.; et al. Ligand-Stabilized Reduced-Dimensionality Perovskites. *J. Am. Chem. Soc.* **2016**, *138* (8), 2649–2655.

(99) Smith, I. C.; Hoke, E. T.; Solis-Ibarra, D.; McGehee, M. D.; Karunadasa, H. I. A Layered Hybrid Perovskite Solar-Cell Absorber with Enhanced Moisture Stability. *Angew. Chemie Int. Ed.* **2014**, *53* (42), 11232–11235.

(100) Two-Dimensional Homologous Perovskites as Light Absorbing Materials for Solar Cell Applications. *J. Am. Chem. Soc.* **2015**.

(101) Zhang, Y.-Y.; Chen, S.; Xu, P.; Xiang, H.; Gong, X.-G.; Walsh, A.; Wei, S. Intrinsic Instability of the Hybrid Halide Perovskite Semiconductor CH3NH3PbI3. *Nat. Commun.* **2015**, No. JUNE, 11.

(102) He, Z.; Zhong, C.; Huang, X.; Wong, W. Y.; Wu, H.; Chen, L.; Su, S.; Cao, Y. Simultaneous Enhancement of Open-Circuit Voltage, Short-Circuit Current Density, and Fill Factor in Polymer Solar Cells. *Adv. Mater.* **2011**, *23* (40), 4636–4643.

(103) Chen, Q.; Mao, L.; Li, Y.; Kong, T.; Wu, N.; Ma, C.; Bai, S.; Jin, Y.; Wu, D.; Lu, W.; et al. Quantitative Operando Visualization of the Energy Band Depth Profile in Solar Cells. *Nat. Commun.* **2015**, *6*, 7745.

(104) Zhou, H.; Zhang, Y.; Seifter, J.; Collins, S. D.; Luo, C.; Bazan, G. C.; Nguyen, T. Q.; Heeger, A. J. High-Efficiency Polymer Solar Cells Enhanced by Solvent Treatment. *Adv. Mater.* **2013**, *25* (11), 1646–1652.

(105) Cowan, S. R.; Roy, a; Heeger, a J. Recombination in Polymer-Fullerene Bulk Heterojunction Solar Cells. *Phys. Rev. B* **2010**, *82* (24), 245207.

(106) Li, C. Z.; Chang, C. Y.; Zang, Y.; Ju, H. X.; Chueh, C. C.; Liang, P. W.; Cho, N.; Ginger, D. S.; Jen, A. K. Y. Suppressed Charge Recombination in Inverted Organic Photovoltaics via Enhanced Charge Extraction by Using a Conductive Fullerene Electron Transport Layer. *Adv. Mater.* **2014**, 6262–6267.

(107) Zhao, T.; Liu, H.; Ziffer, M. E.; Rajagopal, A.; Zuo, L.; Ginger, D. S.; Li, X.; Jen, A. K. Y. Realization of a Highly Oriented MAPbBr 3 Perovskite Thin Film via Ion Exchange for Ultrahigh Color Purity Green Light Emission. *ACS Energy Lett.* **2018**, *3* (7), 1662–1669.

(108) Dubey, A.; Adhikari, N.; mabrouk, sally; Wu, F.; Chen, K.; Yang, S.; Qiao, Q. Strategic Review on Processing Routes towards Highly Efficient Perovskite Solar Cells. *J. Mater. Chem. A* **2018**, *6* (di), 2406–2431.

(109) Cho, H.; Jeong, S.-H.; Park, M.-H.; Kim, Y.-H.; Wolf, C.; Lee, C.-L.; Heo, J. H.; Sadhanala, A.; Myoung, N.; Yoo, S.; et al. Overcoming the Electroluminescence Efficiency Limitations of Perovskite Light-Emitting Diodes. *Science (80-.).* **2015**, *350*

(6265), 1222–1225.

(110) Giesbrecht, N.; Schlipf, J.; Oesinghaus, L.; Binek, A.; Bein, T.; Müller-Buschbaum, P.; Docampo, P. Synthesis of Perfectly Oriented and Micrometer-Sized MAPbBr 3 Perovskite Crystals for Thin-Film Photovoltaic Applications. *ACS Energy Lett.* **2016**, *1* (1), 150–154.

(111) Yu, J. C.; Kim, D. Bin; Jung, E. D.; Lee, B. R.; Song, M. H. High-Performance Perovskite Light-Emitting Diodes via Morphological Control of Perovskite Films. *Nanoscale* **2016**, *8*, 7036–7042.

(112) Li, G.; Tan, Z. K.; Di, D.; Lai, M. L.; Jiang, L.; Lim, J. H. W.; Friend, R. H.; Greenham, N. C. Efficient Light-Emitting Diodes Based on Nanocrystalline Perovskite in a Dielectric Polymer Matrix. *Nano Lett.* **2015**, *15* (4), 2640–2644.

(113) Chen, Z.; Zhang, C.; Jiang, X.-F.; Liu, M.; Xia, R.; Shi, T.; Chen, D.; Xue, Q.; Zhao, Y.-J.; Su, S.; et al. High-Performance Color-Tunable Perovskite Light Emitting Devices through Structural Modulation from Bulk to Layered Film. *Adv. Mater.* **2017**, *29* (8), 1603157.

(114) Kumar, P.; Zhao, B.; Friend, R. H.; Sadhanala, A.; Narayan, K. S. Kinetic Control of Perovskite Thin-Film Morphology and Application in Printable Light-Emitting Diodes. *ACS Energy Lett.* **2017**, *2* (1), 81–87.

(115) Ji, F.; Pang, S.; Zhang, L.; Zong, Y.; Cui, G.; Padture, N. P.; Zhou, Y. Simultaneous Evolution of Uniaxially Oriented Grains and Ultralow-Density Grain-Boundary Network in CH3NH3PbI3Perovskite Thin Films Mediated by Precursor Phase Metastability. *ACS Energy Lett.* **2017**, *2* (12), 2727–2733.

(116) Kim, D. H.; Park, J.; Li, Z.; Yang, M.; Park, J. S.; Park, I. J.; Kim, J. Y.; Berry, J. J.; Rumbles, G.; Zhu, K. 300% Enhancement of Carrier Mobility in Uniaxial-Oriented Perovskite Films Formed by Topotactic-Oriented Attachment. *Adv. Mater.* **2017**, *29* (23), 1–8.

(117) Wang, Z.; Lin, Q.; Chmiel, F. P.; Sakai, N.; Herz, L. M.; Snaith, H. J. Efficient Ambient-Air-Stable Solar Cells with 2D–3D Heterostructured Butylammonium-Caesium-Formamidinium Lead Halide Perovskites. *Nat. Energy* **2017**, *6* (August), 17135.

(118) Leblebici, S. Y.; Leppert, L.; Li, Y.; Reyes-Lillo, S. E.; Wickenburg, S.; Wong, E.; Lee, J.; Melli, M.; Ziegler, D.; Angell, D. K.; et al. Facet-Dependent Photovoltaic Efficiency Variations in Single Grains of Hybrid Halide Perovskite. *Nat. Energy* **2016**, *1* (8), 1–7.

(119) Kumar, S.; Jagielski, J.; Kallikounis, N.; Kim, Y. H.; Wolf, C.; Jenny, F.; Tian, T.; Hofer, C. J.; Chiu, Y. C.; Stark, W. J.; et al. Ultrapure Green Light-Emitting Diodes Using Two-Dimensional Formamidinium Perovskites: Achieving Recommendation 2020 Color Coordinates. *Nano Lett.* **2017**, *17* (9), 5277–5284.

(120) Koh, T. M.; Shanmugam, V.; Schlipf, J.; Oesinghaus, L.; Müller-Buschbaum, P.; Ramakrishnan, N.; Swamy, V.; Mathews, N.; Boix, P. P.; Mhaisalkar, S. G. Nanostructuring Mixed-Dimensional Perovskites: A Route Toward Tunable, Efficient Photovoltaics. *Adv. Mater.* **2016**, *28* (19), 3653–3661.

(121) Jiang, Y.; Leyden, M. R.; Qiu, L.; Wang, S.; Ono, L. K.; Wu, Z.; Juarez-Perez, E. J.; Qi, Y. Combination of Hybrid CVD and Cation Exchange for Upscaling Cs-Substituted Mixed Cation Perovskite Solar Cells with High Efficiency and Stability. *Adv. Funct. Mater.* **2018**, *28* (1), 1703835.

(122) Kamminga, M. E.; Fang, H. H.; Filip, M. R.; Giustino, F.; Baas, J.; Blake, G. R.; Loi, M. A.; Palstra, T. T. M. Confinement Effects in Low-Dimensional Lead Iodide Perovskite Hybrids. *Chem. Mater.* **2016**, *28* (13), 4554–4562.

(123) Dohner, E. R.; Jaffe, A.; Bradshaw, L. R.; Karunadasa, H. I. Intrinsic White-Light Emission from Layered Hybrid Perovskites. *J. Am. Chem. Soc.* **2014**, *136* (38), 13154–13157.

(124) Quan, L. N.; Yuan, M.; Comin, R.; Voznyy, O.; Beauregard, E. M.; Hoogland, S.; Buin, A.; Kirmani, A. R.; Zhao, K.; Amassian, A.; et al. Ligand-Stabilized Reduced-Dimensionality Perovskites. *J. Am. Chem. Soc.* **2016**, *138* (8), 2649–2655.

(125) Tian, Y.; Scheblykin, I. G. Artifacts in Absorption Measurements of Organometal Halide Perovskite Materials: What Are the Real Spectra? *J. Phys. Chem. Lett.* **2015**, *6* (13), 3466–3470.

(126) Grancini, G.; Srimath Kandada, A. R.; Frost, J. M.; Barker, A. J.; De Bastiani, M.; Gandini, M.; Marras, S.; Lanzani, G.; Walsh, A.; Petrozza, A. Role of Microstructure in the Electron–Hole Interaction of Hybrid Lead Halide Perovskites. *Nat. Photonics* **2015**, *9* (10), 695–701.

(127) Valence and Conduction Band Densities of States of Metal Halide Perovskites: A Combined Experimental - Theoretical Study. *J. Phys. Chem. Lett.* **2016**, *7*, acs.jpclett.6b00946-jpclett.6b00946.

(128) He, B. B. *Two-Dimensional X-Ray Diffraction*; John Wiley & Sons, Inc.: Hoboken, NJ, USA, 2009.

(129) Materials Processing Routes to Trap-Free Halide Perovskites. *Nano Lett.* **2014**, *14* (11), 6281–6286.

(130) Stranks, S. D. Nonradiative Losses in Metal Halide Perovskites. *ACS Energy Lett.* **2017**, *2* (7), 1515–1525.

(131) Sherkar, T. S.; Momblona, C.; Gil-Escrig, L.; Ávila, J.; Sessolo, M.; Bolink, H. J.; Koster, L. J. A. Recombination in Perovskite Solar Cells: Significance of Grain Boundaries, Interface Traps, and Defect Ions. *ACS Energy Lett.* **2017**, *2* (5), 1214–1222.

(132) Schubert, F. E. Light-Emitting Diodes. *Cambridge Universtiy Press* **2006**.

(133) Pust, P.; Schmidt, P. J.; Schnick, W. A Revolution in Lighting. *Nat. Mater.* **2015**, *14* (5), 454–458.

(134) Demchyshyn, S.; Roemer, J. M.; Groiß, H.; Heilbrunner, H.; Ulbricht, C.; Apaydin, D.; Böhm, A.; Rütt, U.; Bertram, F.; Hesser, G.; et al. Confining Metal-Halide Perovskites in Nanoporous Thin Films. *Sci. Adv.* **2017**, *3* (8), 1–12.

(135) Wang, Z.; Luo, Z.; Zhao, C.; Guo, Q.; Wang, Y.; Wang, F.; Bian, X.; Alsaedi, A.; Hayat, T.; Tan, Z. Efficient and Stable Pure Green All-Inorganic Perovskite CsPbBr3Light-Emitting Diodes with a Solution-Processed NiOxInterlayer. *J. Phys. Chem. C* **2017**, *121* (50), 28132–28138.

(136) Liang, D.; Peng, Y.; Fu, Y.; Shearer, M. J.; Zhang, J.; Zhai, J.; Zhang, Y.; Hamers, R. J.; Andrew, T. L.; Jin, S. Color-Pure Violet-Light-Emitting Diodes Based on Layered Lead Halide Perovskite Nanoplates. *ACS Nano* **2016**, *10* (7), 6897–6904.

(137) Zou, W.; Li, R.; Zhang, S.; Liu, Y.; Wang, N.; Cao, Y.; Miao, Y.; Xu, M.; Guo, Q.; Di, D.; et al. Minimising Efficiency Roll-off in High-Brightness Perovskite Light-Emitting Diodes. *Nat. Commun.* **2018**, *9* (1), 608.

(138) Lv, Y.; Shi, Y.; Song, X.; Liu, J.; Wang, M.; Wang, S.; Feng, Y.; Jin, S.; Hao, C. Bromine Doping as an Efficient Strategy to Reduce the Interfacial Defects in Hybrid 2D/3D Stacking Perovskite Solar Cells. *ACS Appl. Mater. Interfaces* **2018**, *10*, acsami.8b09461.

(139) Hu, Y.; Schlipf, J.; Wussler, M.; Petrus, M. L.; Jaegermann, W.; Bein, T.; Müller-Buschbaum, P.; Docampo, P. Hybrid Perovskite/Perovskite Heterojunction Solar Cells.

ACS Nano **2016**, *10* (6), 5999–6007.

(140) Cho, Y.; Soufiani, A. M.; Yun, J. S.; Kim, J.; Lee, D. S.; Seidel, J.; Deng, X.; Green, M. A.; Huang, S.; Ho-Baillie, A. W. Y. Mixed 3D–2D Passivation Treatment for Mixed-Cation Lead Mixed-Halide Perovskite Solar Cells for Higher Efficiency and Better Stability. *Adv. Energy Mater.* **2018**, *8* (20), 1–10.

(141) Chen, P.; Bai, Y.; Wang, S.; Lyu, M.; Yun, J. H.; Wang, L. In Situ Growth of 2D Perovskite Capping Layer for Stable and Efficient Perovskite Solar Cells. *Adv. Funct. Mater.* **2018**, *28* (17), 1–10.

(142) Wang, Y.; Zhang, T.; Kan, M.; Li, Y.; Wang, T.; Zhao, Y. Efficient α-CsPbI3Photovoltaics with Surface Terminated Organic Cations. *Joule* **2018**, 1–11.

(143) Lin, Y.; Bai, Y.; Fang, Y.; Chen, Z.; Yang, S.; Zheng, X.; Tang, S.; Liu, Y.; Zhao, J.; Huang, J. Enhanced Thermal Stability in Perovskite Solar Cells by Assembling 2D/3D Stacking Structures. *J. Phys. Chem. Lett.* **2018**, *9* (3), 654–658.

(144) Cho, K. T.; Zhang, Y.; Orlandi, S.; Cavazzini, M.; Zimmermann, I.; Lesch, A.; Tabet, N.; Pozzi, G.; Grancini, G.; Nazeeruddin, M. K. Water-Repellent Low-Dimensional Fluorous Perovskite as Interfacial Coating for 20% Efficient Solar Cells. *Nano Lett.* **2018**, *18* (9), 5467–5474.

(145) Ma, C.; Leng, C.; Ji, Y.; Wei, X.; Sun, K.; Tang, L.; Yang, J.; Luo, W.; Li, C.; Deng, Y.; et al. 2D/3D Perovskite Hybrids as Moisture-Tolerant and Efficient Light Absorbers for Solar Cells. *Nanoscale* **2016**, *8* (43), 18309–18314.

(146) Yoo, H. S.; Park, N. G. Post-Treatment of Perovskite Film with Phenylalkylammonium Iodide for Hysteresis-Less Perovskite Solar Cells. *Sol. Energy Mater. Sol. Cells* **2018**, *179* (December 2017), 57–65.

(147) Cao, D. H.; Stoumpos, C. C.; Farha, O. K.; Hupp, J. T.; Kanatzidis, M. G. 2D Homologous Perovskites as Light-Absorbing Materials for Solar Cell Applications. *J. Am. Chem. Soc.* **2015**, *137* (24), 7843–7850.

APPENDIX A: ABBREVIATIONS

0D: zero-dimensional

1D: one-dimensional

2D: two-dimensional

3D: three-dimensional

ΔG: Gibbs free energy

BA^+: butylammonium or $CH_3(CH_2)_3NH_3I$

C4-di-I_2 or C4 (chapter 4): $NH_3I(CH_2)_4NH_3I$

C4-mono-I: $CH_3(CH_2)_3NH_3I$

C8-di-I_2 or C8 (chapter 4): $NH_3I(CH_2)_8NH_3I$

CB: conduction band

CF: chloroform

CIE: Commission Internationale de l'Eclairage

DCB: ortho-dichlorobenzene

DFT: density function theory

DMF: dimethylformamide

DMSO: dimethyl sulfoxide

DOS: density of states

E_b: binding energy

EDBE-di-I_2 or EDBE (chapter 4): $NH_3I(CH_2)_2O(CH_2)_2O(CH_2)_2NH_3I$

E_f: formation energy

E_g: band gap

EL: electroluminescence

ETL: electron transporting layer

EQE: external quantum efficiency

FA^+: $HC(NH_2)_2^+$ formamidinium

FF: fill factor

FWHM: full width half maximum

GB: grain boundary

GBL: gamma-butyrolactone

IPA: isopropyl alcohol

ITO: indium tin oxide

J_{sc}: short-circuit current

L_D: diffusion length

LD: low-dimensional

MA^0: methylamine

MA^+: $CH_3NH_3^+$ or methylammonium

MAI: CH_3NH_3I

$MAPbBr_3$: methylammonium lead bromide or $CH_3NH_3PbBr_3$

$MAPbI_3$: methylammonium lead iodide or $CH_3NH_3PbI_3$

OIHP: Organic-inorganic halide perovskites

PCE: power conversion efficiency

PEAI: $C_6H_5(CH_2)_2NH_3I$

PHJ: planar heterojunction

PL: photoluminescence

PMMA: poly (methyl methacrylate)

PSC: perovskite solar cell

PV: photovoltaic

RMS: root-mean-square

SEM: secondary electron microscopy

SKPM: scanning kelvin probe microscopy

SP: surface potential

TCSPC: time-correlated single photon counting

TEM: Transmission electron microscopy

TRPL: Time-resolved photoluminescence

UPS: Ultraviolet photoelectron spectroscopy

UV-vis: ultraviolet-visible

VB: valence band

V_{oc}: open-circuit voltage

XPS: X-ray photoelectron spectroscopy

XRD: X-ray diffraction

VITA

Ting Zhao was born and raised in Qingdao, a seaside city of China, where she attended Qingdao No.2 High School and found her interest in chemistry. In 2009 she was admitted into Beijing University of Chemical Technology majoring in Polymer Science and Engineering. During her senior year, she worked under the mentorship of Dr. Shouke Yan studying polymer synthesis for phosphorescent LEDs. She graduated in 2013, receiving a Bachelor of Engineering degree. Ting then began graduate school in September of 2013 at University of Washington and began working under the supervision of Dr. Alex K.-Y. Jen in 2014 on perovskite solar cells.